



UNIVERSITY OF CAGLIARI

DEPARTMENT OF MATHEMATICS AND COMPUTER SCIENCE
PhD COURSE IN COMPUTER SCIENCE
CYCLE XXXI

Ph.D. THESIS

Microscopic Blood Images Analysis by Computer Vision Techniques

S.S.D. INF/01

CANDIDATE
Andrea Loddo

PhD SUPERVISOR
Prof. Cecilia Di Ruberto
Prof. Michel Kocher

PhD COORDINATOR
Prof. Michele Marchesi

Final examination academic year 2017/2018

"I resist what I cannot change."

I want to state a particular thank to prof. Cecilia Di Ruberto, prof. Michel Kocher, and Lorenzo, who have always supported me in the realization of this work.

I dedicate my thesis to my parents. Because without whom it would never have been started.

To my love, friends, relatives, anyone who has taught me something. Because without whom it would never have been finished.

To Salvatore and Rosalba. Because you are always on my mind.

Voglio esprimere un ringraziamento particolare alla Prof.ssa Cecilia Di Ruberto, al prof. Michel Kocher e a Lorenzo, per avermi sempre supportato nella realizzazione di questo lavoro.

Dedico la mia tesi ai miei genitori. Perché senza di loro non sarebbe mai iniziato.

Al mio amore, amici, parenti, chiunque mi abbia insegnato qualcosa. Perché senza di loro non sarebbe mai finito.

A Salvatore e Rosalba. Perché siete sempre nella mia mente.

Abstract

Automatic analysis and information extraction from an image is still a highly challenging research problem in the computer vision area, attempting to describe the image content with computational and mathematical techniques. Moreover, the information extracted from the image should be meaningful and as most discriminatory as possible, since it will be used to categorize its content according to the analyzed problem. In the Medical Imaging domain, many important decisions that affect patient care depends on the usefulness of the information extracted from the image. Managing medical image is even more complicated not only due to the importance of the problem but also because it needs a fair amount of prior medical knowledge to be able to represent with data the visual information to which pathologist refer.

Today medical decisions that impact patient care rely on the results of laboratory tests to a greater extent than ever before, due to the marked expansion in the number and complexity of offered tests. These developments promise to improve the care of patients, but the more increase the number and complexity of the tests, the more improvements the possibility to misapply and misinterpret the test themselves, leading to inappropriate diagnosis and therapies. Moreover, pathologists devote much time to the analysis of the tests rather than to the patients care and to the prescription of the right treatment, because of the increased number of tests and amount of data to analyze. Sometimes it can be a waste of time, considering that most of the tests performed are only check-up tests, and most of the analyzed samples come from healthy patients.

Then, a quantitative evaluation of medical images is essential to overcome uncertainty and subjectivity, but also to reduce the amount of data and the timing of the analysis significantly. In the last few years, many computer-assisted diagnosis systems have been developed, attempting to mimic pathologists by extracting features from the images. Image analysis involves complex algorithms to identify and characterize cells or tissues using image pattern recognition technology. This thesis addresses the main problems associated to the digital microscopy analysis in hematology diagnosis, with the development of algorithms both for the extraction of useful information from different digital images and for the distinction of various biological structures. The proposed methods aim to improve the degree of accuracy of the analysis and to reduce the diagnosis time. Furthermore, they can be used as

standard tools for skimming the number of samples to be analyzed directly from the pathologist, or as double check systems to verify the correct results of the automated facilities used today.

Contents

List of Figures	11
List of Tables	17
1 Introduction	21
1.1 CAD - Computer Aided Diagnosis	22
1.2 Contributions	23
1.3 Dissertation structure	24
I Digital Microscopy CAD	27
2 Image Pre-processing	31
2.1 Operations on the histogram	31
2.2 Operations of local pre-processing	32
2.2.1 Smoothing operators	33
2.2.2 Sharpening operators	33
2.3 Color and Color Spaces	34
2.3.1 Primary Spaces	35
2.3.2 Luminance-Chrominance Spaces	36
2.3.3 Perceptual Spaces	38
3 Segmentation	41
3.1 Pixel Based or Thresholding	41
3.1.1 Otsu Algorithm	42
3.1.2 Zack Algorithm	43
3.1.3 Fuzzy Threshold	43
3.1.4 Local Thresholding	44
3.2 Edge Based	44
3.2.1 LoG Operator	45
3.2.2 Canny Operator	46
3.2.3 Deformable Models	46
3.3 Region Based	47

3.3.1	Region Growing	48
3.3.2	Split and Merge	48
3.3.3	Watershed	49
3.4	Post-Processing	50
3.4.1	Mathematical morphology	50
4	Feature Extraction	53
4.1	Contour Descriptors	54
4.2	Regional Descriptors	54
4.2.1	Geometric Descriptors	54
4.2.2	Chromatic Descriptors	55
4.2.3	Texture Descriptors	56
4.3	Feature Selection	64
5	Classification	67
5.1	Nearest Neighbor	68
5.2	Decision Trees	68
5.3	Bayesian Classifier	69
5.4	Artificial Neural Network	69
5.5	Support Vector Machine	70
5.5.1	One-vs-all SVM	71
5.5.2	One-vs-one SVM	71
5.6	Deep learning methods	72
5.6.1	Neural Networks	72
5.6.2	Convolutional Neural Networks (CNNs)	73
5.6.3	Deep CNN Architectures	73
5.6.4	Recurrent Neural Networks (RNNs)	74
5.7	Model Evaluation	75
II	CAD for Peripheral Blood Images	79
6	Background	81
6.1	Hematology	81
6.2	Peripheral Blood Images	83
6.3	ALL - Acute Lymphoblastic Leukemia	85
6.3.1	Related Works	86
6.3.2	White Blood Cells images Datasets	89
6.4	Malaria	93
6.4.1	Related Works	93
6.4.2	Malaria parasites morphology	102

7 WBCs Segmentation	107
7.1 WBC segmentation by samples	108
7.1.1 On Mean Shift Technique	109
7.1.2 Experimental evaluation	110
7.1.3 System Implementation	110
7.1.4 System extension	114
7.2 Discussion	115
8 WBCs Identification and Counting	117
8.1 Agglomerates Identification	117
8.2 WBCs detection and separation from agglomerates	118
8.2.1 WBC detection with CHT	119
8.2.2 WBC separation from clumps with VFC	120
8.3 WBC detection with VFC	121
8.3.1 On Vector Field Convolution	121
8.4 Image Cleaning	127
8.5 WBC Count	130
8.6 Discussion	130
9 RBC analysis	135
9.1 RBC segmentation	135
9.2 MP-IDB: Malaria Parasite Dataset	139
9.2.1 Homomorphic filtering for image enhancement	141
III Conclusions	145
Bibliography	151
A Hematopoiesis	167
A.1 Granulopoiesis	169
A.2 Monopoiesis	171
A.3 Lymphopoiesis	172
A.4 Erythropoiesis	173
A.4.1 Erythrocyte Variations	174
A.4.2 Erythrocyte Inclusions	176
A.5 Megakaryocytopoiesis	177
A.5.1 Malaria parasites	178

List of Figures

2.1	Example of operations on the histogram. Left: original greyscale image. Center: contrast stretched image. Right: result of histogram equalization with 64 bins.	32
2.2	Example of Gaussian smoothing filter application on a grey level image. From left to right: original greyscale image, filtered images with $\sigma = 2, 4$ and 8	33
2.3	Example of sharpening operators. From left to right: original greyscale image, application of Laplacian filter, gradient operator and unsharp filter.	34
2.4	Example of primary spaces image representation. From left to right and from top to bottom: RGB image, XYZ image, CYMK image; CMY image, CMK image, MYK image.	36
2.5	Example of Luminance-Chrominance spaces. From left to right: RGB, Ycbcr and Lab images.	38
2.6	Example of perceptual spaces. From left to right: RGB, HSV, HSL images.	39
3.1	Example of global thresholding. From left to right: RGB original image, binary image resulting from a 0.6 global threshold value, binary image after Otsu threshold, which produced an optimal global threshold value of 0.4157.	42
3.2	Example of Zack algorithm.	43
3.3	Example of fuzzy thresholding. From left to right: RGB original image; 2 class c-means fuzzy thresholded image (threshold value = 0.4347); 3 class c-means fuzzy thresholded image (threshold value = 0.7362).	44
3.4	Example of local thresholding. Left: RGB original image; local thresholded image with uniform sensitivity given to pixels belonging to background and everything else. WBCs zones are well distinguished from the other objects.	45
3.5	Example of edge based segmentation. Left: RGB original image; binary mask obtained with LoG operator; binary mask obtained with Canny operator.	46

3.6 Example of deformable model segmentation, by using Active Contour strategy. From left to right: RGB original image; seed region indicates the region to analyse; segmentation result after 250 iterations of Active Contour.	47
3.7 Example of region growing application. From left to right: RGB original image; segmentation result after region growing application starting from a WBC nuclei seed point in the centre of image; superimposition of segmentation result over original image indicating the obtained region.	48
3.8 Example of split and merge application. From left to right: RGB original image; gray level converted image; split and merge segmentation results by using quadrants from 512×512 down to 1×1	49
4.1 The LBP operators $LBP_{8,1}$ and $LBP_{16,2}$, respectively	65
6.1 Peripheral blood smear components: a real image and a schematic representation.	83
6.2 Different illumination conditions generate distinct images because of the absence of a standardized acquisition procedure. From left to right: acquisition of the same smear with four microscope's brightness levels. Courtesy of CHUV, Lausanne.	83
6.3 A comparison between different types of WBCs: neutrophils, basophils, eosinophils, monocytes and lymphocytes.	85
6.4 A comparison between lymphocytes suffering from ALL: a healthy lymphocyte, followed by lymphoblasts classified as L1, L2 and L3, respectively, according to the FAB [BCMT ⁺ 76].	85
6.5 Crop of a sample image taken from ALL-IDB1. It represents a leukocyte clump.	88
6.6 Sample images from the ALL-IDB1	90
6.7 Sample images from the ALL-IDB2	91
6.8 From left to right: original images from the ALL-IDB1 database, ground-truth for whole leukocyte, only nuclei and RBCs	91
6.9 From left to right: original images from the ALL-IDB2 database, ground-truth for whole leukocyte, only nucleus and only cytoplasm	91
6.10 From left to right: sample image from IUMS-IDB and SMC-IDB.	92
6.11 Types of human malaria parasites: from left to right, <i>P. falciparum</i> in its schizont stage, <i>P. vivax</i> in two gametocytes specimens and one ring stage, <i>P. ovale</i> in its ring stage, <i>P. malariae</i> in its schizont stage. Courtesy of CHUV, Lausanne.	94

6.12 Types of malaria parasites: from top left, clockwise, <i>P. Falciparum</i> in its schizont stage, <i>P. Vivax</i> in a gametocytes specimen, <i>P. Malariae</i> in its schizont stage, <i>P. Ovale</i> in its ring stage. All parasites have been surrounded with a yellow box. Underneath, from left to right: crops of <i>P. Falciparum</i> schizont, <i>P. Vivax</i> gametocyte, <i>P. Ovale</i> ring and <i>P. Malariae</i> schizont, taken from the boxes. Courtesy of CHUV, Lausanne.	103
6.13 Examples of malaria parasite stages. From top left: <i>P.falciparum</i> ring, trophozoite, schizont, gametocyte; <i>P.ovale</i> ring, trophozoite, schizont, gametocyte; <i>P.vivax</i> ring, developed trophozoite, gametocyte. [LDRK18]	104
6.14 Example of blood smear image acquired with a good coloration and illumination scheme. Three different regions of interest characterize the image: an eosinophil granulocyte on the bottom left (yellow bounding box), a schizont Plasmodium Falciparum on bottom center (green bounding box) and the erythrocytes. Please note that some platelets are also present (blue bounding box). Courtesy of CHUV, Lausanne.	105
7.1 From left to right: extracted image from ALL-IDB2, segmentation result for nucleus an cytoplasm with the first strategy, segmentation result for nucleus an cytoplasm with the second strategy; segmentation result for nucleus an cytoplasm with the third strategy. First strategy tends to misclassify lighter pixels belonging to RBCs, that are quite similar to WBC cytoplasm. Second strategy improve the results of the first one and it misclassifies only RBC nuclei, that are quite light. Final strategy gives the expected results by classifying WBCs pixels correctly.	111
7.2 Examples of training samples candidates. From From left to right: original image from ALL-IDB2, same image after three iteration of Mean Shift algorithm; same image thresholded to emphasize WBC nuclei (light blue) and cytoplasm (blue).	112
7.3 Original images from the ALL-IDB1 database, ground-truth for whole leukocyte, ground-truth for leukocyte nuclei and final segmentation result.	113
7.4 Examples of ROI selection for WBCs, RBCs and plasma.	115
8.1 Examples of leukocytes identified as grouped.	118
8.2 Leukocyte detection phases: connected components, single objects detection, artifact removal, agglomerates crop and detected leukocytes.	120
8.3 Application of circular Hough transform to the whole image using an unknown radius and a wrong threshold.	121

8.4	RBC image's G channel extraction. The WBCs are highlighted with respect to the other regions.	122
8.5	Example of VFC detection procedure. Top, from left to right: original image, VFC right component, VFC left component, distance transform image. Bottom, from left to right: external energy image, overlay image and opened image.	126
8.6	Application of complete VFC-based pipeline. Left: oversegmented image, right: final result, all WBCs are split.	126
8.7	Final separation results and image cleaning results.	127
8.8	Left to right: grey level sub-image, binary sub-image, whole leukocyte sub-image, nucleus sub-image and cytoplasm sub-image.	128
8.9	Original images superimposed with the contours of the leukocytes identified.	129
8.10	Top: from left to right, images extracted from ALL-IDB, IUSMS-IDB and SMC-IDDB, respectively. Bottom: from left to right, the final segmentation results for each image on top.	132
8.11	Original and segmented images from ALL-IDB1, IUMS-IDB, SMC-IDB and related SVM performances.	133
9.1	From top left to bottom right: shape and colour abnormalities: spherocyte, elliptocyte, tear, sickle, acanthocyte, echinocyte, keratocyte, byte, stomatocyte, target, schistocyte and rouleaux formation. (Bottom) Inclusions: howell-jolly bodies, siderotic granules, basophilic stippling, Heinz bodies, malaria and nucleated RBC.	136
9.2	Pipeline of this approach.	137
9.3	Segmentation results after ROI selection for two and three classes. Blue represents WBCs, while light blue represents RBCs.	138
9.4	From left to right: same smear acquired with four microscope brightness levels. Different illumination conditions could generate unconventional colour schemes in images. Courtesy of CHUV, Lausanne.	140
9.5	From left to right: original RGB image, Saturation channel of HSV space, Histogram of the saturation plane with a vertical line indicating the Otsu threshold. Underneath: segmentation, polynomial estimation of the background evolution. Courtesy of CHUV, Lausanne.	142
9.6	From left to right: original RGB image, corrected image by the described method with S channel, corrected image by the described method with G channel, horizontal profiles at the center of the image. In red, the original image, in blue, the proposed with S channel, and in green the proposed method with G channel. Courtesy of CHUV, Lausanne.	142
9.7	Bone marrow smear image. Erythroid and granulocytic precursors are present. Courtesy of [Uta18]	149

A.1	Hematopoietic process.	168
A.2	Granulopoiesis.	169
A.3	Granulocyte toxic changes.	171
A.4	Monopoiesis.	171
A.5	Lymphopoiesis.	172
A.6	Erythropoiesis.	173
A.7	Poikilocytosis.	175
A.8	Erythrocyte Inclusions.	176
A.9	Megakaryocytopoiesis.	177
A.10	Examples of malaria parasite stages. First row, from left to right: <i>P. falciparum</i> ring, trophozoite, schizont, gametocyte; second row, from left to right: <i>P. ovale</i> ring, trophozoite, schizont, gametocyte; third row, from left to right: <i>P. malariae</i> ring, trophozoite, schizont, gametocyte; last row, from left to right: <i>P. vivax</i> ring, developed trophozoite, gametocyte. Courtesy of CHUV, Lausanne.	179
A.11	Plasmodium Falciparum schematic stages of life. Courtesy of [CDC18]. Fig. 1: Normal red cell; Figs. 2-18: Trophozoites (among these, Figs. 2-10 correspond to ring-stage trophozoites); Figs. 19-26: Schizonts (Fig. 26 is a ruptured schizont); Figs. 27, 28: Mature macrogametocytes (female); Figs. 29, 30: Mature microgametocytes (male).	180
A.12	Plasmodium Malariae schematic stages of life. Courtesy of [CDC18]. Fig. 1: Normal red cell; Figs. 2-5: Young trophozoites (rings); Figs. 6-13: Trophozoites; Figs. 14-22: Schizonts; Fig. 23: Developing gametocyte; Fig. 24: Macrogametocyte (female); Fig. 25: Microgametocyte (male).	181
A.13	Plasmodium Falciparum schematic stages of life. Courtesy of [CDC18]. Fig. 1: Normal red cell; Figs. 2-5: Young trophozoites (Rings); Figs. 6-15: Trophozoites; Figs. 16-23: Schizonts; Fig. 24: Macrogametocytes (female); Fig. 25: Microgametocyte (male).	182
A.14	Plasmodium Vivax schematic stages of life. Courtesy of [CDC18]. Fig. 1: Normal red cell; Figs. 2-6: Young trophozoites (ring stage parasites); Figs. 7-18: Trophozoites; Figs. 19-27: Schizonts; Figs. 28 and 29: Macrogametocytes (female); Fig. 30: Microgametocyte (male).	183

List of Tables

7.1	Segmentation performances.	114
8.1	Detection performances of proposed WBC count methods compared with the state-of-the-art. Please note that "Det 1" stands for the method based on CHT and "Det 2" for the one based on VFC. ALL, IUMS and SMC are contraction of ALL-IDB, IUMS-IDB and SMC-IDB, respectively.	131
9.1	Detection and counting of both WBC and RBC performances compared with the state-of-the-art.	138
9.2	Composition of dataset's images	140

Acronyms

ALL Acute Lymphoblastic Leukaemia

ALL-IDB Acute Lymphoblastic Leukaemia Image Database

ANN Artificial Neural Networks

ASM Angular Second Moment

Aut Autocorrelation

CAD Computer Aided Diagnosis

Con Contrast

Cor Correlation

CP Cluster Prominence

CS Cluster Shade

DAG Directed Acyclic Graph

DAve Difference Average

DEnt Difference Entropy

DVar Difference Variance

Ene Energy

Ent Entropy

FN False Negative

FNR False Negative Rate

FP False Positive

FPR False Positive Rate

FS Fuzzy Sets

GLCM Gray Level Co-occurrence Matrix

GLDM Gray Level Difference Matrix

GLN Grey Level Non-uniformity

GLRLM Gray Level Run-Length Matrix

HGLRE High Grey Level Run Emphasis

Hom Homogeneity

HSC Hematopoietic Stem Cells

IDM Inverse Difference Moment

LBP Local Binary Pattern

LGLRE Low Grey Level Run Emphasis

LoG Laplacian of Gaussian

LRE Long Run Emphasis

LRHGLE Long Run High Grey Level Emphasis

LRLGLE Long Run Low Grey Level Emphasis

MC Measure of Correlation

MP Maximum Probability

NN Nearest Neighbors

PCA Principal Component Analysis

PM Product Moment

RBC Red Blood Cell

RBF Radial Basis Function

RLN Run Length Non-uniformity

RP Run Percentage

SAve Sum Average

SEnt Sum Entropy

SRE Short Run Emphasis

SRHGLE Short Run High Grey Level Emphasis

SRLGLE Short Run Low Grey Level Emphasis

SVar Sum Variance

SVM Support Vector Machine

TN True Negative

TNR True Negative Rate

TP True Positive

TPR True Positive Rate

Var Variance

WBC White Blood Cell

WBCC White Blood Cell Count

Chapter 1

Introduction

The visual analysis of bodily fluids and tissues focused on diagnosing diseases using a microscope is called microscopic pathology, that is a sub-discipline of pathology. This kind of analysis still constitutes the final step to confirm if and which illness is present. Traditionally, *cytopathology* and *histopathology* compose microscopical pathology. Cytopathology refers to diagnosis based on the study of cytological images, that are characterized by the presence of single cells and cell clusters, while histopathology relates to diagnosis based on the study of histological images and involves examination of entire human tissues composed of an association of cells into structures which deal with a particular function.

The measurements and characterization of cells from cytological images can be performed automatically since the late 1950s, when Coulter [Cou56] developed a method for sizing and counting cells, using electrical impedance directly from the blood sample. Nowadays the technique proposed by Coulter has been improved to analyze different particles. A further improvement of this approach is the Flow Cytometry, used to measure and examine multiple physical characteristics, chemical properties simultaneously and defines the maturation stage of particles, as they flow in a fluid stream rapidly and they pass one-at-a-time through at least one laser. Particle components are fluorescently labeled and then excited by the laser to emit light at varying wavelengths, and then distinguished using an optical-to-electronic coupling system that records the way in which the cell emits fluorescence and scatters incident light from the laser. The properties measured include size, morphology, granularity and internal and external structure of cells in question. This system, due to its complexity, needs many quality controls. Some of these controls are performed internally by the same instrument, but others must be executed externally to check the performance of each component.

1.1 CAD - Computer Aided Diagnosis

The microscope is still an essential tool to the pathology laboratory today since pathologists continue to perform manual observation of samples. It can be used to check the results from an instrument or if a recalibration is needed. The manual microscopic examination involves numerous drawbacks, in particular, the results accuracy heavily depends on the operator skills. The operators develop their skills during a complex training period analyzing as many cases as possible of different pathology. Nevertheless many cases require different experts and technical opinions to reduce human error. The process of manual microscopic observation is prolonged and time-consuming, in particular, if it involves different operators for a single diagnosis. Digital microscopes are becoming routine pieces of equipment in laboratories, being a combination of a digital camera and a lens, can scan the samples and store the images for future review. Furthermore, digital microscopy adds high-resolution and spatial information that flow measurements cannot extract. Digital slides are also, by nature, more comfortable to share than physical slides thus increasing the possibility of consultations between two or more experts. Digital slides have also the potential to be numerically analyzed directly by computer algorithms, useful to automate the manual counting of structures, or for classifying the condition of the tissue. The extraction of image-based information by computer technology from the digital slide is also known as *Digital Pathology* and can be used both to speed up the process of diagnosis and to reduce uncertainty and subjectivity.

In the last few years, many Computer Aided Diagnosis (CAD) system have appeared to automate or aid some stages of the diagnostic process, also motivated by the presence of equipment which allows obtaining slides with good quality automatically. However, automatic interpretation of microscopy medical images is still an open research question. In particular, the primary challenge when developing CAD systems is the creation of an effective method to extract meaningful information from the images, such as the cells number in the film or the position of the different structures in a tissue. These issues become more complex, concerning artificial vision, considering that there is not a color standardization for the staining and acquisition of digital slides. There is a considerable color variability between different slides, due to the quality of the biological sample and the sample preparation, such as the quantity of dye used during the staining procedure, or due to different acquisition system and the image capturing parameters, such as the environment illumination. Furthermore, such variability may be present in the same slide, in particular, the presence of uneven lighting, with a central area very bright and shading areas more marked towards the corners. Excessive use of the microscope light can cause this problem.

1.2 Contributions

In this thesis, there is an in-depth analysis of the unsolved issues in Computer-Aided Diagnosis from digital microscopy images, mainly acquired from peripheral blood smears. Different solutions have been analyzed and proposed. Three study cases can be distinguished: White Blood Cells analysis with leukemia correlation, Red Blood Cells analysis with malaria parasites correlation and histological tissues analysis. Particular attention has been given to the extraction of useful information from the digital images and the development of dataset-independent algorithms. In particular, the proposed framework has been tested over well known public datasets for what concerns WBC analysis, while a comprehensive dataset for RBC cells analysis has been introduced and published by our own. Cells count and clumps separation have been addressed in our studies. A crucial step in this kind of work certainly regards the segmentation step, which has several issues: some algorithms, able to isolate the cells of interest from images acquired in different illumination condition and stained with distinct staining have been realized. A correct segmentation step and a subsequent count of the cells permit to manage each cell singularly, and then to diagnose the presence of leukemia, in WBC analysis, or malaria, in RBC analysis. Since the importance of this kind of diagnosis different ensembles of descriptors and classifiers have been evaluated to provide a result as accurate as possible. In the proposed framework no object detection or segmentation method is needed, since every segmentation algorithm, applied to histological images, can produce a considerable number of regions and structures, which is extremely difficult to manage singularly. The overall procedure instead is based on the textures analysis, being the most suitable to analyze the tissue structure. Also, great importance has been given to the analysis of colors, considered one of the most interesting contents to be examined in the histological images, studying not only the internal correlation of various colors but also by analyzing the relationship between different colors. Moreover, further work has been realized to extend the WBC analysis framework and to include an in-depth RBC analysis, in particular, devoted to malaria parasites analysis. It aims to propose the first public dataset of blood samples afflicted by malaria, specifically designed to evaluate and compare algorithms for segmentation and classification of malaria parasite species. Every image is provided with its related ground truth and parasites classification of type and stage of life. The primary purpose is to offer a new comparative test tool to the image processing and pattern matching communities, to encourage and improve computer-aided malaria parasites analysis. The scientific results obtained during this Ph.D. work and described in this thesis also appeared in related publications, following listed:

- C. Di Ruberto, A. Loddo, L. Putzu, "A Multiple Classifier Learning by Sampling System for White Blood Cells Segmentation", G. Azzopardi, N. Petkov Eds. Computer Analysis of Images and Patterns - 16th International Conference, CAIP 2015, Valletta, Malta, September 2-4, 2015 Proceedings, Part I.

Lecture Notes in Computer Science 9256, Springer 2015, pp. 415-425, ISBN 978-3-319-23191-4.

- C. Di Ruberto, A. Loddo, L. Putzu, " Learning by Sampling for White Blood Cells Segmentation", V. Murino, E. Puppo Eds.: Image Analysis and Processing - ICIAP 2015 - 18th International Conference, Genoa, Italy, September 7-11, 2015, Proceedings, Part I. Lecture Notes in Computer Science 9279, Springer 2015, pp. 557-567, ISBN 978-3-319-23230-0.
- C. Di Ruberto, A. Loddo, L. Putzu. Peripheral Blood Image Analysis. Proceedings of the Doctoral Consortium, 11th Joint Conference on Computer Vision, Imaging and Computer Graphics Theory and Applications, VISIGRAPP 2016; Pages 15-23.
- C. Di Ruberto, A. Loddo, L. Putzu. A Leucocytes Count System from Blood Smear Images: Segmentation and Counting of White Blood Cells based on Learning by Sampling. Machine Vision and Applications; Volume 27, Issue 8, November 2016, Pages 1151-1160.
- C. Di Ruberto, A. Loddo, L. Putzu., G. Fenu A Computer-Aided System for Differential Count from Peripheral Blood Cell Images. Proceedings of the 12th International Conference on Signal Image Technology & Internet-Based Systems; 2016, Pages 112-118.
- A. Loddo, C. Di Ruberto, L. Putzu Histological Image Analysis by Invariant Descriptors. Proceedings of the 19th International Conference on Image Analysis and Processing, ICIAP 2017; LNCS 2017, vol. 10484, Pages 345-356.
- S. Porcu, C. Di Ruberto, A. Loddo, L. Putzu. White Blood Cells Counting Via Vector Field Convolution Nuclei Segmentation. Proceedings of the 13th International Joint Conference on Computer Vision, Imaging and Computer Graphics Theory and Applications, Vol. 4: VISAPP, 227-234, 2018, January 27-29, 2018 Funchal, Madeira, Portugal.
- A. Loddo, C. Di Ruberto, M. Kocher. Recent Advances of Malaria Parasites Detection Systems Based on Mathematical Morphology. Sensors. Volume 18, number 2, Pages 513, 2018.
- A. Loddo, C. Di Ruberto, M. Kocher, Guy Prod'Hom. MP-IDB: The Malaria Parasite image database for image processing and analysis. SaMBA workshop, MICCAI 2018.

1.3 Dissertation structure

This dissertation describes the work mentioned above in detail. It is organized as follows:

- Part I illustrates the phases of a typical CAD system schema for digital microscope images analysis. Four main steps have been highlighted and then analyzed in detail in chapters 2, 3, 4 and 5, namely pre-processing, segmentation, feature extraction, and classification respectively. We give an idea of the most used techniques and illustrating the basic concepts useful to the comprehension of the proposed CAD systems.
- Part II describes the proposed CAD system for peripheral blood image analysis. Chapter 6 contains an extended background of the topics and materials this dissertation takes on, that is a background on hematology and peripheral blood cells, a description of ALL and malaria analysis with references to previous works and to the datasets used to experiment possible solutions. Then chapter 7 shows three different approaches for segmentation, chapter 8 illustrates a method for leukocyte identification and count, while chapter 9 explains the system extension to erythrocyte segmentation to realize a complete blood cells segmenter.
- Part III concludes the dissertation and gives some final comments on the proposed approaches, discussing the choices made with the obtained results. The experimental results obtained have brought to further ideas for the future, not just to improve the overall procedures but also to extend the proposed CAD systems to further issues and to different medical problems.

Appendix A outlines the types of diseases that are directly connected with an abnormal number of cells in the peripheral bloodstream and shows how the presence of diseases or parasites may affect the morphology of the cells themselves.

Part I

Digital Microscopy CAD

The medical community, typically, has been established to take care of human health with knowledgeable and expert clinicians, like radiologists, hematologists, or health science specialists. Nowadays, technology provides an opportunity for having faster and more accurate tools, e.g., X-ray machines, CBC machines, and MRI. These automated medical tools are essential for diagnosing patients' health conditions. In this context, CAD systems have recently gained attention because they could offer a valid help to clinicians. They have to deal with different medical fields and with issues related to images and data to manage. In particular, CAD systems dealing with images acquired with a digital microscope have to face additional issues like the variations of illumination and acquisition conditions or the different types of smear staining. Despite the previously listed issues, CAD systems for digital microscope based on image processing techniques generally consist of the following phases:

- Image pre-processing: noise suppression added to the image during the phase of acquisition and improvement of the luminance and contrast of the images.
- Segmentation: partitioning the image to isolate the objects of interest in the image. This phase is the most important in the automatic analysis of images, as from the result of the segmentation depends on the result of the entire analysis.
- Feature extraction: feature extraction of previously segmented objects, necessary for subsequent classification.
- Classification: assignment of segmented objects to a specific class. If present, any disease is determined through this phase.

In general, it is possible that some CAD systems do not need to use all the mentioned phases. As an example, pre-processing could be avoided if images have been captured with the most recent microscopes which produce high-quality images with a low percentage of imperfections or artifacts. Conversely, some phases can be repeated multiple times in order to deal with different issues. For instance, performing numerous stages of segmentation is very frequent in peripheral blood smear images analysis, for example using the first segmentation to firstly identify the cells and then to separate the components of the cells themselves. The following chapters give an overview of the most used techniques in the different phases of a typical CAD system and the basic concepts applied to the proposed methods for peripheral blood image analysis, described in part II will be depicted.

Chapter 2

Image Pre-processing

Pre-processing is a common name for operations with images at the lowest level of abstraction. The primary purpose is an improvement of the image condition by means of some operations in order to suppress unwanted distortions, such as noise or artifacts, or enhance some image features for further processing like, for example, enhancing or stretching the contrast, separating, in a better way, the objects of interest from the background. It is worth to indicate that pre-processing methods may be unnecessary on CAD systems for several reasons: first of all, image acquisition tools, like modern microscopes, are equipped with high-level cameras, and they can produce excellent quality images. Secondarily, this kind of operations could alter a lot, or even suppress, the structures of the cells which are essential for further analysis phases. Typically, images structures are represented with an appropriate definition with only a small quantization noise, or they can directly be acquired in a low contrast environment. For these reasons the most used pre-processing operations are:

- Histogram operations
- Local pre-processing operations:
 - Smoothing operators
 - Sharpening operators

2.1 Operations on the histogram

An image histogram is a representation of the tonal distribution in a digital image. A good example is the grey level histogram. It provides the frequency of pixels' intensity values inside the image and indicates the number of pixels having each grey level. It also gives useful information about the image, such as the number of modes, the presence of a dominant peak or the grey levels distribution along the histogram.

If the image has a low contrast, it means that all the pixels values are condensed towards a side of the histogram. On the other hand, a bimodal histogram often denotes the presence of a fairly homogeneous brightness object on a nearly constant background. Operating on the histogram means defining a mapping h from the initial space of grey levels in a new grey levels space $h : [0..255] \rightarrow [0..255]$, whose application to the image I , is the replacement of grey level $I[i, j]$ with $h(I[i, j])$. Therefore, it is possible to increase the contrast within the image, equalize the histogram and highlight or hide some image details, by defining the appropriate mapping. The *contrast stretching* operation is necessary when the histogram values are not distributed over the entire frequency range. Stretching the histogram is a solution to correct this situation, by mapping the minimum and the maximum value of the original image with the value 0 and 255, respectively. This operation is common for cytometric image analysis, as it allows good separation of foreground objects from the background. Figure 2.1 shows an example of contrast stretching. The *histogram equalization* operation is essential because it is often used to make images captured in different lighting conditions comparable. The equalization is achieved by defining a mapping that equally distributes the pixels values. This operation produces a histogram (theoretically) flat, considering $h(x)$ as the histogram of the original image, it can be changed through the use of the function $y = y(x)$, so that the histogram $g(y)$ of the resulting image becomes constant for each intensity value $g(y) = c$.

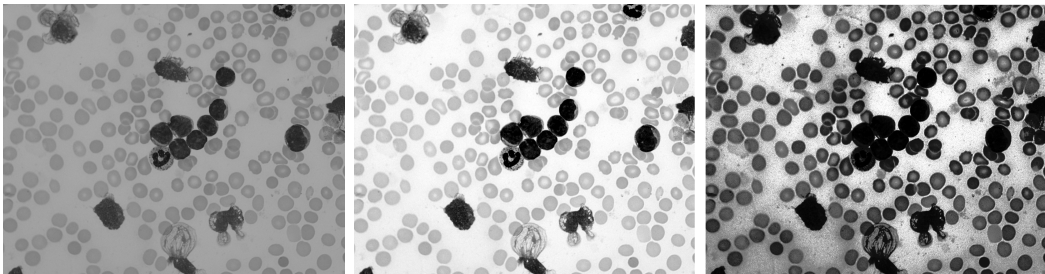


Figure 2.1: Example of operations on the histogram. Left: original greyscale image. Center: contrast stretched image. Right: result of histogram equalization with 64 bins.

2.2 Operations of local pre-processing

Local pre-processing ones operate on a small neighborhood of the original image pixels to calculate new pixel values of the resulting image rather than on the entire image. They are also called filtering operations since they make use of digital filters. The pixels neighborhood, used to calculate new intensity value, always needs to have odd cardinality, in such a way that the considered pixel lies in the middle of the neighborhood. Typically, the sizes are 3×3 , 5×5 or 7×7 . The filter used for the filtering operation has the same size as the considered pixel's neighborhood.

The values of the filter are used as a weight that is multiplied by the corresponding pixel values of the neighborhood and then added together to give rise to the new value of the pixel in the resulting image. We can distinguish between two groups of local pre-processing methods, in accordance with their ultimate goal. They are the smoothing and the sharpening operators.

2.2.1 Smoothing operators

The smoothing operators have the purpose of suppressing noise or other small unwanted details in images, using their redundancy. Unfortunately, as previously said, these operators tend to flatten also useful details such as objects' edges and the cell structures, even though they generally produce good results in the removal of impulsive noise. The most used smoothing operator is the *averaging filter*. It stores the average value of its neighborhood in the considered pixel. In this case, the results are acceptable if the noise has a smaller size than the objects of interest; in any case, the objects' contours are heavily altered. Average filters can also have different weight values, to properly reflect the characteristics of the Gaussian noise. They are also called Gaussian filters since they simulate the trend of a Gaussian curve. Fig. 2.2 represents an example. Another common smoothing operator is the *median filter*, which behaves similarly to the average filter. The only difference is that it stores the median value of its neighborhood in the considered pixel.

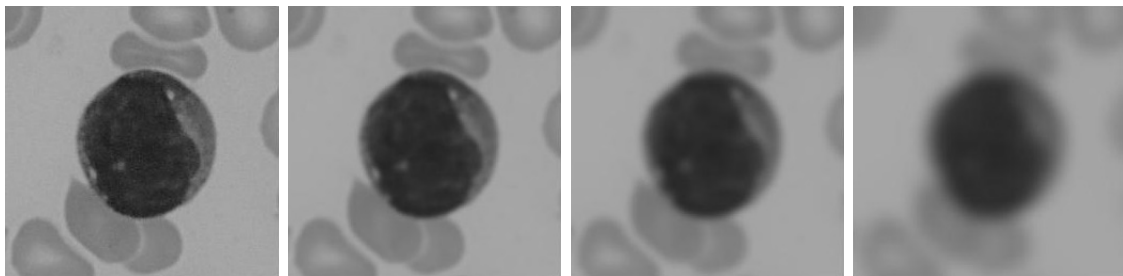


Figure 2.2: Example of Gaussian smoothing filter application on a grey level image. From left to right: original greyscale image, filtered images with $\sigma = 2, 4$ and 8 .

2.2.2 Sharpening operators

The sharpening operators have the purpose of highlighting the interesting details of the image, such as the edges of objects. Unfortunately, these operators tend to highlight also the noise present in the image, however they improve the perceived picture detail. These operators depend on the use of local derivatives of the image. Since the image is a discrete function, the traditional definition of derivative cannot be applied. In digital images, the operator used for the first derivative is the intensity difference between adjacent pixels. In most cases, the sharpening operators use the

second derivatives, since they are more sensitive to intensity variations. The most used sharpening operator is the *Laplacian filter* that brings the desired sharpening effect by subtracting the Laplacian filtered image from the original one. Another useful sharpening operator is the *gradient operator* that makes use of the image gradient to detect and improve the edges. An edge is a set of connected pixels (4 or 8 connected) with sharp changes in brightness, so it can be detected as any transition of grey levels, where the slope of this transition is proportional to how the edge is sharp. Such image function change can be described by the gradient pointing in the direction in which the function has its most significant growth. Prewitt, Sobel, Kirsch, and Robinson are examples of operators that can correctly determine the gradient direction by using the first derivative. Another common sharpening operator used in most of the commercial products to make the image noticeably sharper is the *Unsharp filter*. It is a simple sharpening operator which takes its name from the fact that it enhances edges and other high-frequency components in an image via a procedure that subtracts a smoothed (or unsharp) version of the image from the original one. Fig. 2.3 shows some examples of the described sharpening operators.

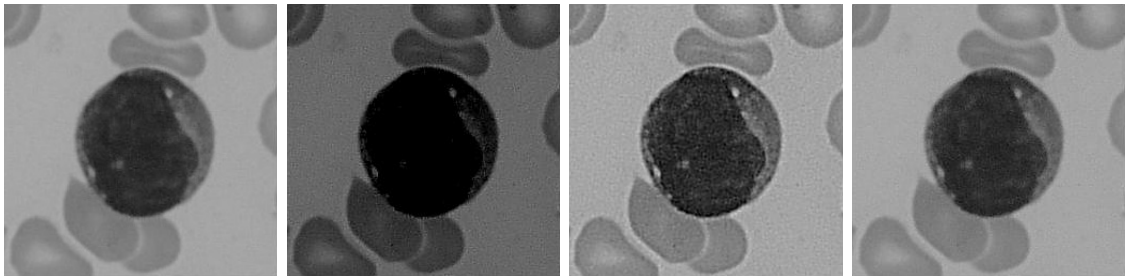


Figure 2.3: Example of sharpening operators. From left to right: original greyscale image, application of Laplacian filter, gradient operator and unsharp filter.

2.3 Color and Color Spaces

Color is very important in CAD systems since the hematologists stain blood to highlight spatial structures. The color is the brain's reaction to a specific visual stimulus. It is incredibly subjective and personal, thus trying to attribute numbers to the brains reaction to visual stimuli is very difficult. Color spaces aim to aid the process of describing the colors, either between people or between machines or programs. The presence of more than one color space is since different color spaces can work better in specific applications, for example, some devices have limiting factors that dictate the size and type of color space used. Thus, some color spaces are tied to a specific piece device (device dependent) while others are equally valid on whatever device they are used (device independent). The standard families are

primary, luminance-chrominance, and perceptual spaces [VMP03, BVMP04] and they classify color spaces into a few categories, concerning their definitions and their properties.

2.3.1 Primary Spaces

The primary spaces are based on the trichromatic theory of color vision, also known as the Young-Helmholtz theory of color vision. It states that there are three receptors in the retina that are responsible for the perception of color. One receptor is sensitive to the color green, another to the color blue and a third to the color red. These three colors can then be combined to form any visible color in the spectrum. The primary spaces assume that it is possible to match any color by mixing appropriate amounts of the three primary colors. Examples of primary spaces are the real RGB, the subtractive CMY(K), and the imaginary XYZ. The most widely used color space indeed is the RGB color space, in which a color point in the space is characterized by three color components of the corresponding pixel which are red (R), green (G), and blue (B). In general, color images are acquired through the RGB color space, called the image acquisition color space. Therefore, all the color spaces are expressed thanks to transformations performed on the R, G and B channels. As previously said, CMY(K) is the subtractive color space and can be obtained easily from a set of RGB values by subtracting the individual RGB values from 1, since a pure cyan (C) surface does not contain R, a pure magenta (M) surface does not contain G and a pure yellow (Y) surface does not contain B. So, the equation is:

$$\begin{bmatrix} C \\ M \\ Y \end{bmatrix} = \begin{bmatrix} 1 \\ 1 \\ 1 \end{bmatrix} - \begin{bmatrix} R \\ G \\ B \end{bmatrix} \quad (2.1)$$

with the assumption that, in general, all color values have been normalized to the range [0, 1]. In general, this color space is used in color printers and copiers that internally perform this conversion. According to the equation, equal amounts of the color channels should produce black. In practice, however, their combination for printing produces only a dark color far from the real black. Thus, to produce a pure black a fourth color has been added, giving rise to the CMYK color space. In this case, the conversions start from the just computed CMY, by finding the black (K) channel and then correcting the complementary colors based on the value of K.

$$\begin{aligned} K &= \min(c, m, y) \\ C &= c - K \\ M &= m - K \\ Y &= y - K \end{aligned} \quad (2.2)$$

The XYZ colour space is obtained from the RGB colour space using the following equation:

$$\begin{bmatrix} X \\ Y \\ Z \end{bmatrix} = \begin{bmatrix} 0.412 & 0.357 & 0.180 \\ 0.212 & 0.715 & 0.072 \\ 0.019 & 0.119 & 0.950 \end{bmatrix} \cdot \begin{bmatrix} R \\ G \\ B \end{bmatrix} \quad (2.3)$$

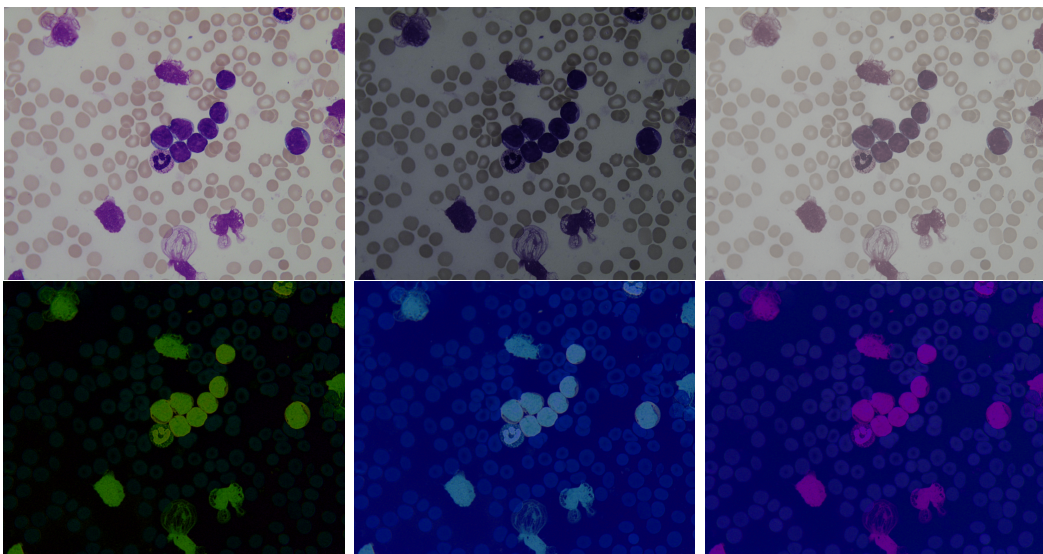


Figure 2.4: Example of primary spaces image representation. From left to right and from top to bottom: RGB image, XYZ image, CMYK image; CMY image, YUV image, MYK image.

2.3.2 Luminance-Chrominance Spaces

The luminance-chrominance spaces are used if it is useful to separate the color definition into luminance, represented by one component, and chrominance, represented by the two other components. Among these color spaces, there are the television transmission color spaces, sometimes known as transmission primaries, YIQ, and YUV for analogical standard and YCbCr for the digital standard. For this reason, only the YCbCr has been taken into account. It could be obtained from the RGB color space using the following equation:

$$\begin{bmatrix} Y \\ Cb \\ Cr \end{bmatrix} = \begin{bmatrix} 0 \\ 128 \\ 128 \end{bmatrix} + \begin{bmatrix} 0.299 & 0.587 & 0.114 \\ -0.169 & -0.331 & 0.500 \\ 0.500 & -0.419 & -0.081 \end{bmatrix} \cdot \begin{bmatrix} R \\ G \\ B \end{bmatrix} \quad (2.4)$$

The International Commission of Illumination (CIE) has defined a system that classifies color according to the human visual system in order to specify any color in

terms of its CIE coordinates. There are two main CIE based color spaces, CIELUV (Luv) and CIELAB (Lab). They are nearly linear with visual perception with the L parameter that has a good correlation with perceived lightness and the other two parameters that express the chrominance. Fig. 2.5 shows some examples. They are based on the XYZ color space so they could be obtained by a conversion from the XYZ color space using the following equations:

Luv

$$\begin{aligned} L &= \begin{cases} 116\sqrt[3]{y_r} - 16, & y_r > 0.008856 \\ 903.3y_r, & y_r \leq 0.008856 \end{cases} \\ u &= 13L(u' - u'_r) \\ v &= 13L(v' - v'_r) \end{aligned} \quad (2.5)$$

where

$$\begin{aligned} y_r &= \frac{Y}{Y_r} \\ u' &= \frac{4X}{X + 15Y + 3Z} \\ v' &= \frac{9Y}{X + 15Y + 3Z} \\ u'_r &= \frac{4X_r}{X_r + 15Y_r + 3Z_r} \\ v'_r &= \frac{9Y_r}{X_r + 15Y_r + 3Z_r} \end{aligned}$$

Lab

$$\begin{aligned} L &= 116 \cdot h\left(\frac{Y}{Y_r}\right) - 16 \\ a &= 500 \left[h\left(\frac{X}{X_r}\right) \left(\frac{Y}{Y_r}\right) \right] \\ b &= 200 \left[h\left(\frac{Y}{Y_r}\right) \left(\frac{Z}{Z_r}\right) \right] \end{aligned} \quad (2.6)$$

where

$$h(q) = \begin{cases} \sqrt[3]{q}, & q > 0.008856 \\ 7.787q + 16/116, & q \leq 0.008856 \end{cases}$$

Both equations require a reference white X_r , Y_r and Z_r .

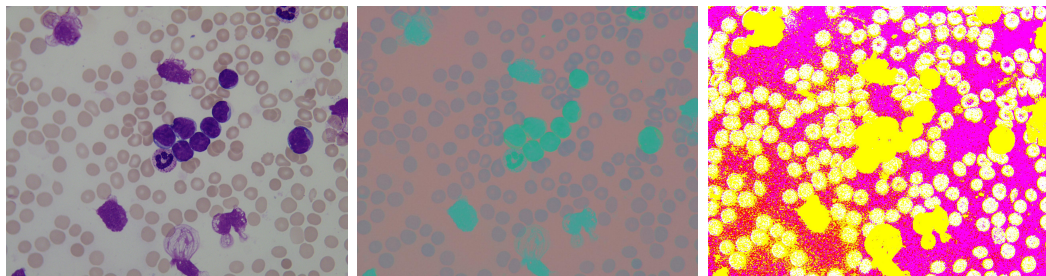


Figure 2.5: Example of Luminance-Chrominance spaces. From left to right: RGB, Ycbcr and Lab images.

2.3.3 Perceptual Spaces

The perceptual spaces try to quantify the subjective human color perception through Intensity, Hue and Saturation values. This family represents a wealth of similar color spaces, which include HSI (I stands for Intensity), HSV (V stands for Value), HSL (Hue Saturation Lightness), HCI (C stands for Chroma), and so on. Most of these color spaces are linear transforms from RGB and, consequently, are device dependent. Fig. 2.6 depicts some examples. Their advantage lies in the extremely intuitive manner of specifying color, selecting the desired hue and then modifying it slightly by adjusting its saturation and intensity values. Furthermore, the separation of the luminance component from color information is stated to have advantages in image processing. Here only the HSV color space has been taken into account since it is the most used perceptual space. It can be obtained from the RGB color space with the following equation:

$$\begin{aligned}
 Max &= \max(R, G, B) \\
 Min &= \min(R, G, B) \\
 \Delta &= Max - Min \\
 V &= Max \\
 S &= \frac{(\Delta)}{Max} \\
 H = & \begin{cases} 0, & \text{if } \Delta = 0 \\ 60^\circ \times \left(\frac{G-B}{\Delta} \text{ mod } 6 \right), & \text{if } R = Max \\ 60^\circ \times \left(\frac{B-R}{\Delta} + 2 \right), & \text{if } G = Max \\ 60^\circ \times \left(\frac{R-G}{\Delta} + 4 \right), & \text{if } B = Max \end{cases} \quad (2.7)
 \end{aligned}$$

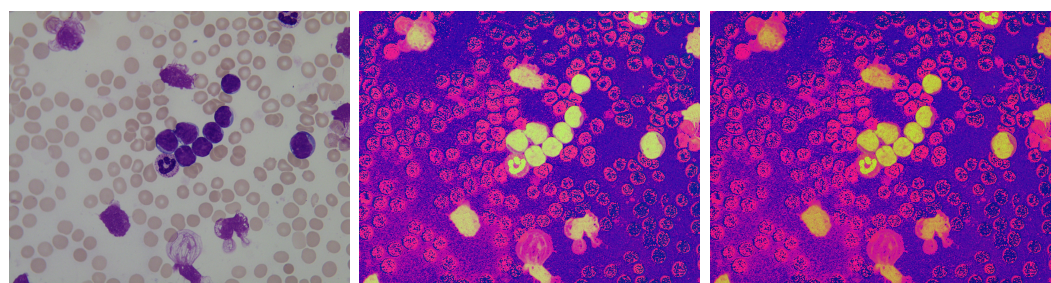


Figure 2.6: Example of perceptual spaces. From left to right: RGB, HSV, HSL images.

Chapter 3

Segmentation

Segmentation is one of the most important steps in image analysis because it permits to identify and separate, according to specific criteria of homogeneity and separation, the different regions contained in the image. Its main objective is to divide the image into parts that have a strong correlation either between them or with objects and areas of the real world contained in the image. The commonly used segmentation methods operate essentially relying on characteristics such as the value of brightness, color, and reflection of the individual pixels, identifying groups of pixels that correspond to spatially connected regions. As for many problems of image processing, no standard solution exist in general. Therefore, depending on the characteristics of the images to process, and especially of the objects to be segmented, different segmentation techniques can be applied. The simplest can often lead to unsatisfactory results, while the remaining are more powerful, but their drawback is a higher computational cost. For medical images analysis, two primary levels of segmentation exist: the first level aims to separate whole cells from the background and the second one seeks to separate the cells in their components like the nucleus from the cytoplasm in WBCs analysis or intracellular parasites in RBCs analysis, for example. The second segmentation level is quite common in cells analysis because the cell class depends on the morphological characteristics of its components. The segmentation techniques can be divided into three main categories: Pixel-Based, Edge-Based and Region Based.

3.1 Pixel Based or Thresholding

Thresholding is the most elementary and computationally cheaper technique for image segmentation, making use of a threshold operator that directly involves the image histogram. The hypothesis underlying this segmentation technique is that the pixels of an object approximately have the same brightness and, therefore, they can be separated from the background by thresholding brightness values. The problem becomes more difficult if the histogram presents more than two peaks because more

than one threshold value is necessary to separate the image objects. This technique presents some drawbacks, in particular, if the threshold is not chosen accurately, the detected objects can shrink or grow. This change in size can be crucial in applications where size is an essential parameter for the classification of the object itself. Moreover, an incorrect threshold value can cause a partial fusion of two or more objects together, making it impossible to perform its subsequent classification and identification. When the intensity distribution of objects and background is sufficiently distinct, it is possible to use a single global threshold [GW07, GWE04] applicable to the entire image. The value of this global threshold is calculated starting from an initial threshold value T between the minimum and maximum value of the histogram, that allows making the first segmentation. It produces two groups of pixels. Their values are averaged and used to calculate the new threshold value T . The process is then iterated until the difference between successive values of T is less than a predetermined parameter. This simple algorithm works well in situations where there is a clear valley between the various fashions histogram, relative to the background and objects.

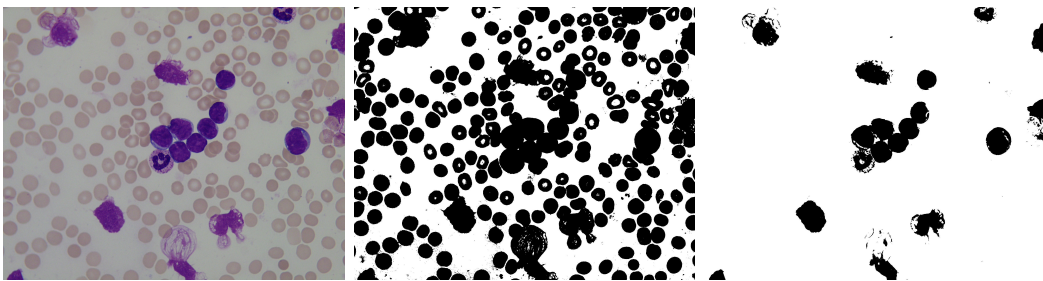


Figure 3.1: Example of global thresholding. From left to right: RGB original image, binary image resulting from a 0.6 global threshold value, binary image after Otsu threshold, which produced an optimal global threshold value of 0.4157.

3.1.1 Otsu Algorithm

The method of Otsu [Ots75] also performs a global threshold, but differently from the previous one allows to obtain an optimal threshold value, as it maximizes the variance between classes, as shown in Fig. 3.1. If well segmented, the classes are differentiated from the intensity value of their pixels. A threshold that gives the best separation between the classes in terms of intensity is an optimal threshold. The method of Otsu, moreover, can be extended to the segmentation of images that need more threshold values, since the measure of separability on which is based also extends to an arbitrary number of classes. It begins to lose meaning when the number of classes excessively increases since it works only with one variable which is the intensity. Typically, however, applications that require more than two threshold values are resolved with the use of other values in addition to the intensity, such as

the color or the entropy present in the histogram [KSW85].

3.1.2 Zack Algorithm

The Zack algorithm [ZRL77], also known as triangle method, differently from the other methods, does not work directly on the intensity value of the histogram, but it works on the image obtained from the histogram plot. It is called triangle method because it draws a sort of triangle, constructing a straight line that connects the highest histogram value $h[b_{max}]$ and the lowest one $h[b_{min}]$, where b_{max} and b_{min} indicate the values of the grey levels where the histogram $h[x]$ reaches its maximum and minimum, respectively. The distance d between the marked line and the histogram values between b_{min} and b_{max} is then calculated. The intensity value, where the distance d reaches its maximum, defines the threshold value. This algorithm is particularly effective and fast, indeed, differently from the ones seen before, it is computed directly on an image without any further iteration.

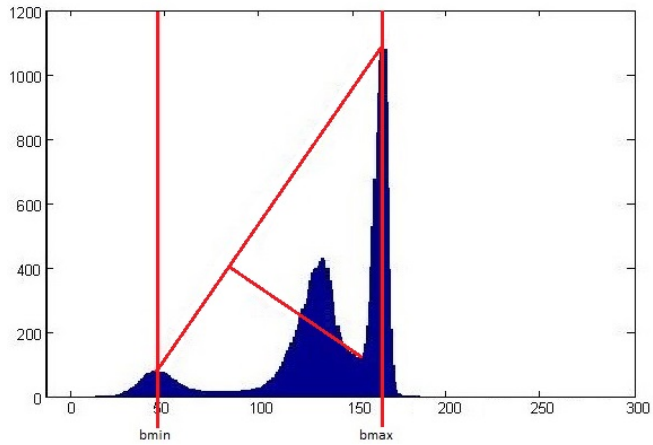


Figure 3.2: Example of Zack algorithm.

3.1.3 Fuzzy Threshold

The so far treated threshold algorithms are also called crisp techniques. They produce excellent results with sharp images and regions, but the segmentation process becomes complex in the presence of noise or imprecision. The nature of this imprecision in the image arises from the presence of uncertainty, that can lead to ill-defined regions. In this case, it is appropriate to avoid crisp segmentation and to prefer a fuzzy segmentation. Fuzzy threshold approaches are based on Fuzzy Sets (FSs) theory. Regions may be viewed as fuzzy subsets of the image. Several researchers have worked on fuzzy based thresholding techniques, in particular, to identify the best fuzzy measure able to separate the fuzzy subset, such as the fuzzy compactness

[PR88], the fuzzy similarity [RAS⁺⁰⁰] or the fuzzy divergence and gamma membership [CR03, MPCB⁺¹³]. Fuzzy threshold approaches segmentation performances are better than many crisp methods even though their computational performances are not comparable, as Fig. 3.3 shows. Crisp methods are entirely based on computations performed on the histogram, a 1-D array easily obtainable from the image, while fuzzy approaches are based on computations performed on the image, a 2-D array of size $M \times N$.



Figure 3.3: Example of fuzzy thresholding. From left to right: RGB original image; 2 class c-means thresholded image (threshold value = 0.4347); 3 class c-means thresholded image (threshold value = 0.7362).

3.1.4 Local Thresholding

Global thresholding algorithms may work properly in an area but produce unsatisfactory results in other areas when the background is not constant, and the contrast between objects varies unevenly. In this case, the use of local thresholding could be a better solution. The image is subdivided into rectangular overlapping sub-images, and the histogram of each of them is calculated. The sub-images must be big enough to include both the object and the background pixels. If the sub-image has a bimodal histogram, the minimum value between the two peaks is precisely the threshold. If the histogram is unimodal, the threshold value must be calculated by interpolating the thresholds of the adjacent sub-images, instead. In general, the local thresholding is computationally more expensive than the global one, although it is advantageous to segment objects from the background and to extract tiny and scattered variable regions. Fig. 3.4 shows an example.

3.2 Edge Based

This segmentation technique is not based on the intensity value of the pixels, but on the fact that an object to be identified must have a closed edge that surrounds it. This assumption is not always true but often verified. The edges of objects are preliminarily identified by applying suitable operators of edge detection. As

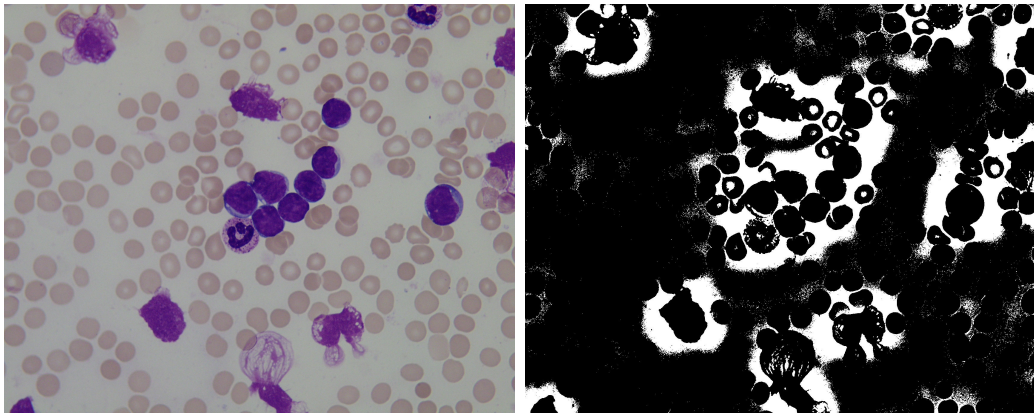


Figure 3.4: Example of local thresholding. Left: RGB original image; local thresholded image with uniform sensitivity given to pixels belonging to background and everything else. WBCs zones are well distinguished from the other objects.

said previously, an edge is a set of connected pixels (4 or 8 connected) that lies on the border of two regions, therefore presenting sharp brightness changes. There is a little difference between edge and boundary since the edge is a local concept while the boundary is an extended concept. Therefore the boundary of an object is composed of a series of edges. It is possible to carry out a threshold applied to the first derivative to detect only the edge. It is an operation that takes the name of non-maxima suppression, as it resets all the values in the first derivative which are not maximum. The chosen threshold value allows selecting more than one maximum points, as to have a contour wider but visible. Instead, if the threshold operation is applied to the second derivative, this operation takes the name of zero crossing and has the aim of seeking zero crossing points, necessary for the location of the edge points without distortion, avoiding the appearance of a double border. As previously mentioned, there are several implementations of filters on the first derivative, that can be applied directly to the search of the edges. In general, before the edge detection, a smoothing filter is applied to the image, to reduce both the noise and the edge thickness, so that the detection is more effective. The process works correctly if the signal is not noisy and if the edge is entirely localized in space and with small amplitude. An evolution of this approach is the Laplacian of Gaussian (LoG) filter with zero crossing and the Canny filter with non-maxima suppression. Examples are shown in Fig. 3.5.

3.2.1 LoG Operator

This edge detection approach, also known as Marr-Hildreth algorithm [MH80], is based on the second derivative of a function. The Laplacian operator is rarely used by itself for edge detection, as it is susceptible to noise, but it is used in conjunction with the Gaussian one, known precisely as Laplacian of Gaussian, LoG.

The fundamental characteristics of LoG are the Gaussian smoothing filter, used to reduce noise and to enlarge the edge, the Laplacian in two dimensions, the zero crossings in the second derivative and, finally, the edge location estimated with sub-pixel using the linear interpolation. The Gaussian filter is preferred because it applies an action of smoothing both in space and in frequency. Furthermore, the derivative of the Gaussian filter is independent from the considered image and can be pre-calculated analytically by reducing complexity. Once the Laplacian filter is applied, it is needed to search points in the image in which there is a zero crossing, considering only those zeros for which there is a significant change in all possible directions around zero.

3.2.2 Canny Operator

Even the Canny algorithm [Can86] uses a Gaussian filter for smoothing. Then the magnitude and direction of the gradient are calculated using different but finite approximations of partial derivatives. It applies the non-maxima suppression to the magnitude of the gradient, and finally, it uses the double threshold algorithm to find and link the edges. The use of the double threshold is necessary, considering that a single threshold would not lead to satisfactory results. For example, if the threshold is too low, it may detect too many false edges instead, if the threshold is too high some real edges may be lost. The use of two thresholds produces two different images and, of course, the image with the higher threshold will present a much smaller number of edges. Starting from this image, each edge is examined and compared with that one of the other images in search of edges that have been lost, and that can be linked to create a continuous boundary.

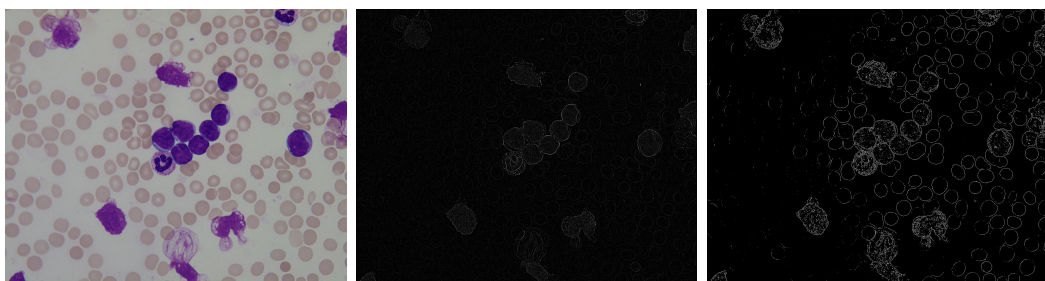


Figure 3.5: Example of edge based segmentation. Left: RGB original image; binary mask obtained with LoG operator; binary mask obtained with Canny operator.

3.2.3 Deformable Models

In medical image analysis, in many cases, the boundaries between the tissue structures and cell components are not clearly defined. The use of edge detection on

these images produces poor results, in particular, due to the presence of small structures or particles this approach produces a huge number of false edges. Moreover, in general, the edge approaches based on filters do not yield to a closed contour. As a result, these techniques either fail or require some post-processing step to remove invalid object boundaries in the segmentation results or to close the extracted contour. To address these difficulties, deformable models or snakes [KWT88] have been extensively studied and widely used in medical image segmentation, with promising results, as shown in Fig. 3.6. Deformable models are curves or surfaces defined to match a contour as an energy minimization problem, where the optimal solution constitutes an equilibrium of internal and external energy. The deformable model can move under the influence of internal forces, which are defined within the curve or surface itself to keep the model smooth during deformation, while external forces, which are computed from the image data, are defined to move the model toward an object boundary or other desired features within an image. By constraining extracted boundaries to be smooth and incorporating other prior information about the object shape, deformable models offer robustness to both image noise and boundary gaps.

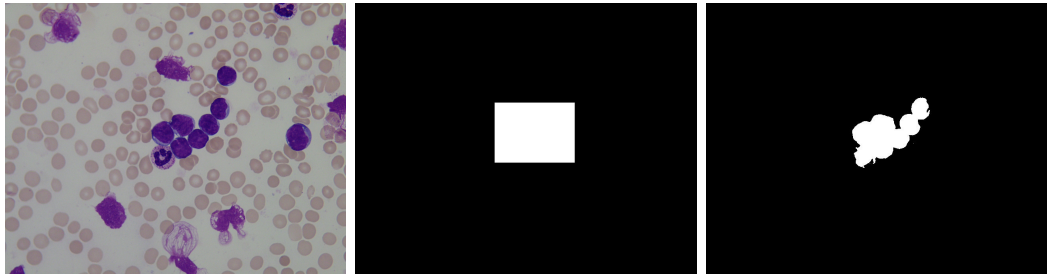


Figure 3.6: Example of deformable model segmentation, by using Active Contour strategy. From left to right: RGB original image; seed region indicates the region to analyse; segmentation result after 250 iterations of Active Contour.

3.3 Region Based

These segmentation techniques introduce more information than previous concerning the connectivity of the pixels forming the entire object, avoiding in this way that individual points of the same region, having the right color or the right contrast, are classified as separate objects. Unlike the pixel and edge-based segmentation methods, region-based approaches aim to identify objects and regions, working directly on the space occupied by the pixels instead of identifying objects from their properties, such as brightness or edges. Considering R as the entire spatial region occupied by the image, the segmentation process can be seen as the partitioning of R into n sub-regions R_1, R_2, \dots, R_n , with the constraint that, the union of all

regions returns R and the intersection between any set of regions is equal to 0. The pixels belonging to a region must be connected (8 or 4 connected), and a similarity criterion must relate them. The most common techniques of segmentation region based are divided into region growing and split and merge techniques.

3.3.1 Region Growing

The region growing is a procedure that allows selecting regions connected and homogeneous of an image, whose selection is effected from a single pixel and is based on a similarity or growth criterion which imposes a maximum difference, a priori defined, between the value of the initial pixel and the pixel values of the region. The basic approach involves the selection of a set of starting pixels, called seed points, and from these seeds add the pixels of their neighborhood that have specific properties of similarity with the seeds, such a specific intensity range or color. The selection of the set of starting pixels is based on the nature of the problem, instead the selection criteria of similarity depends both on the problem and the type of the input image, since it must be ensured independence between the result of the segmentation and the scan direction of the image or the selected seed points.

Algorithms of region growing have been widely used for the analysis of peripheral blood images, in particular for segmentation of cells in which the nucleus is easily identifiable and thus can be used as a seed, as shown in Fig. 3.7.

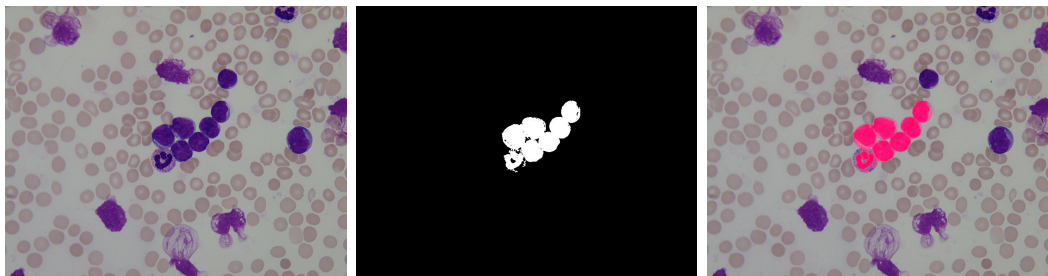


Figure 3.7: Example of region growing application. From left to right: RGB original image; segmentation result after region growing application starting from a WBC nuclei seed point in the centre of image; superimposition of segmentation result over original image indicating the obtained region.

3.3.2 Split and Merge

Segmentation can also be performed by recursively splitting (partitioning) an image until uniform regions are obtained. Then, merging (aggregation) can be performed on adjacent regions that may be compatible on the basis of a similarity criterion. In the simplest way, an image can be partitioned recursively repeating a division into four quadrants, until uniform smaller regions (even composed of a few pixels)

have been obtained, according to the defined similarity criterion. Such division into quadrants is represented by a tree called quad-tree, in which the root node contains the information of the whole image and each of the four children nodes contains the information about a quadrant. If a quadrant is sufficiently uniform, it will not be further partitioned. Splitting step inevitably partitions also homogeneous regions and makes necessary a subsequent phase to merge the adjacent and homogeneous regions of the image into a region that meets the defined criterion of similarity, as shown in Fig. 3.8.

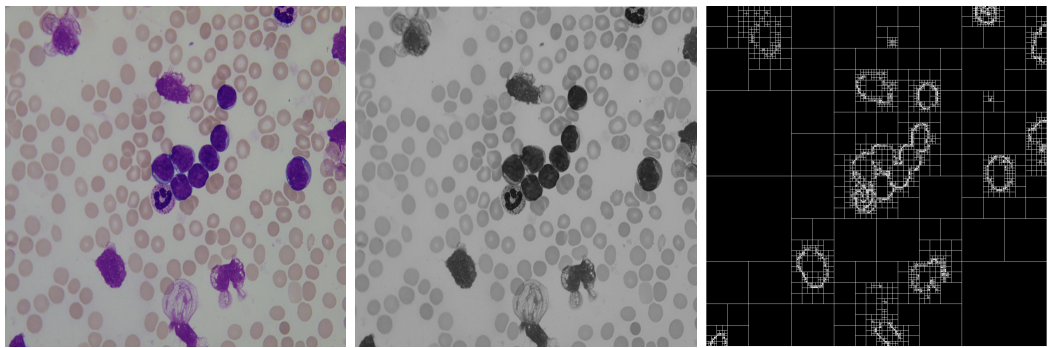


Figure 3.8: Example of split and merge application. From left to right: RGB original image; gray level converted image; split and merge segmentation results by using quadrants from 512×512 down to 1×1 .

3.3.3 Watershed

The watershed segmentation [Mey94] is a mixed approach based on the pixel aggregation (flooding) with the use of the image gradient as a barrier for flooding. In this approach, the gradient image can be considered as a topographical 3D image, in which it is possible to identify points that come from a regional minimum, points that surely fall in a local minimum called basin and points of local maximum called watershed lines. The flooding applied to this image leads to a state where only the watershed lines are visible, that correspond to the objects contours in the image. A direct application of the watershed algorithm induces an over-segmentation due to the presence of too many basins which can never merge, or the presence of noise and other irregularities of the gradient. To avoid this problem in digital microscopy images analysis, the watershed is often used with different strategies that include the use of markers. These markers can be extracted directly from the original images intensity value and subsequently combined with the gradient to obtain a stronger result.

3.4 Post-Processing

After segmentation, an image can be represented as a map of binary objects, background, and foreground. In some cases, the initial segmentation is not satisfactory, as it can present holes or artifacts. Some improvements to the segmentation results can be made directly on the binary image using a series of operations based on a priori knowledge. The morphological operators are commonly used for this purpose, to reduce the number of artifacts, to fill the holes present in some regions, to remove some objects not completely enclosed in the image or others that are not interesting for the analysis. Mathematical morphology is based on the set theory for binary images [Ser83a, Ser83b] and on lattice theory for grey level images. It provides some approaches to image processing that are useful to extract image components and for the representation and description of the object's shape. The sets, in this case, represent the objects contained in the image. The operations of mathematical morphology are based on the use of structuring elements, that are small sets of sub-images used to investigate and study the properties of interest in the input image. They can have any shape defined according to the problem to be treated and are represented as binary matrices.

3.4.1 Mathematical morphology

Mathematical morphology (MM) can be defined as a theory for the analysis of spatial structures. It is called morphology because it aims at analyzing the shape and form of objects. It is mathematical in the sense that the analysis is based on set theory, integral geometry, and lattice algebra. MM is not only a theory but also a very powerful image analysis technique [Soi04]. It was introduced by Matheron in 1964 as a technique for analyzing the geometric structure of metallic and geologic samples. It refers to a branch of nonlinear image processing and analysis that concentrates on the geometric structure within an image. The morphological filters, which can be constructed on the basis of the underlying morphological operations, are more suitable for shape analysis than the standard linear filters since the latter sometimes distort the underlying geometric form of the image. Some of the salient points regarding the morphological approach are as follows [GD88]:

- Morphological operations provide for the systematic alteration of the geometric content of an image while maintaining the stability of the important geometric characteristics.
- There exists a well-developed morphological algebra that can be employed for representation and optimization.
- It is possible to express digital algorithms concerning a tiny class of primitive morphological operations.

- There exist rigorous representation theorems by means of which one can obtain the expression of morphological filters in terms of the primitive morphological operations.

MM was initially developed for binary images and later on generalized to grayscale images [Soi04, Ser84], considered as a sampled function of \mathbb{R}^2 in \mathbb{R} , or in general of any function of \mathbb{R}^n in \mathbb{R} . More recently, several researchers have extended morphological operators to color (or in general multispectral) images, considered as sampled functions of \mathbb{R}^n in \mathbb{R}^m , with m being equal to three in the case of the usual color images or the number of bands otherwise [BDVD12]. Moreover, several approaches for fuzzifying MM have been proposed, extending the ordinary morphological operations by using fuzzy sets [NK00].

Dilation and erosion are the basic morphological processing operations. They are defined in terms of more elementary set operations but are employed as the essential elements of many algorithms. Both dilation and erosion are produced by the interaction of a set called structuring element (SE) with a set of pixels of interest in the image. The structuring element has both a shape and an origin. From these two basic operators, others have been derived (opening, closing, hit-or-miss). They can be applied to extract image components useful in the representation and descriptions of region shapes, such as area granulometry, boundaries, skeleton, or convex hull. Besides, morphological operators can be used for image preprocessing and postprocessing, such as morphological filtering, thinning, and especially for segmentation.

Given an image or set A and a structuring element B , the operations are realized by sliding B over A so that the origin of B visit all elements of A . The *erosion* operation creates a new set by considering all the location of B for which B is entirely contained in A . The result is that the contour of the set A has been eroded. Such a property for which B must be fully contained in A is equivalent to the property for which B must not share any elements with the complement of A . The erosion and dilation are dual operations; thus it is possible to obtain the dilation of A through the use of a structuring element B eroding the complement of A . More immediately, the *dilation* operation creates a new set by considering all the location of B for which at most one element of B is contained in A . The result is that the contour of the set A has been dilated. A simple operation that arises from the erosion is the *boundary extraction*. The contour of a set A can be obtained from the difference between the original set A and the erosion of A with an appropriate structuring element B .

Also, the opening and closing arise from the composition of erosion and dilation. The *opening* of an image or set A with a structuring element B is defined as the erosion of A with B followed by a dilation of the result. This is useful to flatten the contours of an object, breaking the thin lines and removing the sharp contour. The *closing* of an image or set A with structuring element B is defined as the dilation of A with B followed by the erosion of the result. Even the closing flattens the

contours, but differently, in fact, it eliminates small holes and fills the gap in the contours. To fill bigger holes, instead, the operation of *hole filling*, that consists of a more laborious process, is used. Assuming to have a set A with a hole inside, the process starts taking the complement of A , that is composed of the background pixels and therefore also the hole pixels. Then, iteratively, a set containing only a pixel for each hole is dilated using an appropriate structuring element and making every time the intersection with the complement of A , so as to exclude pixels outside the contour of A . Similarly, an iterative procedure of dilatation is used for the *extraction of connected components*. This time the process starts from the points of the connected components in A , that is dilated until the connected components have been filled. The intersection is performed with A at every iteration, to exclude pixels outside the connected component.

Chapter 4

Feature Extraction

Once the image has been segmented into regions, the collection of resulting segmented pixels is represented and described appropriately for further processes. The representation of a region may be based on external characteristics, such as the contour and shape or internal characteristics, such as the color and displacement of the pixels inside the region. The following step results to be the description of the regions according to the chosen representation. In peripheral blood cells images analysis, it may be necessary to use both representations, as it is important to analyze characteristics such as shape and area of a cell and also regional characteristics such as color and texture. The features must be extracted from the object to describe it. The ideal descriptors are those independent to transformation such as the orientation of the object, size, and position and that is sufficiently discriminatory. The purpose of the phase of feature extraction is to obtain a set of descriptors, that will be further separated into different classes by a classification procedure. Features are classified into two distinct groups:

- general features: application independent features such as color, texture, and shape. They can be further divided into features calculated at each pixel, like color and location (*pixel-level features*), features calculated over the results of segmentation or edge detection (*local features*) and features calculated over the entire image or sub-image (*global features*).
- domain-specific features: application dependent features such as human faces, fingerprints and conceptual features.

Moreover, all features can be coarsely classified into low-level features and high-level features. Low-level features can be extracted directly from the original images, whereas high-level feature extraction must be based on low-level features.

4.1 Contour Descriptors

As previously mentioned, many descriptors may be directly extracted from the segmentation result. For example, one of the simplest descriptors is the *contour length*. A good approximation of the contour length can be easily obtained by counting the pixels of the contour. The value of the *diameter* can be easily obtained by computing the maximum distance between two points of the contour. The segment that connects the endpoints of the diameter is called the *major axis*, while the *minor axis* is that segment perpendicular to the major axis, of such a length, that a rectangle completely encloses the contour, passing through the four points of intersection of the axes. The afore defined rectangle is called *bounding box*, having sides parallel to the two axes. The ratio between the sides of the rectangle or the ratio between the two axes measures the value of *eccentricity* (4.1). The *elongation* measures how an object is elongated (4.2), while *rectangularity* represents how rectangular a shape is or, better, how well it fills its minimum bounding box (4.3).

$$\text{eccentricity} = \frac{\sqrt{(\text{majoraxis}^2 - \text{minoraxis}^2)}}{\text{majoraxis}} \quad (4.1)$$

$$\text{elongation} = 1 - \frac{\text{minoraxis}}{\text{majoraxis}} \quad (4.2)$$

$$\text{rectangularity} = \frac{\text{area}}{\text{majoraxis} * \text{minoraxis}} \quad (4.3)$$

These descriptors are useful to discriminate the shape of abnormal objects to normal ones, in particular, peripheral blood cells given their almost circular shape should be distinguished easily from cells with an unusual shape.

4.2 Regional Descriptors

Regional descriptors are the most used since they provide an overall characterization of the examined object. Regional descriptors comprise shape, color and texture descriptors.

4.2.1 Geometric Descriptors

Geometric descriptors are the most used for peripheral blood cells analysis since cells differ considerably in size or shape, thus using these descriptors it is possible to discriminate them easily. The simplest geometrical features are area and perimeter, from which it is possible to compute other more complex descriptors. The *area* of a region is defined as the number of pixels that constitute the region. This descriptor can be useful if the visual geometry is fixed and the objects are always analyzed approximately at the same distance. *convex area* value is also often used. It is the

area of the *convex hull*, the minimum convex polygon that completely encloses the region. The *perimeter* of a region is defined as the number of pixels of its outline. Even in this case, the value of the *convex perimeter* can be used, although it is not usually used as a descriptor, while its most common application is the computation of other descriptors, such as compactness, circularity, and convexity. The *compactness* of a region is defined as the ratio between the area of an object and the area of a circle with the same perimeter (4.4). The circle is used as a benchmark because it is the most compact form its value of compactness is 1. Also the *roundness* calculates the ratio between area and perimeter. However, it excludes the presence of small irregularities. That is the reason why it is derived from the ratio between region area and that of a circle with the same convex perimeter (4.5). The *convexity* instead expresses the relative amount that an object differs from a convex object. This value is obtained through the ratio between the convex perimeter and the perimeter of the object itself (4.6). The value of *solidity*, instead, describes the density of an object by comparing the area of an object and the area of its convex hull (4.7).

$$\text{compactness} = \frac{4 * \pi * \text{area}}{\text{perimeter}^2} \quad (4.4)$$

$$\text{roundness} = \frac{4 * \pi * \text{area}}{\text{convex_perimeter}^2} \quad (4.5)$$

$$\text{convexity} = \frac{\text{perimeter}_{\text{convex}}}{\text{perimeter}} \quad (4.6)$$

$$\text{solidity} = \frac{\text{area}}{\text{convex_area}} \quad (4.7)$$

All the mentioned descriptors that are compactness, circularity, convexity, and solidity, have a maximum value equal to 1, indicating that the region is compact, circular, convex and solid, respectively. The main drawback of the geometric descriptors is that their application requires accurate segmentation of the region of interest and, therefore, they are commonly used with other descriptors less influenced by segmentation errors, such as chromatic descriptors or texture descriptors.

4.2.2 Chromatic Descriptors

Chromatic descriptors delineate the grey level or color distribution of images. These descriptors are calculated directly from histograms of the region, which may be considered as functions of color density. The most used descriptors are the *mean* (4.8), *standard deviation* (4.9), *smoothness* (4.10), *skewness* (4.11), *kurtosis* (4.12), *uniformity* (4.13) and *entropy* (4.14), that describe the shape of the normalised histogram h_N , obtained from the histogram h by dividing each value by the total number of pixels.

$$\mu = \sum_{k=0}^{N_g-1} k \cdot h_N(k) \quad (4.8)$$

$$\sigma = \sqrt{v} \quad (4.9)$$

$$s = \frac{1}{1 + v/(N_g - 1)^2} \quad (4.10)$$

$$\mu_3 = \sigma^{-3} \cdot \sum_{k=0}^{N_g-1} (k - \mu)^3 \cdot h_N(k) \quad (4.11)$$

$$\mu_4 = \sigma^{-4} \cdot \sum_{k=0}^{N_g-1} (k - \mu)^4 \cdot h_N(k) \quad (4.12)$$

$$uni = \sum_{k=0}^{N_g-1} h_N^2(k) \quad (4.13)$$

$$e = - \sum_{k=0}^{N_g-1} h_N(k) \cdot \log_2(h_N(k)) \quad (4.14)$$

where v is the *variance* value (4.15).

$$v = \sum_{k=0}^{N_g-1} (k - \mu)^2 \cdot h_N(k) \quad (4.15)$$

The chromatic descriptors are the most discriminatory characteristics between different types of tissues and cells, but generally, the discrimination on sub-classes requires further descriptors such as texture measures.

4.2.3 Texture Descriptors

The traditional machine vision and image processing approaches assume the presence of uniform intensity values in local regions of the image. This assumption is not always true, and in fact, some objects have a repeated pattern as the main visual feature, which is called texture. Texture probably represents the most used descriptor for the description of the regions of images. Although there are no formal definitions of what is a texture, it can be viewed as a global descriptor generated from the repetition of local patterns. A texture is a repetitive geometric arrangement of the grey levels of an image. It provides important information about the spatial disposition of the grey levels and the relationship with their neighborhoods. The human visual system determines and recognizes easily different types of textures but although for a human observer associating a surface with a texture is very

simple, giving a rigorous definition for this is very complex. Typically, a qualitative definition is used to describe textures. It can be easily guessed that the quantitative analysis of texture passes through statistical and structural relationships among the basic elements of what we call texture. Intuitively, texture descriptors provide measures of properties such as regularity, smoothness, roughness, coarseness, thickness, and so on. In medical image analysis, texture descriptor has proven itself useful to distinguish some abnormal cells or the presence of parasites in the process of evolution. The most used approach for the description of the texture is the statistical approach, that is also the simplest for texture representation. Many statistical descriptors use statistical moments extracted from the histogram of the image or the region. The measures of texture based only on histograms, however, have many drawbacks. In particular statistical moments do not give information about the mutual position of the pixels. Thus, it is important to consider not only the intensity distribution but also the positions of pixels having similar grey levels. Many different methods for managing textures have been developed and are based on the various ways texture can be characterized, including the scale-invariant feature transform (SIFT) [Low04], speeded up robust feature (SURF)[BTG06], the histogram of oriented gradients (HOG) [DT05], Gabor filters [JF90] and others.

Gray Level Co-occurrence Matrix

One of the most powerful model for texture analysis was proposed by Haralick [HSD73]. His method involves the creation of the Gray Level Co-occurrence Matrices (GLCMs) from which features that represent some image aspects can be calculated. A GLCM represents the probability of finding two pixels i and j with distance d and orientation θ and it is denoted with $p_{d,\theta}(i, j)$. Obviously, the d and θ values can assume different values, but the most used are $d = 1$ and $\theta = [0^\circ, 45^\circ, 90^\circ, 135^\circ]$. A GLCM for an image of size $N \times M$ with N_g grey levels is a 2D array of size $N_g \times N_g$. Haralick proposed thirteen descriptors that can be extracted from these matrices. *Angular Second Moment*: is the squares sum of the matrix values (4.16). It is also known as Uniformity. This feature has a range between 0 and 1. The value is 0 if the image is constant.

$$ASM = \sum_{i=0}^{N_g-1} \sum_{j=0}^{N_g-1} p(i, j)^2 \quad (4.16)$$

Often it is called also *Energy* but it is calculated as in (4.17).

$$Ene = \sqrt{\sum_{i=0}^{N_g-1} \sum_{j=0}^{N_g-1} p(i, j)^2} \quad (4.17)$$

Contrast: is the weighted average of all diagonals parallel to the main one which emphasizes the correlation between the different tones (4.18). The contrast is 0 if

the image is constant.

$$Con = \sum_{i=0}^{N_g-1} \sum_{j=0}^{N_g-1} (i - j)^2 \cdot p(i, j) \quad (4.18)$$

Correlation: is the measure of how a pixel is in correlation with its neighbours across the image. It is 1 or -1 for an image related perfectly positively or negatively. It is 0 if the image is constant (4.19).

$$Cor = \sum_{i=0}^{N_g-1} \sum_{j=0}^{N_g-1} \frac{(i - \mu_x) \cdot (j - \mu_y) \cdot p(i, j)}{\sigma_x \cdot \sigma_y} \quad (4.19)$$

Variance: is the measure of linear dependence of the brightness determined from the correlation (4.20).

$$Var = \sum_{i=0}^{N_g-1} \sum_{j=0}^{N_g-1} (i - \mu)^2 \cdot p(i, j) \quad (4.20)$$

Inverse Difference Moment: is a value which measures the proximity of the distribution from GLCM elements to the GLCM diagonal. It has value 1 in the main diagonal of its GLCM (4.21).

$$IDM = \sum_{i=0}^{N_g-1} \sum_{j=0}^{N_g-1} \frac{p(i, j)}{1 + (i - j)^2} \quad (4.21)$$

Often it is called also *Homogeneity* and is calculated as in (4.22).

$$Hom = \sum_{i=0}^{N_g-1} \sum_{j=0}^{N_g-1} \frac{p(i, j)}{1 + |i - j|} \quad (4.22)$$

Sum Average: is the average of the value p_{x+y} containing the sums of all the diagonal orthogonal to the main (4.23).

$$SAve = \sum_{k=0}^{2N_g-2} k \cdot p_{x+y}(k) \quad (4.23)$$

Sum Variance: is an estimation of the second order of the vector p_{x+y} centralized respect to the average (4.24).

$$SVar = \sum_{k=0}^{2N_g-2} (k - F_{SAv})^2 \cdot p_{x+y}(k) \quad (4.24)$$

Sum Entropy: provides an estimate of the vector p_{x+y} relative to entropy, which is the measure of the disorder of the vector itself (4.25).

$$SEnt = - \sum_{k=0}^{2N_g-2} p_{x+y}(k) \cdot \log_2(p_{x+y}(k)) \quad (4.25)$$

Entropy: is the entropy measure for the entire matrix (4.26).

$$Ent = - \sum_{i=0}^{N_g-1} \sum_{j=0}^{N_g-1} p(i,j) \cdot \log_2(p(i,j)) \quad (4.26)$$

Difference Variance: is the variance of the vector p_{x-y} (4.27).

$$DVar = \sum_{k=0}^{N_g-1} (k - F_{DAv})^2 \cdot p_{x-y}(k) \quad (4.27)$$

where DAve, *Difference Average* or *Dissimilarity*, is the average of the vector p_{x-y} containing the differences of all the diagonal orthogonal to the main (4.45).

Difference Entropy: is the entropy measure of the vector p_{x-y} (4.28).

$$DEnt = - \sum_{k=0}^{N_g-1} p_{x-y}(k) \cdot \log_2(p_{x-y}(k)) \quad (4.28)$$

Measure of correlation 1 and 2: are measures related to entropy of the matrix (4.29), (4.30).

$$MC1 = \frac{F_{Ent} - HXY1}{\max(Hx - Hy)} \quad (4.29)$$

$$MC2 = \sqrt{1 - \exp[-2(HXY2 - F_{Ent})]} \quad (4.30)$$

where

$$p_x(i) = \sum_{j=0}^{N_g-1} p(i,j) \quad (4.31)$$

$$p_y(j) = \sum_{i=0}^{N_g-1} p(i,j) \quad (4.32)$$

$$p_{x-y}(i-j) = \sum_{i=0}^{N_g-1} \sum_{j=0}^{N_g-1} p(i,j) \quad (4.33)$$

$$p_{x+y}(i+j) = \sum_{i=0}^{N_g-1} \sum_{j=0}^{N_g-1} p(i,j) \quad (4.34)$$

$$\mu_x = \sum_{i=0}^{N_g-1} i \cdot p_x(i) \quad (4.35)$$

$$\mu_y = \sum_{j=0}^{N_g-1} j \cdot p_y(j) \quad (4.36)$$

$$\mu = (\mu_x + \mu_y)/2 \quad (4.37)$$

$$\sigma_x = \sqrt{\sum_{i=0}^{N_g-1} p_x(i) \cdot (i - \mu_x)^2} \quad (4.38)$$

$$\sigma_y = \sqrt{\sum_{j=0}^{N_g-1} p_y(j) \cdot (j - \mu_y)^2} \quad (4.39)$$

$$HX = - \sum_{i=0}^{N_g-1} p_x(i) \cdot \log_2(p_x(i)) \quad (4.40)$$

$$HY = - \sum_{j=0}^{N_g-1} p_y(j) \cdot \log_2(p_y(j)) \quad (4.41)$$

$$HXY1 = - \sum_{i=0}^{N_g-1} \sum_{j=0}^{N_g-1} p(i, j) \cdot \log_2(p_x(i) \cdot p_y(j)) \quad (4.42)$$

$$HXY2 = - \sum_{i=0}^{N_g-1} \sum_{j=0}^{N_g-1} p_x(i) \cdot p_y(j) \cdot \log_2(p_x(i) \cdot p_y(j)) \quad (4.43)$$

To these descriptors extracted from GLCMs many others have been proposed, but only seven are widely used [ST99, Cla02], that are *mean* (4.44), *difference average* (4.45), *autocorrelation* (4.46), *maximum probability* (4.47), *cluster shade* (4.48), *cluster prominence* (4.49) and *product moment* (4.50).

$$\mu = \sum_{i=0}^{N_g-1} \sum_{j=0}^{N_g-1} i \cdot p(i, j) \quad (4.44)$$

$$DAve = \sum_{i=0}^{N_g-1} \sum_{j=0}^{N_g-1} |i - j| \cdot p(i, j) = \sum_{k=0}^{N_g-1} k \cdot p_{x-y}(k) \quad (4.45)$$

$$Aut = \sum_{i=0}^{N_g-1} \sum_{j=0}^{N_g-1} i \cdot j \cdot p(i, j) \quad (4.46)$$

$$MP = \max(p(i, j)) \quad (4.47)$$

$$CS = \sum_{i=0}^{N_g-1} \sum_{j=0}^{N_g-1} (i + j - \mu_x - \mu_y)^3 \cdot p(i, j) \quad (4.48)$$

$$CP = \sum_{i=0}^{N_g-1} \sum_{j=0}^{N_g-1} (i + j - \mu_x - \mu_y)^4 \cdot p(i, j) \quad (4.49)$$

$$PM = \sum_{i=0}^{N_g-1} \sum_{j=0}^{N_g-1} (i - \mu_x) \cdot (j - \mu_y) \cdot p(i, j) \quad (4.50)$$

Some interesting methods have also been presented to extend the original implementation of GLCM, computing the matrices by evaluating different distance parameters [GVB07], different windows sizes [HCx09], different color channels [BH07], adding the color gradient [GW12] or also considering the edge orientation [MMN⁺12]. Furthermore, the GLCM descriptors can be extracted after computing a weighted sum of GLCM elements [WJL03] or after calculating the local gradient of the matrix [CWCT09].

Gray Level Difference Matrix

Another useful tool for texture analysis is the grey level difference matrix (GLDM)[CH80], that is a particular type of matrix originated by the absolute differences between grey levels pairs. Actually, the GLDM is defined in very similar way to the GLCM, using the same notions of distance and orientation to find grey levels pairs. The main difference arises in the construction and dimension of the matrix. In fact, the GLDM preserves the size of the original image (and not $N_g \times N_g$), collecting the absolute difference between pairs of pixel values (and not the occurrences of two grey levels). This matrix is used to calculate the histogram $h(d)$ that denotes the number of differences with value d . The histogram is then normalized $h_N(d) = h(d)/N$ with $N = \sum_d h(d)$ in order to easily compute nine descriptors that are *mean* (4.51), *angular second moment* (4.52), *contrast* (4.53), *variance* (4.54), *inverse difference moment* (4.55), *entropy* (4.56), *product moment* (4.57), *cluster shade* (4.58) and *cluster prominence* (4.59).

Mean:

$$\mu = \sum_{d=0}^{N_g-1} d \cdot h_N(d) \quad (4.51)$$

Angular Second Moment:

$$ASM = \sum_{d=0}^{N_g-1} h_N(d)^2 \quad (4.52)$$

Contrast:

$$Con = \sum_{d=0}^{N_g-1} d^2 \cdot h_N(d) \quad (4.53)$$

Variance:

$$Var = \sum_{d=0}^{N_g-1} (d - \mu)^2 \cdot h_N(d) \quad (4.54)$$

Inverse Difference Moment:

$$IDM = \sum_{d=0}^{N_g-1} \frac{h_N(d)}{1 + d^2} \quad (4.55)$$

Entropy:

$$Ent = \sum_{d=0}^{N_g-1} h_N(d) \cdot \log_2(h_N(d)) \quad (4.56)$$

Product Moment:

$$PM = \sum_{d=0}^{N_g-1} (d - \mu) \cdot h_N(d) \quad (4.57)$$

Cluster Shade:

$$CS = \sum_{d=0}^{N_g-1} (d - \mu)^3 \cdot h_N(d) \quad (4.58)$$

Cluster Prominence:

$$CP = \sum_{d=0}^{N_g-1} (d - \mu)^4 \cdot h_N(d) \quad (4.59)$$

Gray Level Run-Length Matrix

A different tool for texture analysis is based on information of higher order statistics that uses the Grey Level Run-Length Matrices (GLRLM) [Tan98]. In this approach the GLRLM contains information on a particular number of equal grey levels (run) in a given direction. So, a run-length matrix is defined as a set of consecutive pixels having the same grey level. The element (i, j) of a run-length matrix specifies the number of times that the image contains a run of length j composed by all pixels with grey level i . The creation of the run-length matrices is very simple and the number of operations to be done is directly proportional to the number of image points. A coarse texture will be characterized by a long run, while a finer texture will be characterized by a shorter run. Also, the GLRLMs are calculated by considering the main four orientations and for each matrix eleven descriptors can be extracted, that are *short run emphasis* (4.60), *long run emphasis* (4.61), *grey level non-uniformity* (4.62), *run length non-uniformity* (4.63), *run percentage* (4.64), *low*

grey level run emphasis (4.65), *high grey level run emphasis* (4.66), *short run low grey level emphasis* (4.67), *short run high grey level emphasis* (4.68), *long run low grey level emphasis* (4.69) and *long run high grey level emphasis* (4.70).

Short Run Emphasis:

$$SRE = \frac{1}{n_r} \sum_{i=1}^M \sum_{j=1}^N \frac{p(i,j)}{j^2} = \frac{1}{n_r} \sum_{j=1}^N p_r(j) \cdot j^2 \quad (4.60)$$

Long Run Emphasis:

$$LRE = \frac{1}{n_r} \sum_{i=1}^M \sum_{j=1}^N p(i,j) \cdot j^2 = \frac{1}{n_r} \sum_{j=1}^N p_r(j) \cdot j^2 \quad (4.61)$$

Grey Level Non-uniformity

$$GLN = \frac{1}{n_r} \sum_{i=1}^M \left(\sum_{j=1}^N p(i,j) \right)^2 = \frac{1}{n_r} \sum_{i=1}^M p_g(i)^2 \quad (4.62)$$

Run Length Non-uniformity

$$RLN = \frac{1}{n_r} \sum_{j=1}^N \left(\sum_{i=1}^M p(i,j) \right)^2 = \frac{1}{n_r} \sum_{j=1}^N p_r(j)^2 \quad (4.63)$$

Run Percentage

$$RP = \frac{n_r}{n_p} \quad (4.64)$$

Low Grey Level Run Emphasis

$$LGLRE = \frac{1}{n_r} \sum_{i=1}^M \sum_{j=1}^N \frac{p(i,j)}{i^2} = \frac{1}{n_r} \sum_{i=1}^M \frac{p_g(i)}{i^2} \quad (4.65)$$

High Grey Level Run Emphasis

$$HGLRE = \frac{1}{n_r} \sum_{i=1}^M \sum_{j=1}^N p(i,j) \cdot i^2 = \frac{1}{n_r} \sum_{i=1}^M p_g(i) \cdot i^2 \quad (4.66)$$

Short Run Low Grey Level Emphasis

$$SRLGLE = \frac{1}{n_r} \sum_{i=1}^M \sum_{j=1}^N \frac{p(i,j)}{i^2 \cdot j^2} \quad (4.67)$$

Short Run High Grey Level Emphasis

$$SRHGLE = \frac{1}{n_r} \sum_{i=1}^M \sum_{j=1}^N \frac{p(i,j) \cdot i^2}{j^2} \quad (4.68)$$

Long Run Low Grey Level Emphasis

$$LRLGLE = \frac{1}{n_r} \sum_{i=1}^M \sum_{j=1}^N \frac{p(i,j) \cdot j^2}{i^2} \quad (4.69)$$

Long Run High Grey Level Emphasis.

$$LRHGLE = \frac{1}{n_r} \sum_{i=1}^M \sum_{j=1}^N p(i,j) \cdot i^2 \cdot j^2 \quad (4.70)$$

Local Binary Pattern

Another useful tool for texture analysis is the Local Binary Pattern (LBP), originally proposed in [OPH96] and widely used for grey level texture classification, due to its simplicity and robustness. This operator transforms the image by thresholding the neighborhood of each pixel and by coding the result as a binary number. The resulting image histogram can be used as a feature vector for texture classification. Also, for the LBP operator two main parameters must be defined, which are the radius r and the number of neighborhood n pixels. For example, some possible versions of this operator are the $LBP_{8,1}$ implemented with the parameters r and n equal to 1 and 8, respectively, and the $LBP_{16,2}$ implemented with the parameters r and n equal to 2 and 16, respectively. These two LBP operators are reported in Fig.4.1.

4.3 Feature Selection

A further step, not always present on a CAD system, is the feature selection, a process commonly used in pattern recognition that allows determining the most relevant features reducing the size of the vectors associated with the objects. The feature selection aims to reduce the dimensionality eliminating both the redundant features, that represent information derived from other, both the features that are irrelevant for the analysis. The "ideal" approach would be to test all the possible subsets of features, using them as input to the classification algorithm of interest and select the subset that allows obtaining the best results. This approach in most cases is not applicable. There are several techniques for the selection of characteristics, that can be grouped into three categories:

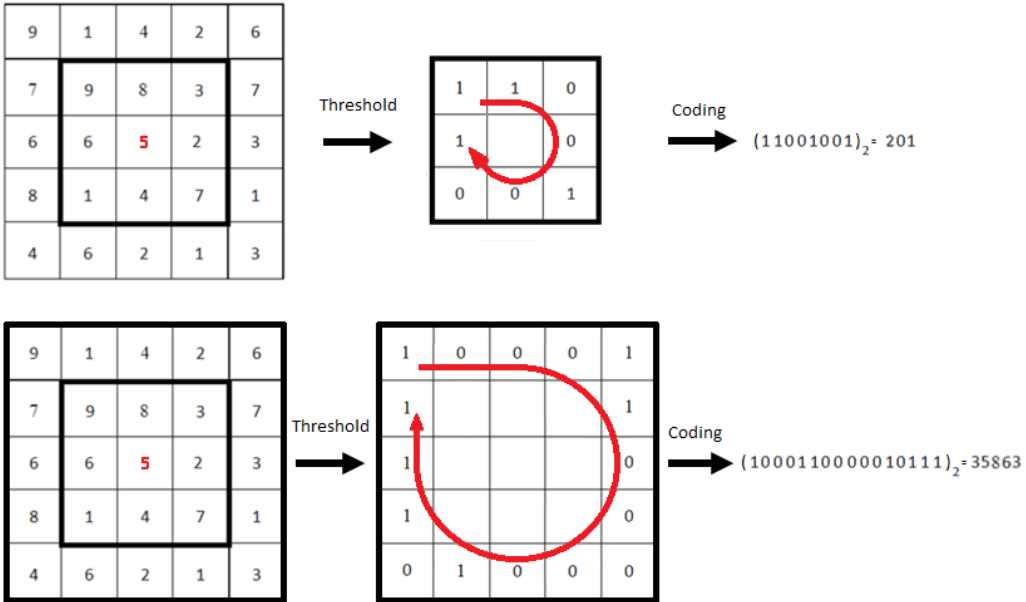


Figure 4.1: The LBP operators $LBP_{8,1}$ and $LBP_{16,2}$, respectively

- embedded methods: the selection is internal to the classification algorithm that takes advantage of internal knowledge of the classifier, such as the weight used to induce the model [DH73]
- filter methods: also known as scheme-independent selection, because the selection is made in advance, with a method independent from the classification algorithm that will be applied subsequently using some measure of distance or correlation [YL04]
- wrapper methods: also known as scheme-specific selection, because the selection is performed making a comparison between different subsets of features, investigated with approaches of sequential forward or backward selection [Kit78], according to the classification algorithm that will be applied later.

Generally, the wrapper methods perform better than the other methods, as they are optimized for a specific classifier, but they are computationally eligible only for small feature vectors. On the other hand, there are different approaches called, by many authors, "feature selection" that do not perform a proper features selection, but rather a dimensionality reduction through projection or combination. The Principal Component Analysis (PCA) [WEG87] is the most popular technique for the reduction of dimensionality. Its purpose is to find a set of orthogonal vectors in the feature space corresponding to the directions along which the data have the highest variance. Projecting the data from their original space to the orthogonal complement permits the dimensionality reduction of the features. The advantages of the PCA is that it can deal with large datasets both in objects and variables reducing the

redundancy. Moreover, it does not make particular assumptions on the data, and so it can be applied to all datasets. The most significant disadvantage arises from the fact that PCA does not select the features, but it creates new ones combining the original. This procedure dramatically affects the control over the single feature, that is particularly important in image processing where features are extracted directly from the image and thus it is essential to establish which are determinant for the task of classification, in order to avoid the extraction of insignificant features.

Chapter 5

Classification

Once the features have been extracted from cells, they must be inserted in a process that classifies cells based on medical concepts. Given a collection of records, each one composed by a set of features x and by a label of class y , the goal is to define a function or classification model, that associates a class label y to each set of attributes x . A classification model is a tool to describe and classify the data of a specific domain. It is possible thanks to a training set, namely a set of training samples in which the values of the class labels are well known. So, the relations between attributes and class labels can be identified and encoded in a model, through a learning algorithm. This model must be able not only to describe the training set but also to predict the class of new records not yet labeled correctly. Literature comprises several classification algorithms, but the most used on medical images are following listed:

- Nearest Neighbour
- Decision Trees
- Bayesian Classifier
- Neural Network
- Support Vector Machine

Moreover, machine learning methods are generally divided into *supervised* and *unsupervised learning* algorithms, although there are many nuances. In supervised learning, a model is presented with a dataset $\mathcal{D} = \{\mathbf{x}, y\}_{n=1}^N$ of input features \mathbf{x} and label y pairs, where y typically represents an instance of a fixed set of classes. In the case of regression tasks y can also be a vector with continuous values. Supervised training typically amounts to finding model parameters Θ that best predict the data based on a loss function $L(y, \hat{y})$. Here \hat{y} denotes the output of the model obtained by feeding a data point \mathbf{x} to the function $f(\mathbf{x}; \Theta)$ that represents the model. Unsupervised learning algorithms process data without labels and are trained to find

patterns, such as latent subspaces. Examples of traditional unsupervised learning algorithms are principal component analysis and clustering methods. Unsupervised training can be performed under many different loss functions. One example is reconstruction loss $L(\mathbf{x}, \hat{\mathbf{x}})$ where the model has to learn to reconstruct its input, often through a lower-dimensional or noisy representation.

5.1 Nearest Neighbor

The Nearest Neighbour classifier uses the concept of proximity to classify a new record, based on the samples provided by the training set that are similar to it. Each instance of the training set is a point in an n -dimensional space, where n is the number of features. When NN has to classify a new record, it calculates its distance from each training set sample. Then, the k examples of the training set closer to the new record, called k-Nearest Neighbors (kNN) [CH67], are identified and used to assign the class label prevailing among kNN to the new record. However, there may be problems in the choice of k , in fact, if this value is too small, there is a high sensitivity to noise, but if it is too large, there may be examples not similar enough to the record to be classified, among the kNN. One way to reduce the influence of the parameter k is to calculate the prevailing class by assigning a different weight to each of the first neighbors according to its distance from the record to be classified. This type of classifier is the simplest among those listed, as it does not require the induction of a model from the training set, which is used in the classification step to compare the new records with the known ones. In contrast to the saved resources for the construction of the model, the classification of a new record, however, is rather expensive. Indeed, the proximity between the new record and the known examples of the training set must be calculated every time.

5.2 Decision Trees

Decision Trees [Qui86] are decision support tools that use a tree-like graph or decision model for classification. The goal is to create a model that predicts the value of a target variable by learning simple decision rules inferred from the data features. Thus, during the classification of a new record, the decision tree represents a flowchart-like structure in which each internal node represents a test on an attribute, and each branch represents the outcome of the test. Obviously, each leaf node represents a class label, and the decision is taken after computing all attributes. The paths from the root to the leaf nodes represent the classification rules. The greatest advantage of decision trees is that they are simple to understand and interpret, but they can be complex with a high number of attributes. In particular, having more attributes conducts to a deeper tree and, therefore, the decision rules become more complex and the model fitter. Among disadvantages, there is that decision tree can

create too complex trees that do not produce a suitable generalization of the data, generating overfitting, even though the greatest one is that the same classification rules can be expressed with different decision trees. Thus finding the optimal decision tree is known to be an NP-complete problem under several aspects of optimality and even for simple concepts. This problem is generally mitigated by training multiple trees in an ensemble learner, where the features and samples are randomly sampled with a replacement strategy.

5.3 Bayesian Classifier

The Bayesian classifiers are based on probabilistic relations between the class labels and feature values of the record. Considering the features of a record as random variables a Bayesian network can be used to plot the conditional dependencies among a set of random variables. It is an acyclic and directed graph in which the nodes represent random variables, and the arcs represent dependency relationships between the variables. Each node of the network is associated with a probability table containing the a priori probability if that node does not depend on any other node, or the conditional probability if the node depends on a set of other nodes. Thus, given a training sample, it must be found the Bayesian network that best describes the conditional dependencies between variables. Once defined the network, the process of classification of a new record entails the calculation of the posterior probability for each class and the selection of the class for which the probability is the highest. The induction of the network that best describes a given training set involves the definition of network structure and the estimation of probabilities values table associated with each node of the network. In a general case, this is an intractable problem, but some algorithms induce Bayesian classification models introducing appropriate simplifying assumptions on the network topology. The simplest among the Bayesian classifiers is the so-called Naive Bayes [DH73], [LIT92] and is based on the assumption that the features are conditionally independent, given the value of the class. In this way the a priori probability of the class and the conditional probabilities of the class features can be easily estimated from the training sample. With the Naive Bayes method, the model is not significantly influenced by either the noise, which is mediated through the calculation of probabilities or by any unnecessary features, for which the probabilities are distributed in an almost uniform way. Despite its simplicity, the Bayesian classifier can perform accurate classifications but only if the features are discriminatory.

5.4 Artificial Neural Network

Artificial Neural Networks (ANN) classifiers are the most used in medical applications. They are networks that emulate the behavior of the human brain, composed

of a set of nodes that are interconnected by links to which a weight is associated. In ANNs, as in biological systems, learning corresponds to change the weight values of the connections between nodes. Given a training sample, the weights of the model are first initialized randomly and then iteratively adjusted, so that the output of the model appears consistent with the values of the label class. The simplest ANNs are composed of two levels, the input level, and the output level. The input layer contains a node for each numerical features, while the categorical features require more nodes, for example, a feature with n possible values can be transformed into n binary variables. The output layer, on the other hand, can contain only one node, if the problem of classification is binary and k nodes if the class label can assume k values. There are also multilevel ANNs whose structures present additional hidden layers between the input layer and the output layer. The number of hidden layers is often determined by trial and error, in fact, typically the correct number of hidden layers is found starting from a network with a high number of layers and nodes, and it progressively decreases the model complexity. Network training involves the adjustment of the weights with the aim to minimize the internal error. This process is costly, especially if the network topology is complex, even if the classification process is rapid. The model is susceptible to noise because the weights are adjusted for each instance of the training sample. On the contrary, the irrelevant or redundant features do not significantly affect the model, since the corresponding weights are typically tiny.

5.5 Support Vector Machine

Support Vector Machines (SVM) are supervised learning models with associated learning algorithms that analyze data used for classification and regression analysis. They have been designed for binary classification problems, so with only two classes, but it can also be extended to multi-class problems. The SVM binary classification is based on the mapping of input vectors in a high dimensionality features space, induced by a kernel function. The learning algorithm produces an optimal hyperplane of separation between the two classes. The SVM can perform linear and nonlinear discrimination, according to the kernel function. It is possible to find a kernel function for which the parameters of the model can be induced without an explicit mapping data. The induction of the model in this way is formulated as an optimization problem, in which it is possible to find quite efficiently a global minimum for the objective function. The SVM provides extreme flexibility both because it is possible to make use of different types of kernels and because it is possible to define a hyperplane for separating classes which guarantees a certain tolerance with respect to noise, using a soft margin instead of a hard margin. For an optimization problem, it becomes changing the constraint value with the c value, that can be increased to obtain less training error. Kernel methods use other parameters for the creation of the separating hyperplane. The Gaussian Radial Basis Function (RBF)

is one of the most used kernels performing a non-linear separation defined by the radius γ of the RBF. Other kernels are the quadratic kernel, the polynomial kernel that can be defined with different order p and the Multilayer Perceptron kernel (MLP) that instead can be defined for different slope α and the intercept constant β . The multi-class problem is solved by building many different binary classifiers and then combine them. The most used strategies are the combinations one-vs-one and one-vs-all.

5.5.1 One-vs-all SVM

The one-vs-all approach, also known as one-vs-rest, is the first and the most intuitive approach to extend the SVM to multi-class problems. The basic idea of the one-vs-all approach is straightforward. In fact, for a multi-class problem having m classes, it consists on training m different binary SVM classifiers where each one of them separates one class from all the other $m - 1$ classes. Then, in the testing phase the class label is assigned taking into account the decision of every m classifiers. The most common practice is to assign the class label i , where i is the classifier that maximizes the separation between the class i from the rest. Another common practice is to use binary trees to arrange the $m - 1$ binary SVM; the path from the root node to a leaf determines the class label. In the best scenario, only one comparison is needed, while in the worst case $m - 1$ comparisons are needed. The problem encountered with binary tree SVM is that there are $\prod_{i=3}^m 2i - 3$ possible ways to construct a tree for a multi-class problem. Thus, for a multi-class problem with a huge value of m , analyzing all the possible solutions is impossible.

5.5.2 One-vs-one SVM

The one-vs-one approach is another commonly used SVM strategy but, differently from the one-vs-all approach, for a multi-class problem having m classes, it consists on training $\frac{m(m-1)}{2}$ different binary SVM classifiers, where each one of them separates a class from another one. In this case, combining the results from individual binary SVM classifiers becomes more complex. The simplest way to obtain the predicted class label is to use the majority voting, counting the votes given by each binary classifier and assigning the class label that has the highest number of votes. However, the voting process could produce ambiguous results (e.g., tie cases). For this reason, a common practice is to use the majority voting strategy combined with the maximum separation strategy, assigning the class label i , if the result of the binary classifier produces the highest number of i votes with the maximum separation between i class and each of the other classes. Another common practice consists in arranging all the $\frac{m(m-1)}{2}$ binary SVM classifiers in a Directed Acyclic Graph (DAG) structure with the same number of nodes. The test phase starts at the root node and continues until a leaf node, representing the predicted class label, is reached. Thus, only $m - 1$ comparisons are needed, completely avoiding tie cases,

but the problem is encountered just during the construction of the DAG. , in this case, there are several ways to construct the DAG structure, and each one of them may produce different classification results and when the number of classes is high, testing all possible orders is impossible.

5.6 Deep learning methods

5.6.1 Neural Networks

Neural networks are a type of learning algorithm which forms the basis of most deep learning methods. A neural network comprises of neurons or units with some activation a and parameters $\Theta = \{\mathcal{W}, \mathcal{B}\}$, where \mathcal{W} is a set of weights and \mathcal{B} a set of biases. The activation represents a linear combination of the input \mathbf{x} to the neuron and the parameters, followed by an element-wise non-linearity $\sigma(\cdot)$, referred to as a transfer function:

$$a = \sigma(\mathbf{w}^T \mathbf{x} + b). \quad (5.1)$$

Typical transfer functions for traditional neural networks are the sigmoid and hyperbolic tangent function. The multi-layered perceptrons (MLP), the most well-known of the traditional neural networks, have several layers of these transformations:

$$f(\mathbf{x}; \Theta) = \sigma(\mathbf{W}^T \sigma(\mathbf{W}^T \dots \sigma(\mathbf{W}^T \mathbf{x} + b)) + b). \quad (5.2)$$

Here, \mathbf{W} is a matrix comprising of columns \mathbf{w}_k , associated with activation k in the output. Layers in between the input and output are often referred to as 'hidden' layers. When a neural network contains multiple hidden layers it is typically considered a 'deep' neural network, hence the term 'deep learning'.

At the final layer of the network the activations are mapped to a distribution over classes $P(y|\mathbf{x}; \Theta)$ through a *softmax* function:

$$P(y|\mathbf{x}; \Theta) = \text{softmax}(\mathbf{x}; \Theta) = \frac{e^{\mathbf{w}_i^T \mathbf{x} + b_i}}{\sum_{k=1}^K e^{\mathbf{w}_k^T \mathbf{x} + b_k}}, \quad (5.3)$$

where \mathbf{w}_i indicates the weight vector leading to the output node associated with class i .

Maximum likelihood with stochastic gradient descent is currently the most popular method to fit parameters Θ to a dataset \mathcal{D} . In stochastic gradient descent a small subset of the data, a mini-batch, is used for each gradient update instead of the full data set. Optimizing maximum likelihood in practice amounts to minimizing the negative log-likelihood:

$$\arg \min_{\Theta} - \sum_{n=1}^N \log [P(y_n|\mathbf{x}_n; \Theta)]. \quad (5.4)$$

This results in the binary cross-entropy loss for two-class problems and the categorical cross-entropy for multi-class tasks. A downside of this approach is that it typically does not optimize the quantity we are interested in directly, such as area under the receiver-operating characteristic (ROC) curve or common evaluation measures for segmentation, such as the Dice coefficient.

Currently, the most popular models are trained end-to-end in a supervised fashion, greatly simplifying the training process. The most popular architectures are convolutional neural networks (CNNs) and recurrent neural networks (RNNs). CNNs are currently most widely used in (medical) image analysis, although RNNs are gaining popularity.

5.6.2 Convolutional Neural Networks (CNNs)

There are two key differences between MLPs and CNNs. First, in CNNs weights in the network are shared in such a way that the network performs convolution operations on images. This way, the model does not need to learn separate detectors for the same object occurring at different positions in an image, making the network equivariant with respect to translations of the input. It also drastically reduces the amount of parameters (i.e. the number of weights no longer depends on the size of the input image) that need to be learned.

At each layer, the input image is convolved with a set of K kernels $\mathcal{W} = \{\mathbf{W}_1, \mathbf{W}_2, \dots, \mathbf{W}_K\}$ and added biases $\mathcal{B} = \{b_1, \dots, b_K\}$, each generating a new feature map \mathbf{X}_k . These features are subjected to an element-wise non-linear transform $\sigma(\cdot)$ and the same process is repeated for every convolutional layer l :

$$\mathbf{X}_k^l = \sigma(\mathbf{W}_k^{l-1} * \mathbf{X}^{l-1} + b_k^{l-1}). \quad (5.5)$$

The second key difference between CNNs and MLPs, is the typical incorporation of pooling layers in CNNs, where pixel values of neighborhoods are aggregated using a permutation invariant function, typically the max or mean operation. This induces a certain amount of translation invariance and again reduces the amount of parameters in the network. At the end of the convolutional stream of the network, fully-connected layers (i.e. regular neural network layers) are usually added, where weights are no longer shared. Similar to MLPs, a distribution over classes is generated by feeding the activations in the final layer through a softmax function and the network is trained using maximum likelihood.

5.6.3 Deep CNN Architectures

Given the prevalence of CNNs in medical image analysis, we elaborate on the most common architectures and architectural differences among the widely used models.

General classification architectures

LeNet [LBBH98] and AlexNet [KSH12], introduced over a decade later, were in essence very similar models. Both networks were relatively shallow, consisting of two and five convolutional layers, respectively, and employed kernels with large receptive fields in layers close to the input and smaller kernels closer to the output. AlexNet did incorporate rectified linear units instead of the hyperbolic tangent as activation function.

After 2012 the exploration of novel architectures took off, and in the last three years there is a preference for far deeper models. By stacking smaller kernels, instead of using a single layer of kernels with a large receptive field, a similar function can be represented with less parameters. These deeper architectures generally have a lower memory footprint during inference, which enable their deployment on mobile computing devices such as smartphones. [SZ14] were the first to explore much deeper networks, and employed small, fixed size kernels in each layer. A 19-layer model often referred to as VGG19 or OxfordNet won the ImageNet challenge of 2014.

Since 2014, the performance on the ImageNet benchmark has saturated and it is difficult to assess whether the small increases in performance can really be attributed to 'better' and more sophisticated architectures. The advantage of the lower memory footprint these models provide is typically not as important for medical applications. Consequently, AlexNet or other simple models such as VGG are still popular for medical data, though recent landmark studies all use a version of GoogleNet called Inception v3 [VLMea16]. Whether this is due to a superior architecture or simply because the model is a default choice in popular software packages is again difficult to assess.

5.6.4 Recurrent Neural Networks (RNNs)

Traditionally, RNNs were developed for discrete sequence analysis. They can be seen as a generalization of MLPs because both the input and output can be of varying length, making them suitable for tasks such as machine translation where a sentence of the source and target language are the input and output. In a classification setting, the model learns a distribution over classes $P(y|\mathbf{x}_1, \mathbf{x}_2, \dots, \mathbf{x}_T; \Theta)$ given a sequence $\mathbf{x}_1, \mathbf{x}_2, \dots, \mathbf{x}_T$, rather than a single input vector \mathbf{x} .

The plain RNN maintains a latent or hidden state \mathbf{h} at time t that is the output of a non-linear mapping from its input \mathbf{x}_t and the previous state \mathbf{h}_{t-1} :

$$\mathbf{h}_t = \sigma(\mathbf{W}\mathbf{x}_t + \mathbf{R}\mathbf{h}_{t-1} + \mathbf{b}), \quad (5.6)$$

where weight matrices \mathbf{W} and \mathbf{R} are shared over time. For classification, one or more fully connected layers are typically added followed by a softmax to map the sequence to a posterior over the classes.

$$P(y|\mathbf{x}_1, \mathbf{x}_2, \dots, \mathbf{x}_T; \Theta) = \text{softmax}(\mathbf{h}_T; \mathbf{W}_{out}, \mathbf{b}_{out}). \quad (5.7)$$

Although initially proposed for one-dimensional input, RNNs are increasingly applied to images. In natural images 'pixelRNNs' are used as autoregressive models, generative models that can eventually produce new images similar to samples in the training set.

5.7 Model Evaluation

The performance of the classification models is then evaluated on the basis of percentage of records correctly classified on a test set with a known class label. Therefore, *accuracy* and the *error rate* of the model can be calculated by comparing the known class labels, and the classifiers predicted labels. A binary problem is composed of positive and negative classes and it can be evaluated with the following measures: True Positive (TP) indicates the number of positives records correctly classified as positives, True Negative (TN) measure indicates the number of negatives records correctly classified as negative, False Positive (FP) measure is the number of negative records misclassified as positive and, finally, False Negative (FN) measure is the number of positive records misclassified as negative. In this way, the accuracy of the error rate can be written as in (5.8) and (5.9):

$$\text{accuracy} = \frac{TP + TN}{TP + TN + FP + FN} \quad (5.8)$$

$$\text{errorrate} = \frac{FP + FN}{TP + TN + FP + FN} \quad (5.9)$$

Differently from binary classification ones, if the problem presents an uncommon number of classes the accuracy and the error rate typically are not good measures of model performance. In this case, the most used measures are the *True Positive Rate* (TPR) also called *sensitivity* or *recall* (r) (5.10), the *True Negative Rate* (TNR) also called *specificity* (5.11), the *False Positive Rate* (FPR) (5.12), the *False Negative Rate* (FNR) (5.13) and the *precision* (p) (5.14). Precision and recall are used if the correct classification of positive instances is considered more important or interesting, according to the faced problem. Indeed, a good model should be able to maximise both measures. For this reason, another important metric is frequently used: the *F-measure* or *F-score* (5.15).

$$TPR = r = \frac{TP}{TP + FN} \quad (5.10)$$

$$TNR = \frac{TN}{TN + FP} \quad (5.11)$$

$$FPR = \frac{FP}{TN + FP} \quad (5.12)$$

$$FNR = \frac{FN}{TP + FN} \quad (5.13)$$

$$p = \frac{TP}{TP + FP} \quad (5.14)$$

$$F\text{-score} = \frac{2rp}{r + p} \quad (5.15)$$

It is worth noting that the same measures are also used for segmentation evaluation. Actually, if any manually segmented images or ground-truth are available, a pixel-wise evaluation can be made in order to assess if a pixel has been correctly included in the region which it belongs (TP), it has been correctly excluded from the region (TN), it has been erroneously included in the region (FP) or it has been wrongly excluded from the region (FN).

The performance of a model may not depend only on the type of classification algorithm but also by other factors such as the size or distribution of the classes in the training and test set. In particular, if the dataset has reduced size, the performances are more related to the specific composition of the samples, and a higher variance characterizes them. Some methods are quite useful to extract a representative test set, from the original dataset, able to assess the performance of the model. They are:

- Holdout: a part of the available samples, the training set, is used to train the model while another part, the test set, is used for its evaluation. Holdout involves a reduction of examples available for training and addiction due from specific partition created. To ensure that the training set and the test set are uniformly representative, the partition can be made by using a stratified sampling process.
- Repeated Holdout: the holdout method is iterated k times, in order to avoid control over the number of times that each record is used for training and testing. The accuracy and error rate are calculated averaging the k iteration results.
- Cross-Validation: the examples available are divided into k sub-sets of equal dimension. The process of training and evaluation of the model is repeated k times, each time using $k - 1$ different sub-sets for training and one sub-set for the test. As for Repeated Holdout, the accuracy and error rate are calculated averaging the k iteration results, but in this case, the final results are more stable since the test sets are mutually exclusive and cover the entire initial sample.
- Leave-one-out: a special case of cross-validation in which k is equal to the number of records. Thus during the training phase, the largest possible number

of examples is used, and each test set contains only one record. This approach provides exhaustive results, but it is computationally costly.

Part II

CAD for Peripheral Blood Images

Chapter 6

Background

6.1 Hematology

Hematology is the branch of medicine concerned with the study, diagnosis, monitoring, treatment, and prevention of blood and blood-forming organs diseases. Hematology studies the blood in health and pathological conditions, firstly to identify the patients health condition and, secondly, to predict how the bone marrow may have contributed to reaching that condition. Hematology, indeed, studies the relationship between the bone marrow and the systemic circulation. Many diseases, disorders, and deficiencies can affect the number and type of produced blood cells, their function, and lifespan. Usually, only healthy, mature or nearly mature cells are released into the bloodstream, but certain circumstances can induce the bone marrow to release immature and abnormal cells into the circulation. The Complete Blood Count (CBC) is one of the most frequently ordered tests to monitor the cell components distribution into the bloodstream. It offers various hematologic data represented by the numbers and types of cells in the peripheral blood circulation. The cells percentage is compared with the reference ranges to determine if the cells are present in their expected rate, if one cell type is increased, decreased or if immature cells exist. Reference ranges for blood tests are sets of values used to interpret a set of diagnostic test results from blood samples. Since it is difficult to prove that healthy-considered subjects may not have infections, parasitic infection and nutritional deficiency, it is more feasible to talk about reference ranges rather than normal ranges. A reference range is usually defined as the set of values in which 95% of the healthy population falls within. It is determined by collecting data from vast numbers of laboratory tests result from a large number of subjects who are assumed to be representative of the population. With automatic counters or the flow cytometry, an automated CBC can be performed quickly. However, if the results from an automated cell count indicate the presence of abnormal cells or if there is a reason to suspect that abnormal cells are present, then a blood smear is collected [LPDRF16]. A blood smear is often used to categorize and identify conditions that

affect one or more types of blood cells and to monitor individuals undergoing treatment for these conditions. The results of a blood smear analysis typically include a description of the appearance of the cells, as well as any abnormalities that may be seen on the slide. The manual analysis of blood smears is tedious, lengthy, repetitive and it suffers from the presence of a non-standard precision because it depends on the operator's skill. The use of image processing techniques can help to analyze, count the cells in human blood and, at the same time, to provide useful and precise information about cells morphology. Peripheral blood smears analysis is a common and economical diagnosis technique by which expert pathologists may obtain health information about the patients. Although this procedure requires highly trained experts, it is error-prone and could be affected by inter-observer variations. Moreover, blood cells' images taken from a microscope could vary in their illumination and coloration conditions, as shown in Figure 6.2. Typically, blood cells images contain three main components of interest: the platelets (or thrombocytes), the red blood cells (or erythrocytes) and the white blood cells (or leukocytes). It is worth considering that blood cells exist with different shapes, characteristics, and colorations, according to their types. A schematic representation is shown in Fig. 6.1 Many tests are designed to determine the number of erythrocytes and leukocytes in the blood, together with the volume, sedimentation rate, and hemoglobin concentration of the red blood cells (blood count). Besides, certain tests are used to classify blood according to specific red blood cell antigens, or blood groups. Other tests elucidate the shape and structural details of blood cells and hemoglobin and other blood proteins. Blood can be analyzed to determine the activity of various enzymes or protein catalysts, that either is associated with the blood cells or are found free in the blood plasma. Blood also may be analyzed from properties such as total volume, circulation time, viscosity, clotting time and clotting abnormalities, acidity (pH), levels of oxygen and carbon dioxide, and the clearance rate of various substances. There are specific tests based on the presence in the blood of substances characteristic of specific infections, such as the serological tests for syphilis, hepatitis, and human immunodeficiency virus (HIV, the AIDS virus) [Bri]. Among the several available blood tests, the most common are the blood cells counts, e.g., a CBC is a measure of the hematologic parameters of the blood. Included in the CBC is the calculation of the number of red blood cells (red blood cell count) or white blood cells (white blood cell count) in a cubic millimeter (mm^3) of blood, a differential white blood cell count, a hemoglobin assay, a hematocrit, calculations of red cell volume, and a platelet count. The differential white blood cell count includes measurements of the different types of white blood cells that constitute the total white blood cell count: the band neutrophils, segmented neutrophils, lymphocytes, monocytes, eosinophils, and basophils. A specific infection can be suspected from the type of leukocyte that has an abnormal value [DRLP16].

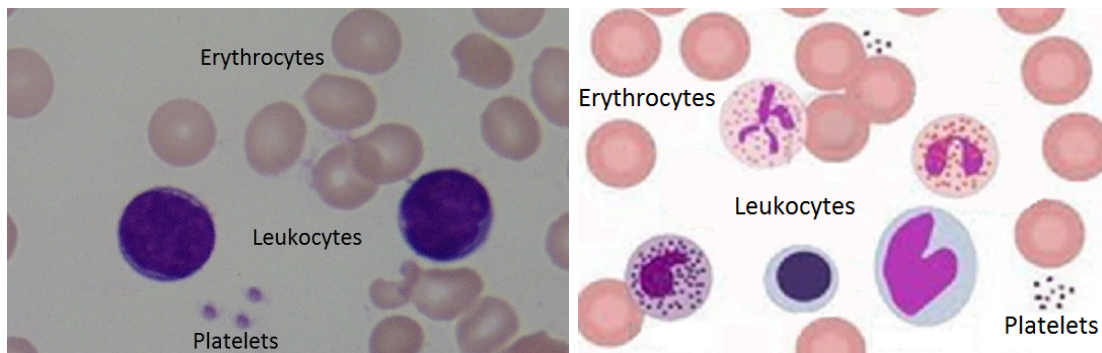


Figure 6.1: Peripheral blood smear components: a real image and a schematic representation.

6.2 Peripheral Blood Images

There are several components in blood smears containing peripheral blood samples. Consequently, these kinds of image usually consist of, at least, three principal objects of interest: the White Blood Cells (WBCs), the Red Blood Cells (RBCs) and the platelets (or thrombocytes). Platelets or thrombocytes are small non-nucleated disc-shaped cells with a diameter between 1 and 3 μm . Upon release into the peripheral blood from the bone marrow, they appear as fragments. They play a significant role in hemostasis leading to the formation of blood clots when there is blood vessel injury or bleeding, starting to clump together to form aggregates. There must be a sufficient number of platelets to control bleeding. If too few are present, or if they do not work correctly, the ability to form a clot becomes impaired and can be a life-threatening situation [Cie11]. Healthy, mature RBCs or erythrocytes are uniform in size, 7-8 μm in diameter, and do not have a nucleus as most other cells do. They are round and flattened like a donut with a depression in the middle instead of a hole (biconcave). Due to the hemoglobin inside the RBCs, they appear pink to red with a pale center once the staining process has been completed. Considering that not every RBC could respect its typical shape, any significant number of cells that are different in shape

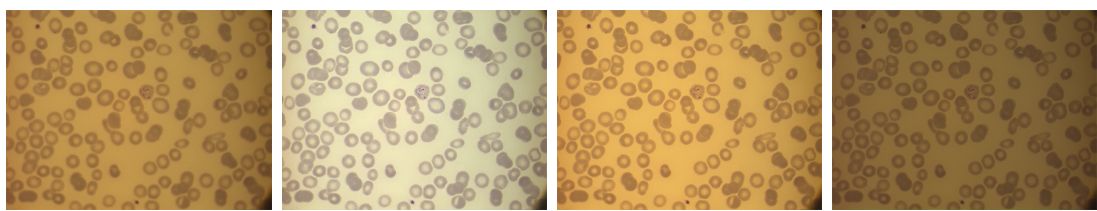


Figure 6.2: Different illumination conditions generate distinct images because of the absence of a standardized acquisition procedure. From left to right: acquisition of the same smear with four microscope's brightness levels. Courtesy of CHUV, Lausanne.

or size may indicate the presence of some diseases [EA13]. WBCs or leukocytes have a nucleus surrounded by cytoplasm, instead. For this reason, they are easily identifiable, as their nucleus appears darker than the background. However, the analysis and the processing of data related to the WBCs are complicated due to wide variations in cell shape, dimensions, and edges. The generic term leukocyte refers to a set of cells that are entirely different from each other. Indeed, although they are all derived from bone marrow stem cells, in the bone marrow, they differentiate themselves into two main groups: cells containing granules, called granulocytic or myelocytic, and cells without granules called mononuclear or lymphoid. Thus, we can distinguish between these cells according to their shape or size, the presence of granules in the cytoplasm and the number of lobes in the nucleus, as it can be seen in Fig. 6.3. The lobes are the most substantial part of the nucleus, and thin filaments connect them. WBCs mature into five distinct cells types, that include neutrophils, basophils, and eosinophils in the granulocytic group and lymphocytes and monocytes in the non-granulocytic group. Neutrophils are indeed the most common WBCs in a healthy adult, present in the human blood at a percentage ranging between 50 and 70%. They range in size from 10-15 μm and present a cytoplasm with pink or purple granules. They are distinguishable also due to the number of lobes present in the nucleus, which can range from 1 to 6 according to the cell maturation. They are involved in the defense against infections. Basophils are the least common of the granulocytes and represent only 0-1% of all leukocytes in human blood. They have a diameter of approximately 10 μm . Generally, basophils have an irregular, plurilobated nucleus that is obscured by large and dark granules. Eosinophils are easily recognized in stained smears due to the presence of large, red-orange granules, which include para-crystalline structures in the shape of a coffee bean. They are round, 10-12 μm in size, and have a nucleus with two lobes. Generally low in number, present at 1-5% in human blood, they most often increase in number in individuals with allergies and parasitic infections. Monocytes are usually the most voluminous WBCs, with a diameter of 12-20 μm and are often referred to as scavenger cells (phagocytes). They can ingest particles such as cellular debris, bacteria, or other insoluble particles. They represent 3-9% of circulating leukocytes. Their nucleus is large and curved, often in the shape of a kidney. Lymphocytes are usually the smaller WBCs, with a diameter of 7-12 μm . They are characterized as having a smooth, round nucleus and a small amount of cytoplasm and often a smooth chromatin pattern. They are very common in human blood, with a percentage of 20-45%.

Numerous diseases and conditions can affect the absolute or relative number of WBCs and their appearance on a blood smear. More details of the conditions that affect the number and the morphology of kind of cells are listed in Appendix A. Examples of the most common diseases that involve variation in shape and number of blood cells include anemia, hemophilia, general blood clots, and bleeding disorders while more severe cases that need to be diagnosed are leukemia, myeloma, and lymphoma. This thesis focused on the analysis of Acute Lymphoblastic Leukemia

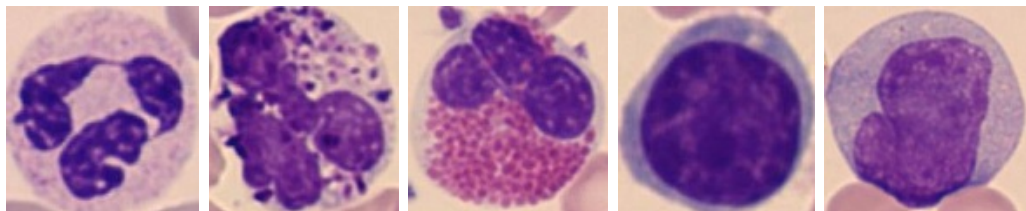


Figure 6.3: A comparison between different types of WBCs: neutrophils, basophils, eosinophils, monocytes and lymphocytes.

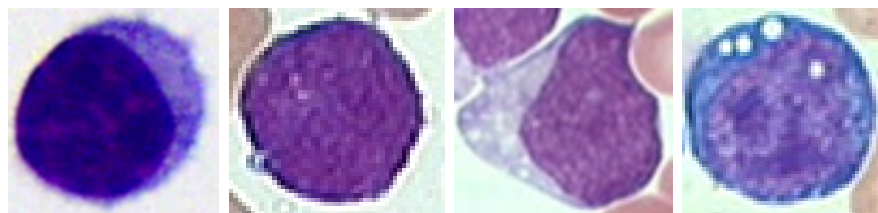


Figure 6.4: A comparison between lymphocytes suffering from ALL: a healthy lymphocyte, followed by lymphoblasts classified as L1, L2 and L3, respectively, according to the FAB [BCMT⁺76].

(ALL) and malaria.

6.3 ALL - Acute Lymphoblastic Leukemia

Leukemia is a blood cancer that can be detected through the analysis of WBCs. There are two types of leukemia: acute and chronic. According to the French-American-British (FAB) classification model [BCMT⁺76], acute leukemia is classified into two subtypes: acute lymphoblastic leukemia (ALL) and acute myeloid leukemia (AML). Here, only ALL has been considered, which affects a group of leukocytes called lymphocytes. ALL primarily affects children and adults over 50 years of age. The risk of developing ALL is highest in children younger than five years of age, and it declines and begins to rise again after age 50. Due to its rapid expansion into the bloodstream and vital organs, ALL can be fatal if left untreated [BCPP00]. Therefore, early diagnosis of this disease is crucial for a patients' recovery, especially for children. Diagnosis of ALL is based on the morphological identification of lymphocytes suffering from ALL, called lymphoblasts, by microscopy and the immunophenotypic assessment of lineage commitment and developmental stage [IGM13]. Lymphoblasts present morphological changes that increment with increasing severity of the disease. In particular, lymphocytes are regularly shaped and have a compact nucleus with regular and continuous edges, whereas lymphoblasts are irregularly shaped and contain small cavities in the cytoplasm, termed vacuoles, and spherical particles within the nucleus, termed nucleoli [LPS11] (Fig. 6.4).

The observation of blood smears by skilled operators is one diagnostic procedure available to initially recognize the ALL, where the automatic counter fails due to the presence of abnormal cells. Human visual inspection is tedious, lengthy and repetitive, and it suffers from the presence of a non-standard precision because it depends on the operator's skill; these disadvantages limit its statistical reliability. The use of image processing techniques can help count the cells in human blood and at the same time to provide information about cell morphology, making them less expensive and providing more accurate standards. One of the goals of this thesis is to provide a fully automatic procedure based on the analysis of blood smear images, to support medical activity. This procedure counts the WBCs present in the smear through a process of segmentation and detection. The detected WBCs are then classified as suffering from ALL or not.

6.3.1 Related Works

The progress of automated methods for the classification of blood cells from digitized images is a current problem in pattern recognition. These techniques can help to count the cells in human blood and, at the same time, be able to provide information on the morphological cells themselves. Unfortunately, for the analysis and processing of images, there are no standard techniques to apply to all types of images, but the processing must be adapted to the context. In particular, regarding the blood smear images, the processing techniques vary according to the type of blood cell to be analyzed. In the literature, few attempts of automated systems, based on techniques of image processing, able to identify and classify peripheral blood cells have been proposed. Moreover, the existing systems are only partially automated, combining manual steps to automated ones. Furthermore, most of them do not work on the entire analysis process, but on individual phases of the whole analysis process. This section will show the techniques most commonly used by different authors at different stages of the process.

The used methods of pre-processing depend on many variables, such as lighting conditions, the duration of the dye, defects caused by visual artifacts or not uniform background. The images should be processed to improve specific characteristics or to reduce further operations that could be required in the later stages of the analysis. The main issues addressed at this stage include noise reduction and enhancement of some structures of the images. Mohapatra et al. [MP10b, MPS10, MP10a, MPS14] used a median filter to remove the noise followed by an Unsharp filter. The median filter has been preferred to the average filter since it preserves details of edges and then they are enhanced with the use of the Unsharp filter. Other authors preferred operations based on the histogram such as contrast stretching or the histogram equalization to redistribute the grey level values. Often these two transformations have been used together or with other techniques, as the algorithm proposed in [MKA⁺10]. It starts from the greyscale image performs separately a contrast stretching and a histogram equalization. Then a series of arithmetic operations between the

two images just obtained is performed in order to highlight the nuclei of leukocytes. The results are impressive because it either enhances the nuclei of leukocytes and it drastically reduces the number of the other blood components, making further steps much more straightforward.

As previously said, different levels of segmentation are used in medical images analysis. In particular, for what concerns peripheral blood images two main levels are used: the level of cells segmentation, which aims to separate whole cells from the background or plasma and the level of segmentation that tries to separate the various components inside the cell, such as the nucleus from the cytoplasm or intracellular parasites. Several authors have proposed methods for effective segmentation of the nucleus of leukocytes, while there are few attempts of segmentation of the cytoplasm. The characteristic generally used for segmentation is the intensity value of grey level images. However, many authors showed how the use of a single channel from different color spaces could be used to highlight differences between blood components. Indeed the nuclei of the white blood cells are more in contrast on the Green component of the RGB color space [Cse92], while the cytoplasm of the white blood cells is more evident on the Hue component [WZZO06] or the Saturation component [HMH11] of the HSV color space. The Saturation component of the HSV color space is also useful to identify and separate erythrocytes [RDKJ00] when present in complex agglomerates of cells. Otherwise, they can be easily detected and counted with a threshold value computed using Zack algorithm from grey level images [BTKD11]. Based on this knowledge many algorithms of region growing have been proposed [KGHS96, LEC⁺98, LC02]. They use the pixels within the nuclei as seeds in order to segment the whole white blood cells. The cytoplasm is detected through iterative aggregation of the pixels surrounding the region of interest according to the homogeneity of the colors and the information of the gradient. Edge-based segmentation methods are rarely used in this contest since the boundaries between cells are not clearly defined. However, the performances of edge detection operations can be improved using morphological operators [PS04, Sco05] being able to connect in a better way the detected edges and restore the complete boundary of the cells. A huge number of papers has been proposed in the literature concerning the application of clustering methods to the segmentation of medical images [KP17]

A further problem in the analysis of peripheral blood cell images is the presence of cells grouped together or adjacent, as shown in Fig. 6.5. It does not allow an analysis of the single cells, such as the computation of shape descriptors or the proportion of cytoplasm and nucleus. *A priori* knowledge about the average size and shape of the cells allow working on sub-images extracted from the original image, by cutting a square around the nucleus previously segmented [KGHS96, SR03]. Thus, assuming that each sub-image has only one white blood cell using some restrictions on the shape and the color information it is possible to perform a clustering around the nucleus. Unfortunately, this assumption is not always true, and in fact, it is possible to find more than one nucleus on a sub-image that affects the result of the clustering. An improvement of this approach works on the whole images without

using the a priori knowledge about the size and shape. It is possible thanks to the distance transform [JRQ03] that associates to each pixel of the binary image its distance from the border. Thus, the maximum distance obtained can be used as a marker for a subsequent segmentation step [MdSV⁺97], or the distance image can be used directly as a shape delimiter for a watershed segmentation [Lin02]. The main drawbacks of these approaches are that the cells should be perfectly segmented since they work directly on the binary images. Furthermore, since the distance transform, in this case, works like a shape delimiter, it can separate only small agglomerates of cells that should have an almost circular shape.

Finally, [CMT⁺16] proposed a deep learning method for cells classification in a label-free environment. They also compared various learning algorithms including artificial neural network, support vector machine, logistic regression.

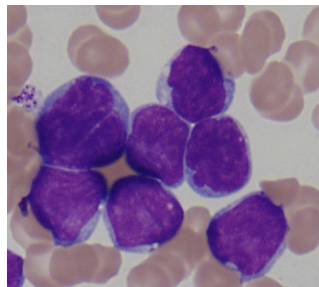


Figure 6.5: Crop of a sample image taken from ALL-IDB1. It represents a leukocyte clump.

The step of feature extraction is essential in the analysis of peripheral blood cells, as only with significant features, the system will be able to discriminate the various types of cells, the cells affected by diseases from the normal ones or the presence of other abnormalities in the blood. The idea is to extract the descriptors that best approach to the visual patterns indicated by pathologists. The color and texture descriptors are indeed the most discriminatory features of blood cells. Generally, this kind of images is acquired using the RGB color space that allows good discrimination of platelets, red blood cells, and white blood cells, especially if the analysis is extended to all RGB channels [AS02]. However, the differentiation of subclasses of cells such as various types of leukocytes, usually requires the use of other color spaces, taking into account all the color channels or only the most discriminatory such as the H channel of the HSV color space [HSP02]. Furthermore, geometrical features can be used to discriminate cells with abnormal size or with an irregular shape. Other geometrical features have explicitly been proposed to classify the type of nucleated cells since they can be distinguished not only using the ratio between cytoplasm and nucleus [PS04, Sco05, Sco06] but also extracting the number of lobes of the nucleus. Extract the number of lobes means to count the more substantial parts of the nucleus connected by thin filaments. It is not an easy task since the connection between the lobes sometimes can appear larger

than average and thus, also a skilled operator, could count two small lobes as it was only one. A good approximation of the number of lobes can be obtained by iterative erosion of the nucleus. The number of lobes corresponds to the connected components with an area more significant than a prefixed parameter [PS04].

Once the features have been extracted, they must be inserted in a process which classifies cells based on hematological concepts [BCPP00, SDH⁺91]. Different learning methods have been used to classify blood cells, but above all very different choices about the number of classes have been taken. The most frequent choice is the binary classification to distinguish healthy white blood cells from abnormal ones making use of the SVM classifier, which is excellent in the separation of binary classes with a pattern very close in space [MP10b, MPS10, MP10a, MPS14]. Mishra [Mis] showed that a highly appropriate feature extraction technique is required for the classification of the disease. Discrete Cosine Transform (DCT) has been used in association with a nucleus features extraction from the RGB image. Finally, they detect ALL on ALL-IDB images with SVM classifier. KNN classifier is also used, for example Abdeldaim et al. [ASEH] present a computer-aided ALL diagnosis system, which first segments each cell in the microscopic images, and then classifies each segmented cell to be normal or affected. The experiment based on ALL-IDB2 achieves the accuracy of 96.42% with a KNN classifier. Instead, when the number of classes is higher the most used classifier have been the Neural Networks, performing a separation into the five types of leukocytes [Sco06] or performing a separation into 7 classes, lymphocytes, neutrophils, eosinophils, other (monocytes and basophils), lymphocytic leukaemia L1, lymphocytic leukaemia L2 and non-lymphocytic leukaemia [BSa08].

In the following chapter, you will see the algorithms proposed to create a fully automated system for peripheral blood images. For clarity, each step of the whole process has been discussed separately following the order mentioned before and used for most of the methods presented in the literature. Furthermore, to make a comparison with the state-of-the-art, each step of the proposed method has been tested using the same dataset presented below.

6.3.2 White Blood Cells images Datasets

The main problem in the testing phase of an automated system is certainly the absence of many public datasets. A lot of authors have tested their methods by using only manual segmented ground truth samples or private datasets. These disadvantages do not allow a direct comparison with the results obtained by similar proposed systems, and it limits the reproducibility of possible innovations. Among the public datasets of peripheral blood samples image we found useful for our purposes, there are the following:

- ALL-IDB [LPS11]
- IUMS-IDB [SRTB14]

- SMC-IDB [MFG12]

Acute Lymphoblastic Leukemia Image Database (ALL-IDB), has been proposed by Donida Labati in [LPS11]. It is a public image dataset of peripheral blood samples of normal individuals and leukemic patients, and it contains the relative supervised classification and segmentation data. So, this dataset allows not only to assess the quality of the algorithms for cell counting but also to assess the ability to discriminate the white blood cells affected by leukemia from healthy ones. The sample images have been collected by the experts of the M. Tettamanti Research Center for childhood leukemia and hematological diseases, Monza, Italy. The ALL-IDB database has two distinct versions. The first version the ALL-IDB1 contains full-size original images that can be used for testing the segmentation capability of algorithms, as well as the classification systems and image preprocessing methods. The second version the ALL-IDB2 is a collection of cropped area of interest of normal and blast cells that belong to the ALL-IDB1 dataset, so it can be used only for testing the performances of classification systems.

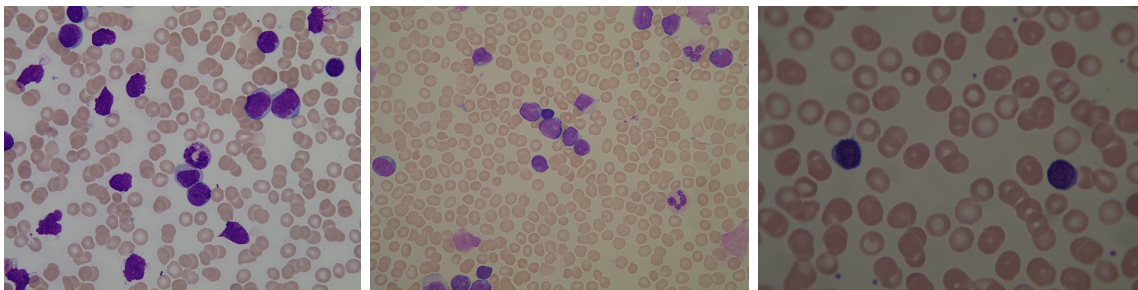


Figure 6.6: Sample images from the ALL-IDB1

In both versions of the dataset, each image has an associated text file containing the coordinates of the centroid of each candidate lymphoblast, which was manually labeled by a skilled operator and can be used as ground truth for classification. The dataset ALL-IDB1 includes 108 images in JPG format with 24-bit color depth. Most of the images in the dataset were captured with an optical laboratory microscope, with different magnifications ranging from 300 to 500, coupled with a Canon PowerShot G5 camera and their resolution is 2592x1944. The remaining images were acquired with a microscope at a constant magnification, combined with an Olympus C2500L camera and their resolution is 1712x1368. Some images belonging to the ALL-IDB1 are shown in Fig. 6.6.

The sample images show that there are many differences either regarding color and illumination or resolution and cells dimension. The dataset ALL-IDB2 includes 260 images in TIFF format with 24-bit color depth. As said previously, these images are cropped areas of interest, containing a single leukocyte per image, belonging from the first version of the database. These images, differently from the first ones, have

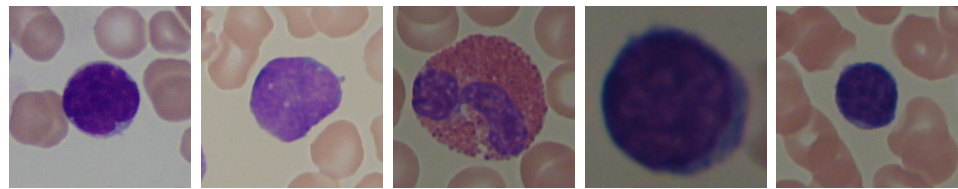


Figure 6.7: Sample images from the ALL-IDB2

a standard size of 257×257 , but being cropped area of them, they present the same issues about color, illumination and cells dimension, as it can be seen in Fig. 6.7.

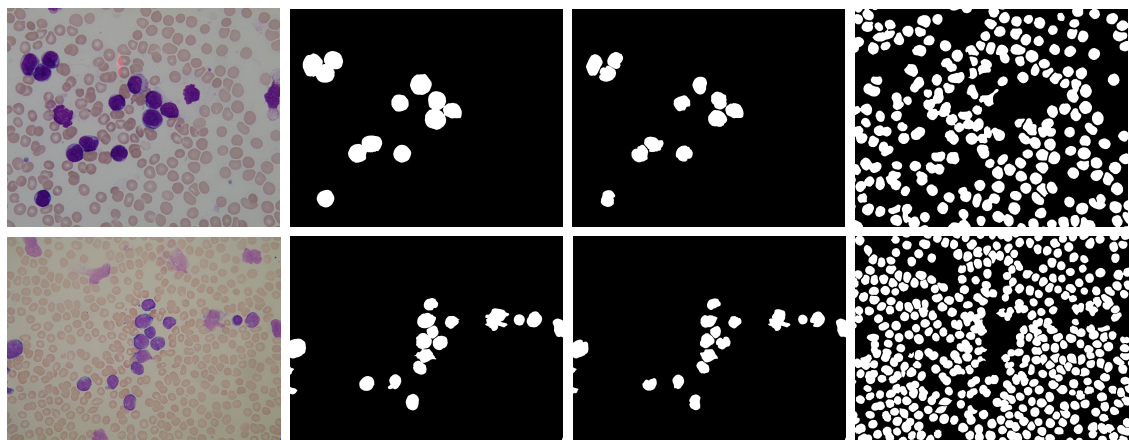


Figure 6.8: From left to right: original images from the ALL-IDB1 database, ground-truth for whole leukocyte, only nuclei and RBCs

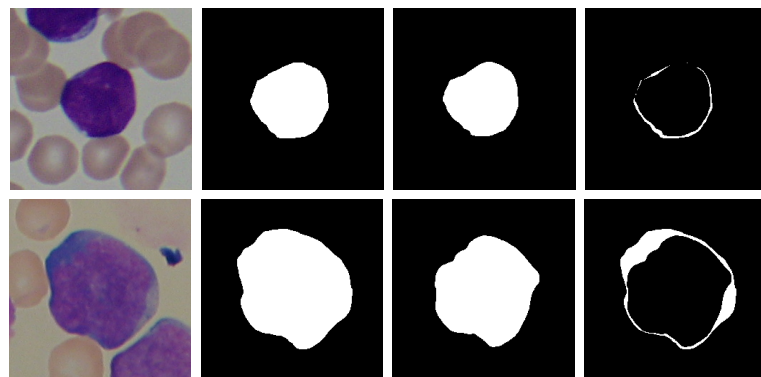


Figure 6.9: From left to right: original images from the ALL-IDB2 database, ground-truth for whole leukocyte, only nucleus and only cytoplasm

To evaluate the segmentation performances of the proposed method, 52 images belonging to the ALL-IDB1 have been manually segmented by skilled operators, creating four ground-truth images for each sample. One for the entire WBCS, one for

the whole of the RBCs, one for WBCs nuclei and, finally, one for WBCs cytoplasm. Fig. 6.8 shows some images belonging to the ALL-IDB1 and their relative ground-truth images. Ground-truth images have also been extracted for images belonging to the ALL-IDB2, but in this case, the manual segmentation is only devoted to the analysis of leukocytes, so the ground truth images display only the cytoplasm and the nucleus of the leukocyte, as it can be seen in Fig. 6.9. Despite our main efforts are devoted in designing a method able to achieve a robust segmentation with different image datasets, in our previous works [RLP15a, RLP15b] just the ALL-IDB dataset has been used, mainly because the proposed approach exploited the subdivision of the ALL-IDB dataset. Indeed, the ALL-IDB2 images were used to create the training set, being able to develop a robust model to segment optimally the original images in ALL-IDB1. Our aim has always been to let our segmentation algorithm work for different kinds of images and, consequently, different datasets. For this reason, two more datasets have been used for testing the proposed method. IUMS-IDB is provided by the Iran University of Medical Science [SRTB14]. It presents 100 microscopic images of size 732×572 , taken from peripheral blood of 8 healthy subjects. These images are truly different from the ones present in the ALL-IDB, since the microscope slides have been smeared and stained with a different staining technique. SMC-IDB, on the other hand, has been proposed in [MFG12], presented at IEEE's 2012 SMC conference. It has been acquired from slides stained with the same staining technique as ALL-IDB. Nevertheless, the images are different, since they have been acquired with a different combination of microscope and camera. This dataset provides a total of 367 peripheral blood images of size 640×480 . Sample images taken from IUMS-IDB and SMC-IDB are shown in 6.10.

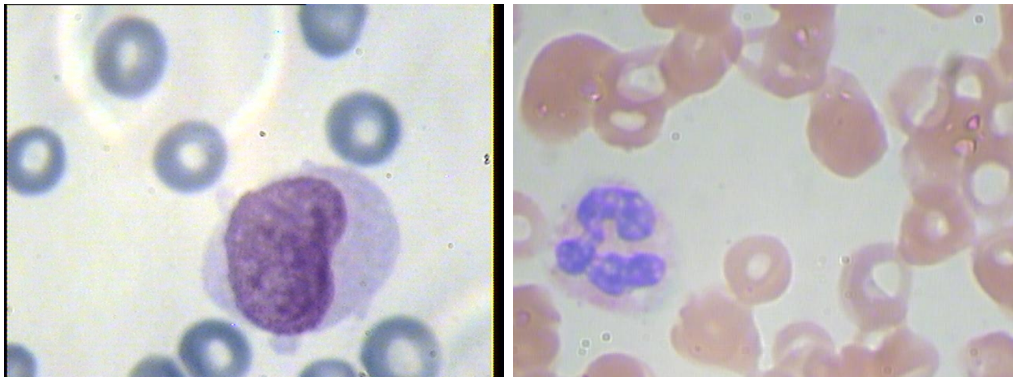


Figure 6.10: From left to right: sample image from IUMS-IDB and SMC-IDB.

6.4 Malaria

This chapter explains in detail the characteristics of malaria disease in general, how it is caused, how it affects humans and, finally, the details of malaria parasites. It refers the survey work [LDRK18]. Malaria is an epidemic health disease so rapid and accurate diagnosis is necessary for proper intervention. Human malaria infection is not strongly related to cell count, but it needs different tests in order to be identified. It can only be caused by parasitic protozoans belonging to the *Plasmodium* type. The parasites are spread to people through the bites of infected female Anopheles mosquitoes, called "malaria vectors". There are five parasite species that cause malaria in humans and two of these species, *Plasmodium falciparum* and *Plasmodium vivax*, constitute the greatest threat. *Plasmodium ovale*, *Plasmodium malariae* and *Plasmodium knowlesi* are the three remaining species that are less dangerous in humans [WHO16], as shown in Figure 6.11. All five species may appear in four different life-cycle stages during the infection phase in peripheral blood: ring, trophozoite, schizont, and gametocyte. Some examples are shown in Figure A.10. The life-cycle-stage of the parasite is defined by its morphology, size and the presence or absence of malarial pigment. The species differ in the changes of infected cell's shape, the presence of some peculiar dots and the morphology of the parasite in some of the life-cycle-stages [Som11].

6.4.1 Related Works

In an image analysis field, especially when we refer to complex computer-aided pipelines, preprocessing methods are particularly used to improve the image data by suppressing unwanted noise or enhancing some image features for further processing. It is worth mentioning preprocessing methods because they are an essential step regarding the image analysis field, but, for what concerns the malaria-affected blood image analysis, in our review, we mainly found methods that operate for illumination correction and noise filtering purposes. Generally speaking, digital microscopy images can be acquired in different lighting conditions, with several types of acquisition devices or from blood smears stained with various staining protocols, and, consequently, the features of similar images could differ a lot. Different techniques for illumination correction have been suggested to reduce such variation, e.g., a lot of authors work with grayscale-converted images as an illumination correction method. On the other hand, noise filtering aims to remove the noise introduced by mishandling the slides and the camera settings. Morphological operators have been extensively used as preprocessing for image enhancement in significant studies. Erosion and dilation operations on raw smear images allow for discarding undesired patterns and help in the selection of required cells or regions of interest. Morphological operators are useful for the removal of unwanted objects, holes filling, splitting, thinning and thickening. Different researchers during the automated diagnosis of malaria used morphological operations in the preprocessing phase, and the most

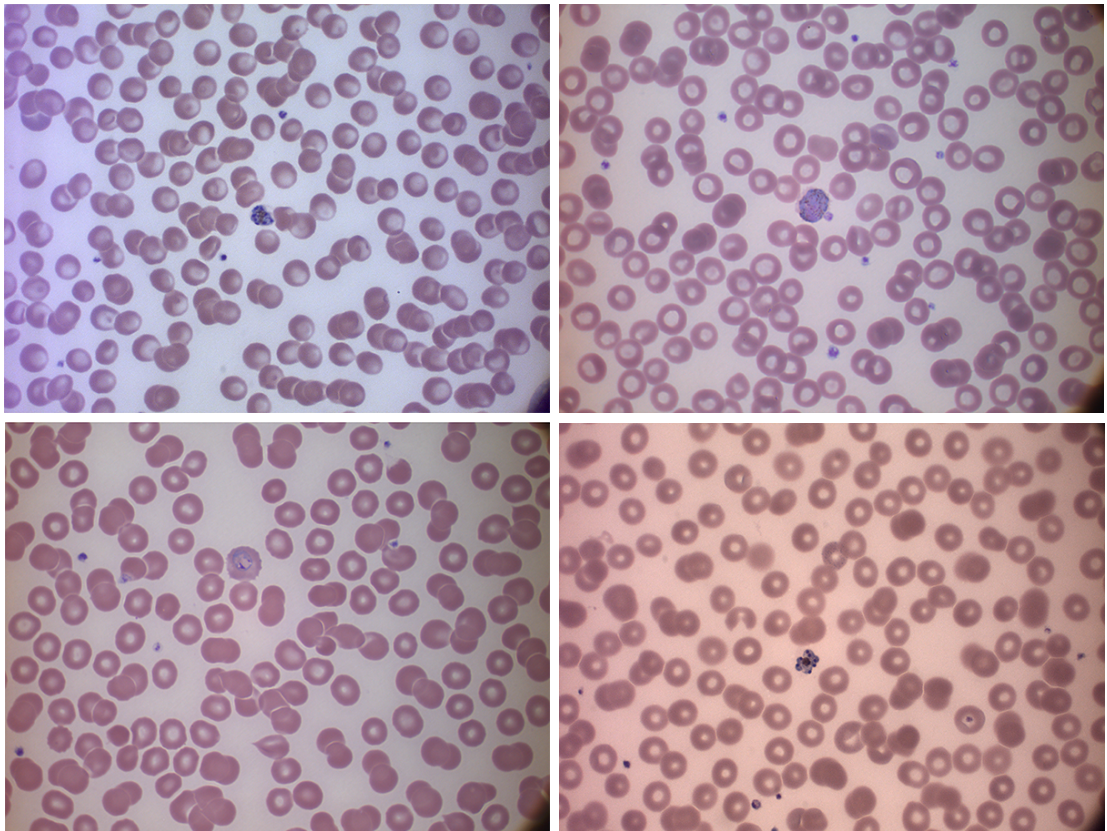


Figure 6.11: Types of human malaria parasites: from left to right, *P. falciparum* in its schizont stage, *P. vivax* in two gametocytes specimens and one ring stage, *P. ovale* in its ring stage, *P. malariae* in its schizont stage. Courtesy of CHUV, Lausanne.

recent are listed below.

In [GBea16], Gonzalez-Betancourt et al. proposed a system to determine markers for watershed segmentation based on the Radon transform and mathematical operators. In the first step of the process, small irrelevant structures and part of the noise are eliminated by a morphological filter, in order to ensure the preservation of the edges of the cell. Image smoothing is performed by a morphological erosion-reconstruction and dilation-reconstruction filter with a disk structuring element of a radius equal to 20 pixels, which is 0.274 times smaller than the average radius of the RBCs.

In this way, the influences of the size and the shape of the structures can be separated in the smoothing process. At the same time, the objects that are not eliminated remain unchanged. Besides, a morphological closing is performed with a disk structuring element having a radius smaller than half the average of the RBCs radii, to connect the possible (more than one) markers that can appear on a single cell.

In [KKM12], Kareem et al. illustrated a morphological approach for blood cell identification and used image features such as intensity, histogram, relative size and geometry for further analysis. Before the identification of blood cells, the authors propose different morphological filtering based on the size of RBCs for platelets and artifacts elimination. Dilation is performed by a concentric ring structuring element and erosion by a disk-shaped structuring element. The radius of the structuring element depends on the radius of the RBCs so that all the components smaller than the RBCs can be removed.

The system proposed in [OPEea17] by Oliveira et al. is based on image processing, artificial intelligence techniques, and an adapted face detection algorithm to identify Plasmodium parasites. The latter uses the integral image and haar-like features concepts, and weak classifiers with adaptive boosting learning. The search scope of the learning algorithm is reduced in the preprocessing step by removing the background around blood cells employing morphological erosions both for training and for testing.

Romero-Rondon et al. in [RRSRBRMC16] presented an algorithm that uses morphological operations, the watershed method, the Hough transform and the clustering method of k-means to detect overlapped RBCs. In the preprocessing stage, white blood cells and platelets are removed before the segmentation task. During this step, some noise, the WBC cytoplasm, and platelets remain on the image. Therefore, the small objects are removed using a morphological opening, and then the image is dilated with a disk-shaped structuring element.

Reni et al. in [RKM15] described a new algorithm for morphological filtering of the blood images as a preprocessing tool for segmentation. Conventional morphological closing on blood images removes the unwanted components but also useful information. On the contrary, the proposed method preserves the necessary knowledge of foreground components while eliminating noise and artifacts.

In the method proposed in [SRZT13] by Sheikhhosseini et al., the first phase is the stained object extraction that detects candidates' objects that can be infected by malaria parasites using intensity and color. Before detecting the stained objects, the method firstly extracts the foreground. The foreground image is a binary image that is produced after applying morphological hole filling on such pixels that have lower intensity value than average intensity value of the green layer. After the stained objects' extraction process, a series of morphological operations are also employed to eliminate small components and complete the final stained objects.

An edge-based segmentation of erythrocytes infected with malaria parasites using microscopic images is proposed by Somasekar et al. in [SR15]. A fuzzy C-means clustering is applied to extract infected erythrocytes, which is further processed for the final segmentation. A morphological erosion is used to erase some small noises and spots before the segmentation and holes inside the infected erythrocytes are filled using a morphological hole filling operation for the final segmentation.

In [TDK10], Tek et al. presented a complete framework to detect and identify malaria parasites in images of Giemsa stained thin blood film specimens. In addi-

tion, the system is able to identify the infecting species and life-cycle stages. The preprocessing step of the proposed method is applied to reduce the variations in the observed size, intensity, and color of the cells and stained objects before the detection and classification steps. The aim is to correct the non-uniform illumination in the images. The estimation is based on a morphological closing operation using a sufficiently large structuring element. Enough large size for an input image is determined automatically concerning its average cell size computed from the area granulometry distribution.

The median filter is often used for reducing impulse noise. Several studies have used it to enhance microscopic images of peripheral blood smear towards the characterization of malaria followed by adaptive or local histogram equalization. Local low pass filter and local adaptive histogram equalization techniques have also been applied to enhance the pathological image quality. Das et al. [DMC15] showed that the geometric mean filter provides better performance towards improving peripheral blood smear images. Di Ruberto et al. [DRLP16] proposed an approach to overcome the problem of uneven illumination conditions in image acquisition. For this purpose they designed an illumination pattern that simulates the classic visual defects introduced by the digital microscope lenses, that is the vignetting effect. Starting from the smallest radius, they applied different illumination patterns, created modifying the radius of the Gaussian curve, to the original images. Then, a similarity value measures the difference regarding pixels between the original images and the corrupted ones.

Segmentation is a critical step in image analysis because it permits the identification and separation of the regions that compose an image, according to specific criteria of homogeneity and separation. Its main target is to divide the image into parts that have a strong correlation with objects or areas of the real world contained in the image. The commonly used segmentation methods essentially operate considering characteristics such as the brightness value, colour, and reflection of the individual pixels, identifying groups of pixels that correspond to spatially connected regions. As for many problems of image processing, there is no standard solution valid in general. Therefore different segmentation techniques can be applied, according to the characteristics of the images to process and of the objects to segment. Medical images segmentation is typically performed using two main strategies: the first level aims to separate whole cells or tissues from the background and the second one seeks to separate the tissue structure in different regions or the cell in their components, as the nucleus from the cytoplasm or intracellular parasites. The latter case is commonly used in applications in which the cell class depends on the morphological characteristics of its components.

Several other authors attempted to use thresholding combined with morphological operations as a segmentation method in their computer-aided systems, and they are described as follows.

Arco et al. in [AGR⁺14] worked on thick blood films and proposed a method that uses an adaptive thresholding based scheme, which also allows a valid classification

of pixels. This means that the election of whether a pixel belongs to the background or the signal (parasites and white blood cells) is only established by the pixels around it, that is its neighborhood. Then, morphological methods are applied to evaluate the area of connected components, labeling those belonging to parasites and counting their number.

Anggraini et al. [ANP⁺11] proposed a method for separating blood cells, parasites and other components from the background in a microscopic field of a thin blood smear. They applied several global thresholding methods and visually compared the results to determine which technique yields the best result qualitatively. The binary image was then subjected to a hole filling morphological operator and applied as a marker to label blood cells. From each identified cell (RBC and WBC), constituents of the parasite (nucleus and cytoplasm) were extracted using multiple thresholds.

Dave et al. in [DU17] performed image segmentation using histogram-based adaptive thresholding followed by mathematical morphological operations (erosion and dilation). The detection of infected RBCs is based on an unsupervised learning technique.

The automated method proposed in [EHZ11] by Elter et al. for parasite detection and identification worked on thin blood film acquired with Giemsa stain. The authors found that the G and B channels of the RGB color are outstanding features to identify objects containing chromatin in Giemsa stained blood films are considered highly discriminative and also almost independent of differences in illumination and staining intensity. They transformed the colour input image into a monochrome image $I(x,y)$, which highlights objects containing chromatin: $I(x,y) = \arctan \frac{I_{green}(x,y)}{I_{blue}(x,y)}$. In this work, mathematical morphology has been used with a black top-hat operator to separate MP from both leukocytes and platelets, with a non-flat paraboloid structuring element with a radius of 9 and a slope of one pixel. It should be taken into account that these fixed parameters might not be suitable for images with different pixel resolutions. A thresholding operation follows the black top-hat operator with a fixed threshold, which, according to the authors, is reliable given the independence of the G and B channels concerning illumination and staining intensity. However, the authors do not define the value of this fixed threshold in their paper.

Kareem et al. in [KMK11] used the Annular Ring Ratio transform method. Before applying it, a preprocessing phase for removing platelets, parasites and other artifacts in the image has been performed. In the proposed method, the image after being converted to grayscale undergoes a morphological opening similar to closing. Unlike conventional closing (dilation followed by erosion), which uses the same structuring element, two different structuring elements are used: a concentric ring for dilation and a disk for erosion. The inner and outer diameter of the dilation ring is set to 35% and 70% of RBCs size, respectively, and the erosion disk has the same diameter. Therefore, considering that fixed manually defined parameters are used for this strategy, the results may substantially differ depending on the image resolution. This approach results in locating only the stained components in the

image instead of all the cells and hence will not only speed up the operation but reduce the complexity.

Mushabe et al. [MDD13] used morphological and statistical classification to detect malaria in blood smears by identifying and counting red blood cells and Plasmodium parasites. Morphological operations and histogram-based thresholding are used to extract RBCs, and boundary curvature calculations and Delaunay triangulation are used for splitting clumped RBCs. They worked on Giemsa-stained thin blood smears.

In [RPRD06], Ross et al. proposed a method that provides a positive or negative diagnosis of malaria and differentiates parasites by species. The segmentation step relies on a six-step thresholding selection strategy. It aims to identify and segment potential parasites and erythrocytes from the background. Mathematical morphology has been used in several key steps of the procedure. Hole filling is used in the first step to fill RBCs' binary masks obtained from first thresholding. Afterwards, step 4 employs RBCs' morphological reconstruction with parasites' mask, found in step 2, for identifying infected cells. In step 5, a morphological opening filter, using a disk-shaped SE with a radius equal to the mean erythrocyte radius less the standard deviation, is applied to the grayscale, morphologically filtered, green component to remove any objects smaller than an erythrocyte. The morphological gradient (the difference between dilation and erosion of the image) is then calculated using a diamond-shaped SE with unity length. Finally, in step 6, the intersection of morphological gradient image and the dilated cell cluster is calculated. This image is then transformed into a binary image by thresholding any value greater than zero. A series of morphological operations, namely a closing operation, thinning, and spur-removal are then applied to generate a contour of the segmented erythrocytes. Contours are filled, and the segmented mask is again reconstructed with the correct parasite marker image to result in a segmented mask of infected cells. RBCs and parasites masks are consequently ready for the next generation step.

Savkare et al. [SN11b] worked on thin blood films with Giemsa staining and used a global threshold and Otsu threshold [Ots75] on the grayscale enhanced image (green channel) for separating foreground from background. Hole filling has been performed on identified cells, and morphological operators have been used to identify overlapping cells. Then, a watershed transform has been applied for separating overlapped cells.

Besides, in the method proposed in [SR17] by Somasekar et al., the segmentation of the infected parasites is based on thresholding. It is achieved in two stages by maximizing the between-class variance of an original image and consequently by an iterative threshold selection from a stage-one threshold image with suitable stopping criteria. The segmented results are post-processed to improve the accuracy of malaria parasites detection by morphological operators (erosion and closing).

On the other hand, a lot of works have been realized through mathematical morphology and granulometry in the segmentation stages, even in combination with thresholding strategies. They are briefly analyzed below.

Ahirwar et al. [APA12] based their approach on thresholding and granulometry. The histogram of the complemented green component has been used, and it is said to be a bimodal distribution in all the considered images. Then, both local and global thresholds are used, and the union of the two binary images is chosen as the parasite marker image. A morphological opening filter, using a disk-shaped SE with a radius equal to the mean erythrocyte radius less the standard deviation, is applied to the grayscale morphologically filtered green component of the image to remove any objects smaller than an erythrocyte. The morphological gradient is then calculated using a diamond-shaped SE with unity length. The segmentation method is applied to each object in the reconstructed binary image of erythrocytes individually. Those objects that do not exceed the area of a circle with a radius equal to the mean erythrocyte radius plus the standard deviation are regarded as being single cells and are unmodified. On the other hand, the clumped cells are segmented as follows. First, the intersection of the morphological gradient image and the dilated cell cluster is taken. This image is then transformed into a binary image by thresholding any value greater than zero. A series of morphological operations, namely a closing operation, thinning, and spur removal is then applied to generate a contour of the segmented erythrocytes. The contours are filled, and the segmented mask is again reconstructed with the correct parasite marker image to result in a segmented mask of infected cells.

Di Ruberto et al. [DRDKJ02] aimed to detect the parasites utilizing automatic thresholding based on a morphological approach applied to cell image segmentation, which is more accurate than the classical watershed-based algorithm. They applied grey scale granulometries based on opening with disk-shaped elements, flat and hemispherical. They used a hemispherical disk-shaped structuring element to enhance the roundness and the compactness of the red blood cells improving the accuracy of the classical watershed algorithm, while they used a disk-shaped flat structuring element to separate overlapping cells. These methods make use of the red blood cell structure knowledge, which is not used in existing watershed-based algorithms.

Khan et al. in [KASS11] presented a novel threshold selection technique used to identify erythrocytes and possible parasites present on microscopic slides that dramatically benefit from morphological operations, such as granulometry and morphological reconstruction.

In [RdCEC17], Rosado et al. proposed a system using supervised classification to assess the presence of malaria parasites and determine the species and life cycle stage in Giemsa-stained thin blood smears. For the RBCs segmentation, they used an adaptive thresholding approach followed by a closing morphological operation with an elliptical structuring element.

Soni et al. [SMK11] performed segmentation of erythrocytes by using granulometry as well. The size and eccentricity of the erythrocytes are also required for the calculation of some feature values (as these can be indicative of infection). The shape of the objects (circular erythrocytes) is known a priori, but the image must

be analyzed to determine the size distribution of objects in the image and to find the average eccentricity of erythrocytes present. Grayscale granulometries based on opening with disk-shaped elements are then used. Non-flat disk-shaped structural elements are applied to enhance the roundness and compactness of the red blood cells and flat disk-shaped structural elements applied to segment overlapping cells. The object to be segmented differs significantly in contrast to the background image. Changes, in contrast, can be detected by operators that calculate the gradient of an image. The gradient image can be computed, and a threshold can be applied to create a binary mask containing the segmented cell. The binary gradient mask is dilated using a vertical structuring element followed by a horizontal structuring element. The cell of interest has been successfully segmented, but it is not the only object that has been found. Any objects that are connected to the border of the image can be removed.

In Tek et al. [TDK10], the localization of the parasites is achieved after a foreground and background segmentation step. Firstly, a rough foreground image using morphological area top-hats (using the average cell area value) is extracted. Then, from these rough foreground and background regions, two different threshold values are determined and used in morphological double thresholding of the input grey level image to produce a refined binary foreground mask. From the foreground image, the stained pixels are detected using a thresholding approach again and finally used as markers to extract the stained objects by morphological area top-hats based on the estimated average area value.

In [YAM12], Yunda et al. proposed a method for *P. vivax* parasite detection. The segmentation phase is a combination of border and region detection that allows rejection of the image background and permits identifying each of the objects. Initially, the morphological gradient method is used to enhance the borders of previously found objects. It is followed by a threshold detection stage using the K-Median method. Furthermore, a Laplacian operator was used to discriminate the pixels that are interior or exterior concerning the regions of the images and then erosion operation followed by two dilations were applied to delete the pixels that did not make part of any object. In the end, Absence of Gradients and Nernstian Equilibrium Stripping (AGNES) and K-Median techniques were applied to assign the remaining number of pixels to each region, using the image regions previously identified as objects and background as the starting point.

Several authors used marker-controlled watershed [Soi04] with the morphological approach, as described in the following.

Das et al. in [DGC⁺11, DGP⁺13, DMC14, DMC15] segmented erythrocytes as aforesaid and then morphological operators are used to eliminate unwanted cells like leukocytes and platelets. Moreover, overlapping erythrocytes are segmented by using a marker-controlled watershed segmentation technique.

In [DSSL17], Devi et al. proposed a computer-assisted system for quantification of erythrocytes in microscopic images of thin blood smears. The performance of the system in classifying the isolated and clump erythrocytes by geometric features is

evaluated for the different classifiers. The clump erythrocytes are segmented using marker-controlled watershed with h-minima as an internal marker.

In [DRB⁺15], Dey et al. presented an automatic system for segmenting platelets, useful for identifying the disease like malaria, using a color based segmentation and mathematical morphology (opening operations with a disk element of radius 2).

In the study presented in [DGR09] by Diaz et al. for quantification and classification of erythrocytes in stained thin blood films infected with *Plasmodium Falciparum*, the authors used connected morphological operators in the segmentation step. The RBCs are detected as follows: firstly, a pixel classification allowed for labeling each image pixel as either background or foreground, based on its color features. Afterward, an inclusion-tree structure is used to represent the hierarchical object relations between background and foreground so that a filtering process allows for removing irrelevant structures such as artifacts generated at the staining or digitization processes.

Khan et al. [KASS11], among other experimentations, used it to try to separate overlapping cells because, according to their statements, the watershed transform can isolate touching cells, but it is not sufficient for overlapping cells.

In the algorithm described by Romero-Rondon et al. in [RRSRBRMC16], the detection of overlapped RBCs is still based on marker-controlled watershed transform. To define the suitable markers in the watershed transform, they used three different approaches, based on a morphological erosion operation, on Hough transform and on a clustering method of K-means.

Savkare et al. in [SN15] segmented cells using K-mean clustering and global threshold. Overlapping cells are separated using a Sobel edge detector and watershed transform, applied to each cluster separately. Over-segmentation is minimized by a series of morphological operations, like erosion and dilation, utilizing disk-shaped structuring elements.

In [SN11a], an approach to detect red blood cells with the following classification into parasite infected and healthy cells for further estimation of parasitemia is proposed. For separation of overlapping cells, the watershed transform is applied on a distance transform of a binary mask of cells having a larger area.

In [Špr09], Špringl performed red blood cell segmentation by using marker-controlled watershed transformation based on the image gradient. Markers are computed as a combination of the binary mask of the red blood cells and centers of the cells that are computed using a similar algorithm that was utilized for the evaluation of the average cell radius. The binary mask is obtained by thresholding the grayscale image with an automatically estimated threshold using the Otsu method [Ots75].

In [SRPP15], Sulistyawati et al. combined morphological operations (erosion, dilation, opening, and closing) and blob analysis to segment and identify malaria parasites with a high degree of accuracy.

Tek et al. in [TDK06] proposed a classifier-based method for the segmentation stage, which relies on a Bayesian pixel classifier to distinguish between stained and

non-stained pixels. In particular, they used a non-parametric approach based on histograms to produce the probability density functions of stained and non-stained classes. Stained pixels can belong to other components such as WBCs, platelets or artifacts, in addition to the parasites, and so the detection procedure requires a further classification to distinguish among parasite and non-parasite pixels. However, the stained pixels have to be represented as connected sets, representing stained objects, to extract features for the classifier. Furthermore, top-hat extraction and infinite reconstruction were applied to find the regions that include the objects.

Feature extraction has the aim of reducing the computational complexity of the subsequent process and facilitating a reliable and accurate recognition for unknown novel data, considering that the input data to an algorithm could be too large to be processed, and it could be redundant (e.g., the repetitiveness of pixels patterns in an image). Moreover, the in-depth understanding of the domain-specific knowledge gained by human experts on the problem being addressed can be of extreme importance for the design of a reliable and effective feature extraction engine [Jia09]. It starts by determining a subset of the initial features, and this procedure is called feature selection. The selected features are expected to contain the relevant information from the input data so that the desired task can be performed by using this reduced representation instead of the complete initial data. Malaria parasite infection causes microstructural changes in erythrocytes. The microscopic features of the RBCs are usually specific to morphology, intensity, and texture. They may also represent the differences that occur among healthy and unhealthy cells. Most of the studies have reported both textural and geometric features for describing malaria infection stages [DMC15]. Generally speaking, features may be distinguished according to the following characteristics: morphological features and textural and intensity features.

It is a well known mathematical morphology approach to compute a size distribution of grains in binary images, using a series of morphological opening operations. It is the basis for the characterization of the concept of size. Some authors used area granulometry for preprocessing purposes in malaria characterization [TDK10], even though it is certainly effective for extracting cell size features' information [Špr09, TDK06, MAAB13]. In [TDK10], local area granulometry combined with the color histogram is used as features. The area granulometry feature is calculated locally on the binary mask of the stained objects, for the RGB channels, and then concatenated. Morphological features are also used in [RPRD06] (erosion dilation), in [DGC⁺11] (opening, closing) and in [DRDKJ02] (skeleton) to classify parasites.

6.4.2 Malaria parasites morphology

A blood smear image, obtained through a microscope, is presented in fig. 6.14. It typically contains at least three regions of interest: white blood cells (or leukocytes), red blood cells (or erythrocytes) and platelets (or thrombocytes). Two different categories of leukocytes exist granulocytes (composed, in turn, of neutrophils, basophils,

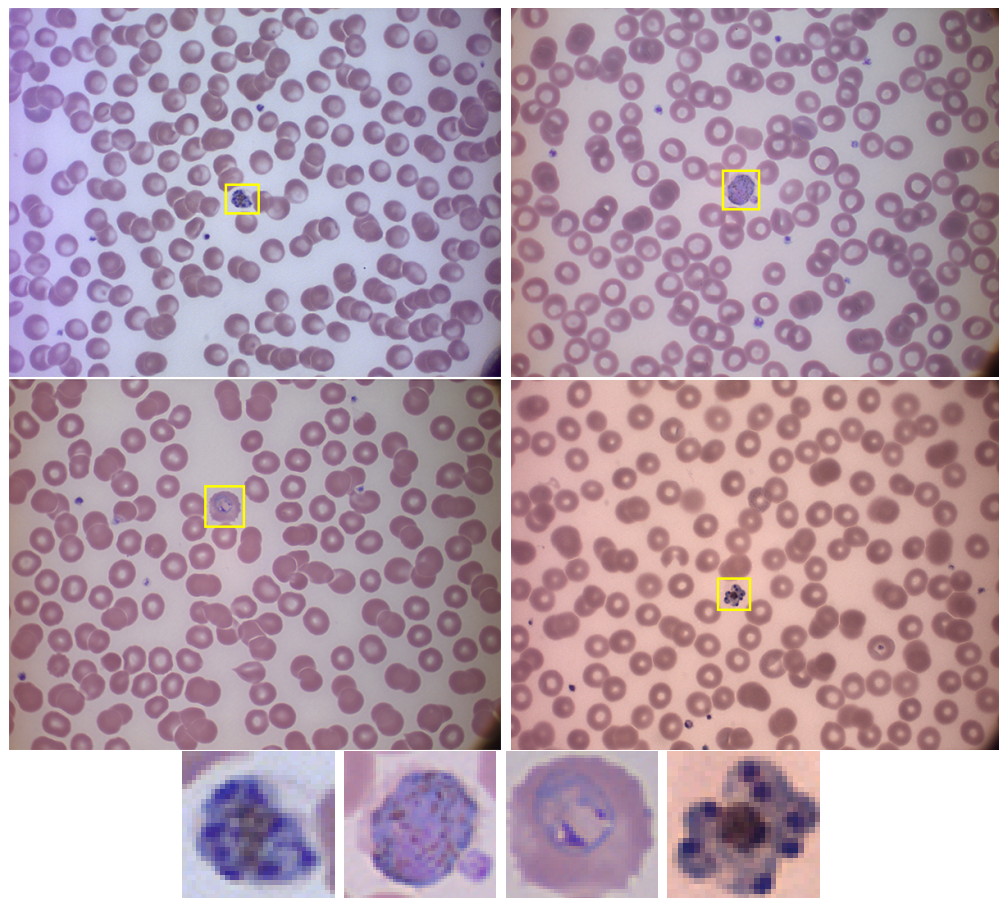


Figure 6.12: Types of malaria parasites: from top left, clockwise, *P. Falciparum* in its schizont stage, *P. Vivax* in a gametocytes specimen, *P. Malariae* in its schizont stage, *P. Ovale* in its ring stage. All parasites have been surrounded with a yellow box. Underneath, from left to right: crops of *P. Falciparum* schizont, *P. Vivax* gametocyte, *P. Ovale* ring and *P. Malariae* schizont, taken from the boxes. Courtesy of CHUV, Lausanne.

and eosinophils). On the other hand, leukocytes without granules are called agranulocytes (composed of lymphocytes and monocytes). Erythrocytes do not have any subcategory even though malaria parasites (MPs) can infect them, consequently modifying their shape, morphology or coloration conditions. In particular, fig. 6.12 shows several examples of malaria parasites in their different life stages and type. Although MPs infect only RBCs, a blood smear image representing both WBCs (particularly granulocytes) and MPs could be tough to analyze because of the similarities in coloration and shape between parasites and WBC grains, as shown in fig. 6.14.

MP-IDB collects four malaria parasite species: Plasmodium Falciparum, Ovale, Malariae, and Vivax, in four different life-cycle stages: ring, trophozoite, schizont,

and gametocyte. *Plasmodium Falciparum* trophozoite and schizont are very rare, and they are not present in our data collection. A complete set of examples, extracted from the dataset, are shown in fig. 6.13. The morphology, the size and the presence or absence of malarial pigment of the parasites define their life-cycle-stage. The species differ in the changes of infected cells shape, the presence of some peculiar dots and the morphology of the parasite in some of the life-cycle-stages [Som11]. An automated malaria parasites analysis on blood smears usually comprises four different tasks, as follows:

1. Image preprocessing: the images are normalized in colouration because it can differ a lot from image to image, and the different regions of interest are made the most contrasted possible.
2. Segmentation: red blood cells and parasites are separated from the background and white blood cells by using algorithms based on different characteristics of the cells (e.g., shape, color, texture).
3. Feature extraction: relevant characteristics (e.g., shape, color, texture) are extracted from the different region of interest to train an automatic parasite analyzer.
4. Classification: several classification schemes can be performed. Hierarchically, cells are classified in red blood cells and white blood cells. Afterward, red blood cells are classified in affected by parasite(s) or not. In the end, parasites are classified in their type and life stage. Parasites potentially can also be present outside the cells. In this case, they should need a more specific and dedicated analysis.

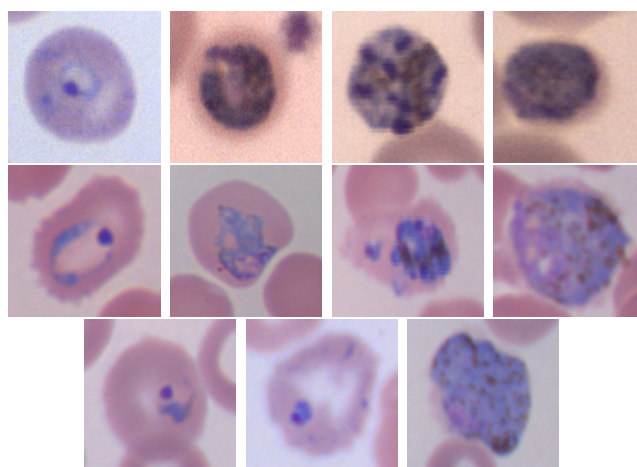


Figure 6.13: Examples of malaria parasite stages. From top left: *P.falciparum* ring, trophozoite, schizont, gametocyte; *P.ovale* ring, trophozoite, schizont, gametocyte; *P.vivax* ring, developed trophozoite, gametocyte. [LDRK18]

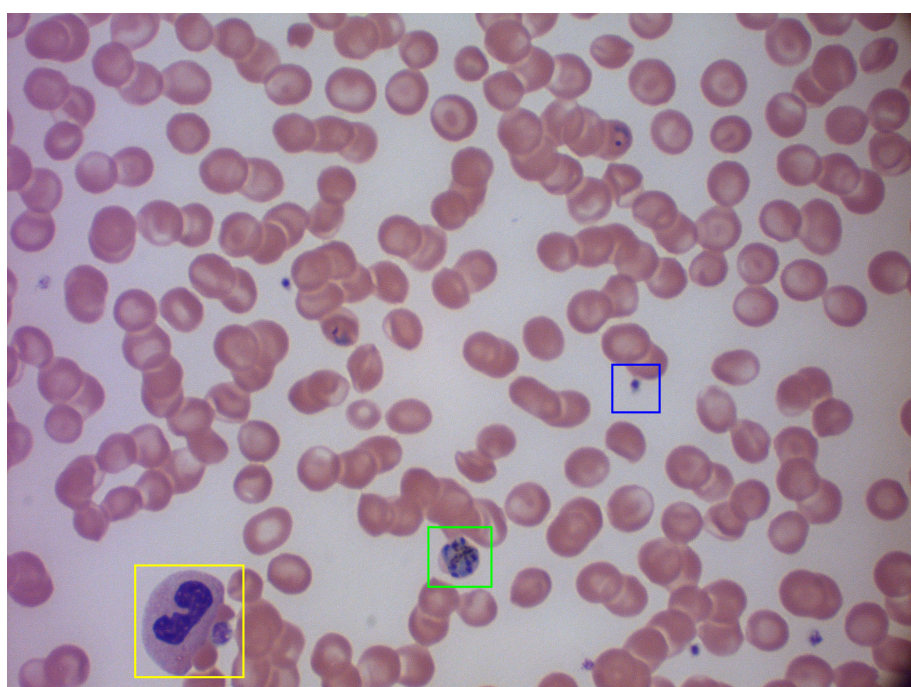


Figure 6.14: Example of blood smear image acquired with a good coloration and illumination scheme. Three different regions of interest characterize the image: an eosinophil granulocyte on the bottom left (yellow bounding box), a schizont Plasmodium Falciparum on bottom center (green bounding box) and the erythrocytes. Please note that some platelets are also present (blue bounding box). Courtesy of CHUV, Lausanne.

Chapter 7

WBCs Segmentation

The main purpose of this thesis was to develop a CAD system able to extract appropriate and useful information from blood cell images, acquired employing microscopes, to easily perform activities on them, like the WBCC. One of the main issues to deal with is certainly the management of the different staining techniques and illumination conditions in which the image can be acquired. Datasets presented for WBC analysis show several examples 6.3.2. All considered, this chapter presents different methods which takes into account these issues and offers solutions to them. Paragraph 7.1 refers to the works [RLP15a], [RLP15b], while paragraph 8.3 refers to the work [PLPD18]. The proposed solution starts with a segmentation step, which is a crucial step in this procedure because its accuracy dramatically affects both the computational performances and the whole system overall accuracy. However, it is also a challenging problem to manage because of the complex nature of the cells, the low resolution of microscopic images and complex scenes, e.g., cells can overlap each other or cells can have different sizes or shapes. On the other hand, the color and contrast between the cells and the background can vary so often according to the standard, inconsistent staining technique, the thickness of smear and illumination. Although standardization is useful to avoid superfluous differences in the features of similar images, a robust segmentation approach can cope with the described issues, and this is undoubtedly one of the main motivations to the realization of this work. State of the art shows that most of the authors proposed traditional methods to perform cells segmentation, like thresholding. In some cases, WBCs counting has been based on detection methods rather than on segmentation ones, by using the circular Hough transform [MLMR13] or texture analysis, even though color image segmentation could also be performed with pixels clustering or classification in color space. Unsupervised and supervised schemes [PLC09], such as k-means and neural networks, have been widely used for this purpose even if there are many disadvantages to deal with. Generally, the biggest problem of an unsupervised clustering scheme is how to determine the number of clusters, which is known as cluster validity. And as for a color image, the selection of color space is quite critical. The supervised scheme needs training. The training set and initialization may affect the

results, and overfitting should be avoided. So a supervised clustering/classification algorithm with right generalization property is most appealing. Our method aims to solve the segmentation problem in a non-linear feature space obtained by kernel methods to overcome the non-linearity of data distribution and the shift/offset of color representing the different regions of interest inside a blood sample: mature erythrocytes, leukocytes nuclei, and cytoplasm. SVM (Support Vector Machines) and ANN (Artificial Neural Network) are machine learning models with excellent performances in classification, but their main drawbacks are that a training phase is necessary to make them work and it could be computationally hard with large datasets. Several authors have proposed methods for effective segmentation of the nucleus of leukocytes, while there are few attempts of segmentation of the cytoplasm. In this chapter, the segmentation techniques used to segment the whole white blood cells will be illustrated. Since during the analysis of the images and the segmentation results many issues have been observed, different approaches have been proposed in order to make further improvement and to obtain better results. Most of the proposed procedures are based on machine learning methods. Although in many cases machine learning methods are not considered computationally suitable for segmentation, here special effort has been devoted to improving this kind of approaches in order to be robust against uneven illumination, local imprecision, different acquisition devices, and staining. They have been mostly chosen because they can provide excellent segmentation results by training with different samples. Efforts have also been made to reduce their computational expensiveness.

7.1 WBC segmentation by samples

As stated before, typically segmentation is a key step in every CAD system. Moreover, it is worth to remember that several regions of interest have different characteristics. Therefore a good segmentation strategy is certainly needed. Further issues addressed are that images are acquired with various acquisition devices and staining techniques. Staining procedures could produce very different blood smears and, consequently, images even though they represent the same scene. Although standardization of the procedures could be useful to avoid excessive differences in the features of similar images, a robust segmentation approach can cope with the described issues. An automatic machine learning approach to performing image segmentation has been realized by following the critical idea that producing a well-trained model, and it is possible to generalize the problem and overcome the issues. As for all the approaches that involve the use of machine learning techniques, a training set is needed in order to create a model or to make a comparison with the unknown samples. ALL-IDB presents two distinct versions, one with regions-complete images and the other with singular leukocytes only. Therefore the strategy is to use a part of this dataset as a training set for the learning by sampling algorithm. Firstly, the images of the training set have been segmented with classic segmentation method

to obtain pure samples related to the regions of white blood cells nucleus and cytoplasm, mature erythrocytes and background. As a comparison, an approach based on three Mean Shift iterations and a ROI-selection method has been realized. The first one aims to smooth the intensity colors of the clustering modes corresponding to the colors of the region of interest, while the second one lets the user choose the most appropriate samples. Moreover, the pixels obtained from these regions have been reduced in number through a Nearest Neighbour Search (NNS) by removing any duplicates or elements with distance next to zero. Then, the training samples have been prepared by adapting sampling from the regions obtained from the classic segmentation phase so as to perform the training process of a multi-class SVM in order to classify all the pixels of a given image correctly. Finally, the SVM is used to segment the image for extracting whole white cells, using a classification phase by means of a model. Since the size of the training set could be controlled and reduced in sampling, SVM training is speedy.

7.1.1 On Mean Shift Technique

Mean Shift technique was originally proposed in 1975 by Fukunaga [FH75], then adapted by Chen [PLC09] and generalized for image analysis purposes. More recently it has been extended to low-level vision problems [FCMG00], including segmentation, adaptive smoothing, and visual tracking. It is used as a non-parametric technique for the estimation of the density gradient in the image analysis field, even if it was developed to perform mode finding on clustering procedures. In contrast to the classic K-means clustering approach, there are neither a priori assumptions about the point distribution nor the number of modes and clusters: the Mean Shift procedure itself computes them. Furthermore, Mean Shift has been adapted to become a very effective image segmentation technique, even if it was born as a clustering method of data analysis. It allows to attenuate shape or color differences between the objects inside the considered images; for these reasons, it works as a local homogenization technique. The objective is to substitute every single pixel value with the mean of the sampled pixel values in a certain neighborhood, within a certain radius R and a certain color distance D . Both of them are usually input defined by the user who generally has a deep knowledge about the context or uses some pre-processing technique to obtain the best values of R and D . Typically, Mean Shift requires at least three basic information to gain the best results; first of all, we have to define a certain kernel, which uses a distance function, to measure the pixel distance in every single iteration of the procedure: examples are the Gaussian kernel and the Epanechnikov kernel. Secondly, it needs two distance values: an R radius and a D color distance. Then, iteratively, the procedure finds the modes of an input given image and calculates new values for every single pixel, according to the chosen kernel function and the distance parameters. It is worth mentioning that the Mean Shift algorithm is not well defined at the boundaries, because it does not consider the non-existent neighbor pixels. Consequently, a strategy to handle

them is necessary. For example, we have studied a padding of the image to process boundary pixels correctly.

7.1.2 Experimental evaluation

This section motivates how a classification method has been used to perform a WBCs segmentation. Support Vector Machine (SVM) has been used to perform a classification of every single pixel belonging to the images to segment, following the indications of the method proposed in [PLC09]. Once Mean Shift has been applied over the training set for producing clustered colored images, as shown in fig. 7.2, in which the classes to which each pixel belongs is immediately clear. We use a part of these images to train the different SVM in the three different strategies following mentioned. As a comparison, we also segment every single dataset image with classic segmentation methods. It is done to execute a more in-depth analysis of our study. The **first strategy** works as a conventional binary SVM classifier. Hence we have exactly two classes in which the pixels will be classified: the positive class includes the white blood cell nuclei and cytoplasm pixels, while the negative class represents pixels belonging to erythrocytes or background. The **second strategy** substantially works like the first one, with the main difference that we exclude from the training samples all the pixels belonging to the cytoplasm, in order to avoid misclassification due to similarities with the lighter region of erythrocytes. The **third strategy** is based on the results obtained with the two previous versions. The classifier needs more valid training samples for cytoplasm only. So, in the last version, we perform a three-class SVM, using both the pixels belonging from WBCs nuclei (class 1) and both pixels belonging to the WBCs cytoplasm (class 2). Thus, pixels belonging to erythrocytes or background are labeled with class 3. Note that for this approach only classic segmentation has been used to produce pure samples for the SVM because Mean Shift segmentation merge both WBC nucleus and cytoplasm. A Mean Shift alteration could be done to adapt it for our purposes, but we have chosen to use classic method for simplicity. Fig. 7.1 shows the segmentation results using the three aforementioned solutions. In the first one, WBCs are exactly recognized and segmented, but the lighter region of erythrocytes is misclassified as WBC one. The second strategy, like the first one, can correctly detect the nucleus even if it fails in detecting the cytoplasm of some WBCs classes. Finally, the third strategy performs a good detection of both nucleus and cytoplasm.

7.1.3 System Implementation

For each strategy, the training set is formed by sampling pixels from the images belonging to the ALL-IDB2 presenting healthy WBCs chosen to make part of the available training images. On the other hand, the test set is formed of the first 33 images of ALL-IDB1, acquired in the same lighting conditions and with the same camera.

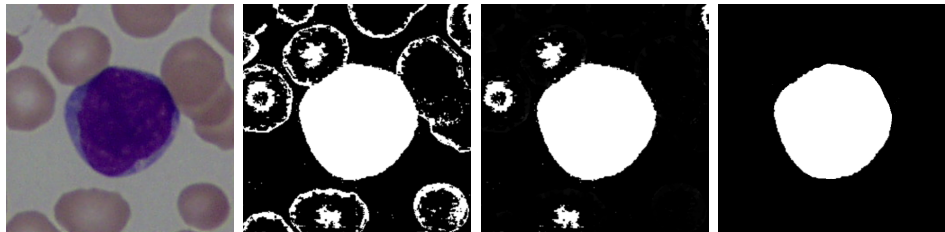


Figure 7.1: From left to right: extracted image from ALL-IDB2, segmentation result for nucleus an cytoplasm with the first strategy, segmentation result for nucleus an cytoplasm with the second strategy; segmentation result for nucleus an cytoplasm with the third strategy. First strategy tends to misclassify lighter pixels belonging to RBCs, that are quite similar to WBC cytoplasm. Second strategy improve the results of the first one and it misclassifies only RBC nuclei, that are quite light. Final strategy gives the expected results by classifying WBCs pixels correctly.

According to the prior knowledge defined about Mean Shift and standard segmentation methods, we have used two strategies to perform the first phase of our algorithm. Both of them are focused on offering the SVM a sufficient set of possible training samples. We have used either standard methods or Mean Shift to obtain this training set. The main objective is to understand which samples represent the most accurate pixels to train an SVM model between Mean Shift and thresholded images. As said before, we have used both the approaches to experiment their behavior concerning the SVM training set building. With thresholding, we have obtained two binary masks. The first one contains the white blood cells segmented in their entirety while the second one contains only the white blood cells nuclei. From these images, the segmented cytoplasm region could be easily obtained performing a difference operation between the first image and the second one and remembering that the cytoplasm region is always placed around the white blood cell nucleus. Thanks to this process we can efficiently perform the SVM training phase. Overall, we have obtained, in both cases, a specific set of images in which the regions have been pointed out. Mean Shift method, instead, produces only a set of images in which the regions of interest are marked with different colors, obtained by finding the dominant color modes of the three main regions: erythrocytes, white blood cell, and background.

At this time, our interest is to perform a proper training phase over the given pixels obtained in phase one. The chosen pixels must be the most various possible all over the regions obtained in phase one, in order to realize a proper classification model during the SVM training phase. The strategy we followed to train the SVM to produce a classification model is now presented. Once we have obtained pixels belonging to the cytoplasm, white blood cell nucleus and red blood cells regions, the remaining step to perform is to accurately choose these pixels with uniform sampling, to consider every single image available in the group of images given for the training

set. Thus, four different regions form candidates of the training set for SVM. We mark nucleus pixels of white blood cells with class label I_1 , cytoplasm pixels with class label I_2 , while mature erythrocyte and non-cell region pixels are marked with I_3 . To avoid uncertainty, the following property has been set: $I_1 \cap I_2 \cap I_3 = \emptyset$ (empty set). SVM implements a classification strategy that exploits a margin-based geometrical criterion rather than a purely statistical criterion. It does not estimate the statistical distributions of classes for classification, while defines the classification model by exploiting the concept of margin maximization. There are two types of margin in SVM. Hard margin classifier works well in no-noise cases but fails with noisy data due to overfitting. Soft margin classifier may achieve much better generalization results by relaxing the hard margin and ignoring the noisy data. So, training can benefit from removing noisy samples from the training; for this reason, we have produced pure samples of the three classes. Statistics theory has revealed that, through uniform, or Monte Carlo sampling, a subset could be produced to approximately represent the entire data set while retaining the distribution of data effectively [Caf98]. The essential steps of this phase can be summarized as follows:

- sample N pixels from I_1, I_2, I_3 regions. There are $N/4$ pixels sampled respectively from four regions (cytoplasm, nucleus, mature erythrocytes, and background region) to keep the size of the training set balanced;
- train an SVM online, taking the reduced training set defined at point one and an RBF kernel and generate a classifier model;
- use this model to classify the image pixels which are represented by $(R, G, B)^T$.

We have performed two main experiments. The first one has been realized to verify our implementation performances over single WBCs and to identify the most suitable parameters for the SVM. Thus, through a ten-fold cross-validation each time we have divided the original training set in two subsets, the first one to train the SVM and the second one to test the obtained model. An ideal average accuracy value has been reached by choosing the parameters c and γ as $1e3$ and $1e1$ respectively. The second and final experiment has been realized to verify the segmentation performances of the proposed method. Thus the whole original training set has been used to create the SVM model. The first 33 native resolution images have been used as a test

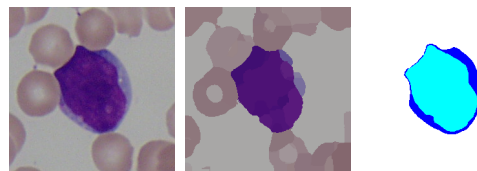


Figure 7.2: Examples of training samples candidates. From left to right: original image from ALL-IDB2, same image after three iteration of Mean Shift algorithm; same image thresholded to emphasize WBC nuclei (light blue) and cytoplasm (blue).

set and to check the method applied to a natural image composed of several white blood cells of many different classes.

Once the first (visual) results have been obtained, we have started experimenting with various features that can be used to train the classifier. Even though we are talking of a segmentation technique, pixels are used as features for the SVM classifier. Until now the only descriptors used are the original RGB color intensity values. Although, in many cases, these features are enough to reach a good segmentation result, in other cases a weak feature set like this is not able to discriminate pixels belonging to regions with wide variations in colors. Thus the first intuition has been to add the average color values of each pixel neighborhood. These average values have been tested for a neighborhood of size 3×3 , 5×5 and 7×7 . For the same neighborhood, we have also computed other statistical features that are often used for segmentation purposes: standard deviation, uniformity, and entropy. While the segmentation accuracy highly benefits from the use of these new features, the overall system became slower, both in training and in segmentation phases. Furthermore, the step of samples selection, used to train the classifier, became too complicated, due to a higher number of samples with different values. For all these reasons the features previously mentioned have been extracted only for a neighborhood of size 3×3 , showing excellent performances as shown in fig. 7.3, outperforming previous results. After the segmentation, all the images have been automatically cleaned, as we have already proposed in [PR13], to remove small artifacts from the background and to give the reader an idea about the goodness of the results. To evaluate the segmentation performances of the proposed method, a subset of images (52 samples) belonging to the ALL-IDB1 have been manually segmented by skilled operators. As stated above, the entire WBCs, the entire RBCs, WBCs nuclei and WBCs cytoplasm are available as separate ground truth images. Fig. 7.3 shows some images belonging to the ALL-IDB1 and their relative ground-truth images. Finally, the ground-truth images previously described have been compared with the automated segmented images in order to calculate the most common metrics for segmentation evaluation, that are: accuracy, sensitivity, specificity, precision and F-measure. Our segmentation approach has been compared with some well known segmentation algorithms like Otsu [Ots75] and Zack [ZRL77]. Table 7.1 shows the average performances obtained 52 samples They adequately represent the different staining and

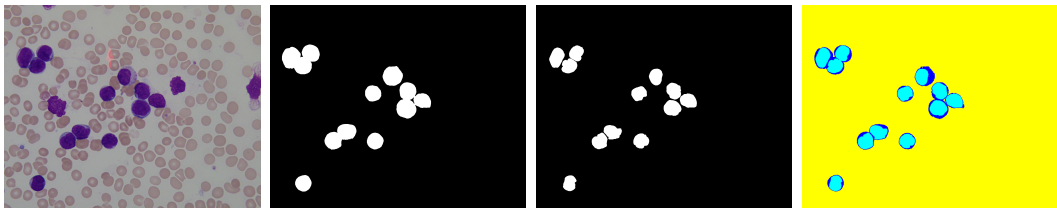


Figure 7.3: Original images from the ALL-IDB1 database, ground-truth for whole leukocyte, ground-truth for leukocyte nuclei and final segmentation result.

illuminations available in ALL-IDB. As it can be seen the most important values obtained with our approach are higher than the other segmentation approaches.

Table 7.1: Segmentation performances.

	Otsu	Zack	Our Approach
Accuracy	77.67 ± 0.6	74.76 ± 3.6	97.61 ± 1.7
Sensitivity	76.70 ± 8.3	85.43 ± 6.8	98.45 ± 0.3
Specificity	85.62 ± 4.6	81.27 ± 5.4	97.56 ± 1.2
Precision	53.55 ± 12.8	79.12 ± 8.6	70.45 ± 5.8
F-measure	45.18 ± 5.3	55.15 ± 3.3	82.13 ± 2.3

7.1.4 System extension

This segmentation solution has been developed following the idea described in section 7.1.2. The same settings have been maintained, from the dataset to materials. The only thing that differs is that classic segmentation method has been used to obtain pure samples related to the regions of white blood cells nucleus and cytoplasm, mature erythrocytes and background, instead of Mean Shift technique. The pixels obtained from these regions have been reduced in number through a Nearest Neighbour Search (NNS) by removing any duplicates or elements with distance next to zero. Even in this case, SVM has been chosen due to the excellent results so far produced. Once the manually segmented images have been obtained from the training set, we used a subset of these images to train the SVM. In particular, in this version we performed a three-class SVM, using both the pixels belonging from WBCs nuclei (class 1) and both pixels belonging to the WBCs cytoplasm (class 2). Thus, pixels belonging to erythrocytes or background are labeled with class 3. It is well known that getting manually segmented images is neither simple nor cheap. Considering that, we perform an experiment which can be applied to every peripheral blood images dataset, even in each illumination condition and with different combinations of cameras and microscopes. This method is based on ROI (Region of Interest) selection. Thus, making use of a few original images, the object of interest (WBCs) could be selected and used as a positive example for our multiple-class classifier. Considering that it is a segmentation method based on classifiers, negative instances are needed. Therefore, the background region, that comprises red blood cells and plasma must be selected. An example of ROI selection for positive and negative example is showed in Fig. 7.4.

Naturally, the negative samples must not contain any WBC. In fact, in this case, the NNS has performed also over pixels belonging from a different region, to avoid errors committed during the ROI selection and to remove pixels with close values. In this way, the obtained training set certainly present uniformly distributed pixel values. Note that with this approach the WBC cytoplasm and nucleus are managed

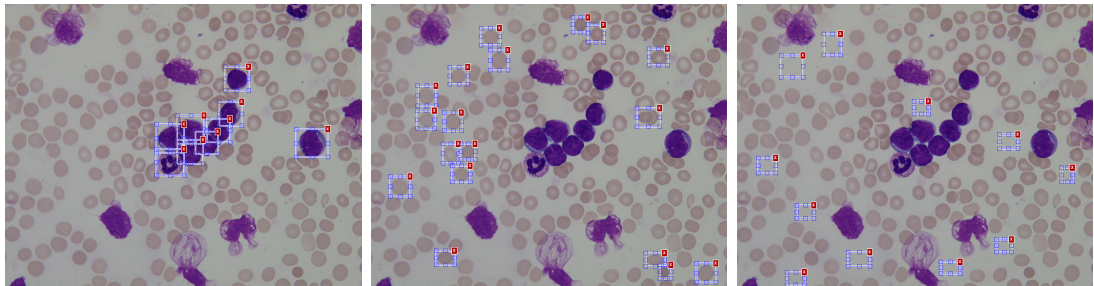


Figure 7.4: Examples of ROI selection for WBCs, RBCs and plasma.

as a unique region, both because the ROI selection is not so suitable for adjacent regions and both because they can be easily separated in a further step by using a simple threshold. Differently, from other approaches, we are now able to take also RBCs into account, considering them as a different class, as explained in 9.1.

7.2 Discussion

This chapter illustrated the segmentation techniques used to segment white blood cells. It has been observed how the results could be influenced by the presence of different lighting condition and especially by the presence of uneven lighting within the same image. Just for this reason, a machine learning approach has been chosen, to take into account the uncertainty present in the image itself and at the same time to address the problems of local light variations. This method uses the SVM, a machine learning technique providing extreme flexibility, both because it is possible to make use of different types of kernel and both because it is possible to define a hyperplane for separating classes which guarantees a certain tolerance with respect to noise. Some visual results have been showed for each of the proposed approaches, and finally, the most common metrics for segmentation evaluation have been computed and compared with the results obtained with some well known segmentation algorithms. Making a comparison with the state-of-the-art is not easy since no public ground truth images for segmentation experiments are available. So, each author that proposed a new segmentation approach tested his method with manually segmented ground truth images. Thus a direct comparison is not possible, but an overall idea of the segmentation performances can be made by comparing the approaches that used ALL-IDB. As a comparison, the method proposed in [RSBK14], that uses a k-means clustering, obtained an average accuracy of 85%, while the method proposed in [AK13] that uses a rectangular detection using Gray Level Co-occurrence Matrix to firstly find the region containing the WBCs later segmented with a reshaping procedure on the region detected achieved an overall accuracy of 91%. Again, the method proposed in [KAG13], that uses a vector quantization technique to segment the white blood cells, obtains an accuracy

of 92%. As it can be seen the results obtained with the SVM approach outperforms the state-of-the-art, with an average accuracy of 97.6%. It must also be noted that most of the algorithms proposed in the literature are focused only on WBCs segmentation. Thus none of them performs a whole segmentation of peripheral blood images. Although the accuracy of these methods can be already considered excellent, a further approach has been proposed, to improve them and to directly face the problem of clumped cells analysis. On the other hand, the VFC detection method is more oriented to clumped cells separation rather than on pure segmentation. It works by following only their natural shape even if they are hard to distinguish. Its strength lies in the invariance to cells shapes and, by using the gradients movement, it can find the edge shape even if this is not immediately visible. Moreover, the proposed algorithm is not tuned to a specific training set, and it could be used for whichever peripheral blood images dataset. Experimental results demonstrate that this new approach is very accurate and robust for detection, if compared to some traditional methods, being able to obtain excellent results with the three public tested datasets, even though some improvements could be implemented.

Chapter 8

WBCs Identification and Counting

A further problem in peripheral blood cells image analysis is certainly the presence of adjacent cells or, even worse, cells grouped or clumped together, like the typical leukocyte agglomerates. An example is shown in Fig. 6.5. Cells clumps can be wrongly identified as single cells and then misclassified, by segmentation strategies, considering that all the shape descriptors belonging to these regions are misleading. This chapter presents an analysis of this phase, which is crucial to detect and separate leukocyte agglomerates. Finally, the single leukocytes can be decomposed and segmented into their components: nucleus and cytoplasm. This process can be summarised in the following basic steps:

- Agglomerates identification
- WBCs separation
- Image cleaning

8.1 Agglomerates Identification

Once the segmented image has been obtained, it is essential to find a suitable method to identify the cells agglomerates. As mentioned earlier, many authors used the a priori knowledge about the typical size and shape of the cells, assuming that only cells agglomerates should present a bigger size than the average leukocytes size. Unfortunately, this assumption is respected only for images acquired with the same camera resolution and the same microscope magnification, and the main issue remains the limit to the usefulness of these approaches to a single dataset, or even a few sets of images. The main goal here is to find an approach able to identify leukocytes agglomerates on different sets of images correctly. It requires the use of one or more descriptors to analyze every region directly. Many shape descriptors could be used to verify if a region is a single cell or an agglomerate [GW07] but, knowing that a WBC is typically round-shaped, an analysis of the

region roundness could be useful to localize the agglomerates. The roundness (4.5) is a measure of circularity (area-to-perimeter ratio) that is relatively insensitive to irregular boundaries and its value is equal to 1 for a circular object and is less than 1 for an object that departs from circularity. The experimentations showed that this descriptor is useful in shape discrimination and that a roundness value lower than 0.80 indicates the presence of leukocytes agglomerates. The roundness value is computed for each connected component of the segmented images and using the threshold mentioned above value, two different images have been created (Fig. 8.1). The first one contains only single leukocytes, and thus it proceeds directly to the next step of the process, while the second one contains only grouped leukocytes and thus it proceeds with the WBCs separation process. It is important to note that in some cases the second image may be empty and so the phase of WBCs separation does not take place.

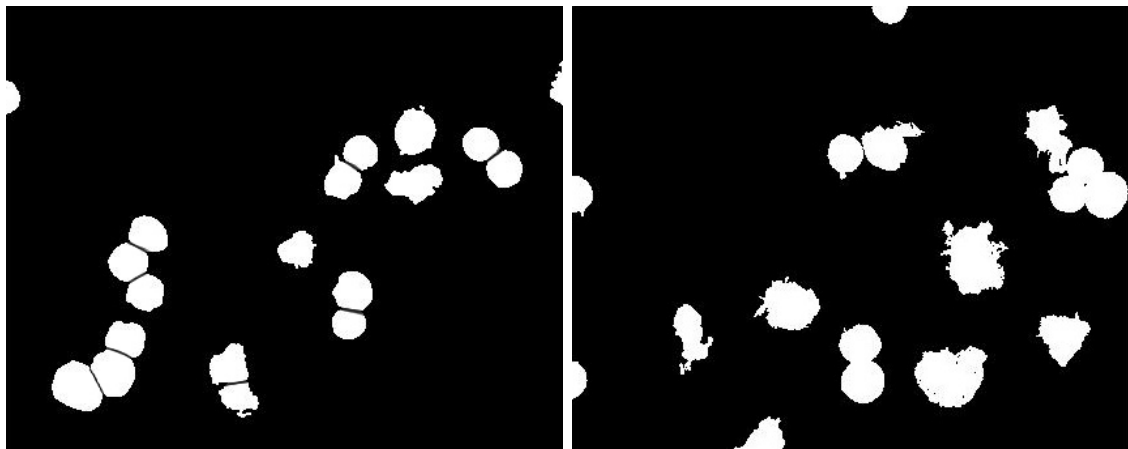


Figure 8.1: Examples of leukocytes identified as grouped.

8.2 WBCs detection and separation from agglomerates

The clumped cells separation is a crucial step in peripheral blood cells analysis, as a precise separation allows extraction of more significant features and a correct count. As previously mentioned, this step has been faced by other authors in two different ways. The first one consists in analyzing the regions of interest in the original image, while the second one is based on the analysis of the segmented image, converted to binary. We proposed two different approaches to operate WBCs clumps separation. The first one is a detection approach based on a modified version of the Hough Transform in such a way that it can analyze circular shapes. It takes the name of Circular Hough Transform (CHT), while the second one makes use of Vector Field Convolution and mathematical morphology techniques.

8.2.1 WBC detection with CHT

The segmentation via SVM 7.1 produces a labeled image, with a different label for every image component. A binary mask containing only WBCs can be easily extracted and used for a first analysis. The analysis starts by extracting all the connected components from the binary mask that we highlight in Fig. 8.2 by drawing a bounding box around them. As it can be seen from the first image, both single cells and clumped cells are detected in this phase. Each connected component just extracted is firstly compared in size and shape with the reference value that we extracted from the training samples. Such reference values are the *solidity* (4.7), determined from the average solidity of all the leukocyte in the training samples, and the area determined from the biggest leukocyte in the training samples. The area value is used to distinguish all the irregular cells sizes caused by the presence of cells agglomerates. The solidity value, on the other hand, is used to discriminate the abnormal components, with an irregular boundary or containing holes but even to exclude dye artifacts, while the *convex_area* is the area of the object's convex hull. Since it is already possible to operate only on cells agglomerate, the use of the whole image is no more necessary. Therefore, we perform a crop of the original image for each region containing the agglomerates, using the previously computed bounding box. At this point, we know the position of the agglomerates but, also, the specific regions to work on. Thus we can use the segmentation result again to delete all regions within the sub-images that are not leukocytes. To entirely preserve the leukocytes edges the binary image containing the segmentation result has been enhanced by a morphological closing operation, excluding small holes inside the regions but also enhancing the contour of the cell. In this way, the resulting image is spotless, presenting only the leukocyte agglomerate on a dark background. Since our ultimate goal is to provide a cell count, rather than a real separation of cells, in this case, we have preferred to speed up the process by realizing a pure detection phase based on the knowledge extracted from the cells forming the training set. The detection has been performed with the circular Hough Transform, being the most suitable for the recognition of circular shape, in particular, if the range of the radii values is already known, as in our case. If the range of the possible radii is small, the detection is faster, but we are more interested in detecting all the leukocytes. Thus the radii of the smallest leukocyte decreased of a factor of 0.9, has been chosen as minimum radius value. On the other hand, the radii of the biggest leukocyte have been chosen as maximum radius value increased of 1.1 factor. Both values have been taken from the training samples. The algorithm of the circular Hough transform is based on the gradient field of the image, that performs a threshold in a measure of the 5% of the maximum intensity value, so ignoring all the pixels with gradient magnitudes smaller than the threshold. Thanks to it, false detection, due to the presence of small values of the gradient magnitude, is avoided. A qualitative evaluation of the whole step of separation and counting is shown in Fig. 8.2. As it can be seen the detection phase is excellent, also with the presence of agglomerates

with a high number of cells. The counting now becomes easy, because it is only necessary to count the detected circles in each sub-image plus the single leukocytes detected in the previous phase.

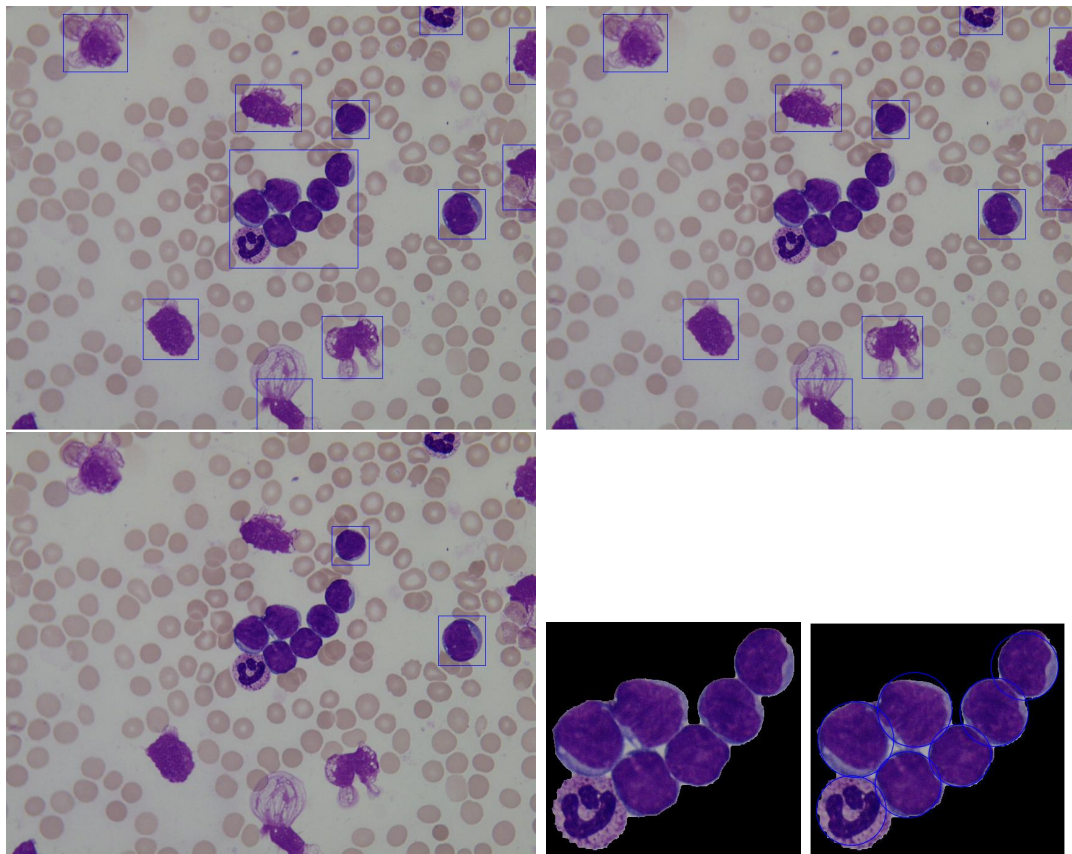


Figure 8.2: Leukocyte detection phases: connected components, single objects detection, artifact removal, agglomerates crop and detected leukocytes.

To further highlight the importance of each phase of the proposed method, we show in Fig. 8.3 how the Hough transform performs on some original blood sample images, without the use of any regions crop and in particular, in the first case without any knowledge about the size of the leukocytes and in the second case without any knowledge about the grey levels. In both cases the results are really unsatisfactory, since many little circles have been drawn over bigger leukocytes or worst many circles have been drawn on areas that do not contain any leukocyte.

8.2.2 WBC separation from clumps with VFC

A real cells separation from clumps can be performed, on the other hand, by using the following method, based on Vector Field Convolution.

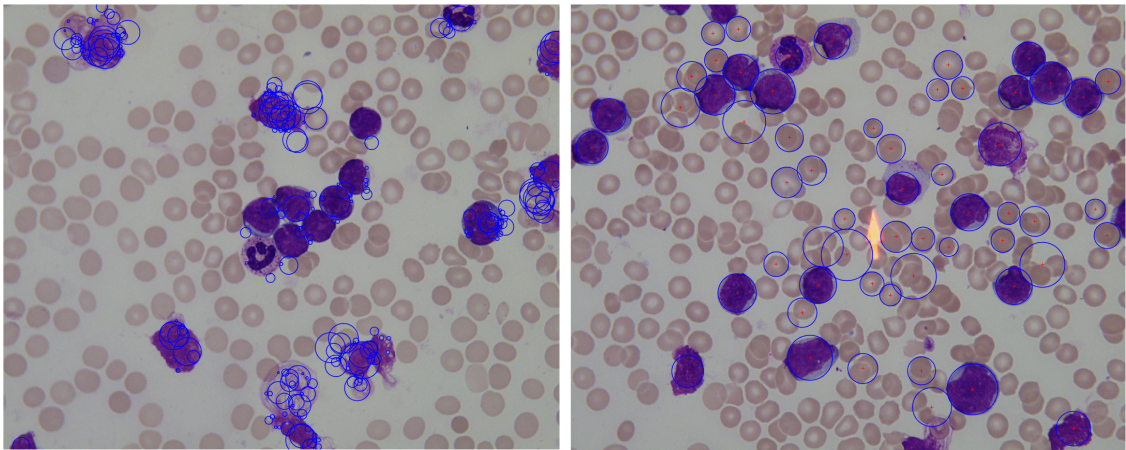


Figure 8.3: Application of circular Hough transform to the whole image using an unknown radius and a wrong threshold.

8.3 WBC detection with VFC

Although the segmentation results of the schema based on segmentation by sampling 7.1 has been very promising for the realization of an automatic cells analysis framework, a further WBC analysis method, based on Vector Field Convolution (VFC), has been investigated and implemented. The primary targets of this improvement are to segment all the WBCs nuclei with VFC strategy and to divide potential clumps by using an analysis of the real cells boundaries, overcoming the use of classic methods, like Watershed transform, for example. The system is composed of the following phases: pre-processing, binary edge map generation, VFC [BS07] application, grades transformation, external energy computation, black and white distance calculation and, finally, skeletonizing and region merging application. The method starts with a contrast stretching on the RGB color space's G channel, as shown in fig. 8.4. The regions boundaries are extracted employing a gradient operator which permits to obtain a binary edge map. Subsequently, the VFC is computed with the initialization of the kernel vector field and the edge map creation. A first WBCs detection has been so far obtained with the previous steps, and a first nuclei segmentation can be consequently obtained by applying the skeleton function on the overlapping between the external force and the binary distance transform images. The final segmentation result is described in detail further on.

8.3.1 On Vector Field Convolution

An external force, namely the VFC, can be obtained by convolving a vector field with the edge map derived from the image [BS07]. Active contours using the VFC external force are called VFC snakes. Differently, from the GVF [XP98] snakes, that are formulated using the standard energy minimization framework, VFC snakes are

constructed from a state of equilibrium between the forces. Furthermore, VFC snakes have many advantages, e.g., a wide capture range. They can grab the concavities. They are better resistant to noise images. They can adapt the force field and reduce the computational cost drastically. The proposed segmentation technique starts with a histogram stretching. In particular, WBCs nuclei have been highlighted by stretching RGB color space's G channel (Figure 8.4). The purpose is to obtain only the cells of interest to create the best possible edge map.

The high spatial frequency regions, corresponding to the edges, have been highlighted thanks to the Sobel operator. It is a kind of orthogonal gradient operator, and it has the advantage to produce a smoothing effect on the image's random noise [SF68]. Gradient corresponds to the first derivative. Therefore gradient operators are derivative. For a continuous function $f(x, y)$, in the position (x, y) , its gradient can be expressed as a vector:

$$\nabla f(x, y) = [G_x \quad G_y]^T = \begin{bmatrix} \frac{\delta f}{\delta x} & \frac{\delta f}{\delta y} \end{bmatrix} \quad (8.1)$$

This operator applies two kernels in the two principal directions. Calling G_x and G_y the horizontal and vertical derivative approximations and I the image, the computation is described as follows:

$$G_x = \begin{pmatrix} +1 & 0 & -1 \\ +2 & 0 & -2 \\ +1 & 0 & -1 \end{pmatrix} \times I \quad (8.2)$$

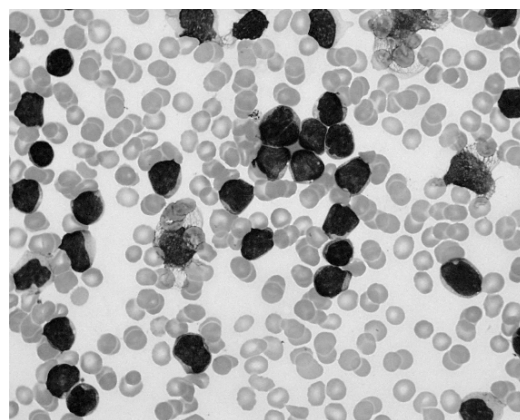


Figure 8.4: RBC image's G channel extraction. The WBCs are highlighted with respect to the other regions.

$$G_y = \begin{pmatrix} +1 & +2 & +1 \\ 0 & 0 & 0 \\ -1 & -2 & -1 \end{pmatrix} \times I \quad (8.3)$$

where the \times operator indicates the convolution operation.

Before going into detail, it is useful to define the Vector Field Kernel (VFK). It is computed using the following equation:

$$k(x, y) = m(x, y)n(x, y) \quad (8.4)$$

where n is the unit vector that points to the origin of the kernel

$$n(x, y) = \left[\frac{-x}{r}, \frac{-y}{r} \right] \quad (8.5)$$

and m is the magnitude of the vector. Potentially, every single pixel in an image may be attracted to the edge of its region [BS07]. This fact could be compared to the gravity effect on every single object in Earth: it is attracted towards the Earth surface. Consequently, if we consider the origin as the point of interest, VFK has the desirable property that a free particle placed in the vectorial field is able to move to a point of interest. The external force that works in the VFC is defined in this way:

$$f_{vfc}(x, y) = u_{vfc}(x, y), v_{vfc}(x, y) \quad (8.6)$$

Since the edge map is non-negative and wider near the edges of the image, the VFC acts more on the edges than to homogeneous regions. Therefore, the free particles of homogeneous regions will be attracted to the edges. If we use a complex-valued range, the VFC acts as a filter on the edge map, which does not depend on the origin of the kernel. The VFC field highly depends on the magnitude of the VFK in such a way that it is directly proportional to the $VFK(x, y)$. The farther is the figure of interest (FOI) [BS07], the less powerful is the force and, therefore, the magnitude must be expressed as a positive function that decreases with respect to the distance of the origin. Two types of magnitude functions are defined as follows:

$$m_1(x, y) = (r + \epsilon)^{-\gamma} \quad (8.7)$$

$$m_2(x, y) = \exp(-r^2 \zeta^2) \quad (8.8)$$

where γ and ζ are positive parameters to control the decrease rate, ϵ is a small positive constant which prevents division by zero at the origin, while $m_1(x, y)$ is inspired by Newton's universal gravitation law. Furthermore, the pixels in the edge map can be considered as objects of mass proportional to the strength of the edges and the VFC would be the gravitational field generated by all objects. $m_2(x, y)$ is a Gaussian shape function, and ζ can be viewed as the standard deviation. The influence of FOI is strongly dependent from γ and ζ because it increases if the first one decreases or the second one increases. In general, the influence of FOI should

be increased (or decreased) as the signal-to-noise ratio is decreased (or increased) [BS07].

The VFC uses the two components of the external force $u_{vfc}(x, y), v_{vfc}(x, y)$ to describe the field of the image and its magnitude. These two components are very useful to describe all the edges, both from single leukocytes and from cell clumps. VFC's right and left components can be computed as follows:

$$u_{vfc} = \text{ExtF}(x) / \sqrt{\text{ExtF}(x)^2 + \text{ExtF}(y)^2} \quad (8.9)$$

$$v_{vfc} = \text{ExtF}(y) / \sqrt{\text{ExtF}(x)^2 + \text{ExtF}(y)^2} \quad (8.10)$$

where ExtF is the External force of the Field. u and v are two intensity images with values range in $-pi$ and $+pi$. They need to be combined and converted in degrees values so that the orientation of every image pixel can be described, as shown in Fig. 8.5.

VFC application typically generates some artifacts and this method applies the distance transform to delete them all. It assigns a number that is the distance between each pixel and the nearest non-zero pixel of the image. As a result, the entropy of the image is reduced as well as the noise even though it does not distinguishes if the edge is an RBC's edge or a WBC's edge. As a consequence, the application of the External Energy is needed to overcome this problem.

For an image $I(x, y)$ the general formulation of the image Energy is:

$$E_{image} = w_{line}E_{line} + w_{edge}E_{edge} + w_{term}E_{term} \quad (8.11)$$

where $w_{line}, w_{edge}, w_{term}$ are weights of the features.

Line functional: the line functional, also known as the image intensity, is the attracted value of the dark lines to the light lines. It is possible to choose this value by selecting a positive or negative value of the force

$$E_{line} = \text{filter}(I(x, y)) \quad (8.12)$$

Edge functional: The edge functional bases its work on the image gradient.

$$E_{edge} = -|\nabla I(x, y)|^2 \quad (8.13)$$

This formula defines the strategy by which the method gets rid of the local minima that are not objects of interest. The energy functional using scale space continuation is

$$E_{edge} = -|G_\sigma \times \nabla^2 I|^2 \quad (8.14)$$

where G_σ is a Gaussian function with standard deviation σ .

Termination functional: The lines curvature in an image is used to detect corners and terminations. Put

$$C(x, y) = G_\sigma \times I(x, y) \quad (8.15)$$

we derive a gradient angle

$$\theta = \arctan \left(\frac{C_y}{C_x} \right), \quad (8.16)$$

the unit vectors that move along the gradient direction

$$n = (\cos \theta, \sin \theta), \quad (8.17)$$

and the unit vectors perpendicular to the gradient direction.

$$n_{\perp} = (-\sin \theta, \cos \theta). \quad (8.18)$$

Starting from the previous formulas, the termination functional of energy can be defined as follows:

$$\begin{aligned} E_{term} &= \frac{\partial \theta}{\partial n_{\perp}} = \frac{\partial^2 C / \partial^2 n_{\perp}}{\partial C / \partial n} = \\ &\Rightarrow \frac{C_{yy} C_x^2 - 2C_{xy} C_x C_y + C_{xx} C_y^2}{(C_x^2 + C_y^2)^{3/2}} \end{aligned} \quad (8.19)$$

External energy result: As stated before, a median filter has been employed in order to delete all the regular part of the image and to highlight the edges. It searches the 13th element of the 5 × 5 mask (Figure 8.5).

Once the median filter has been applied over the gradient image, an AND operation between it and the edges regions image so that we can highlight the points which result to be in overlay (Figure 8.5).

The image obtained from the VFC application contains only the WBCs edges that, in some regions of the image, are far from being a connected boundary. Thus, a further method is needed to link the edges preserving the original boundary of the objects. This phase includes different steps. The first one consists in connecting every single white point to the nearest one to produce a connected boundary. A dilation with a 6 size diamond structural element is applied in order to dilate all white dots. Secondly, the opening of the closing is applied with a 4 and 3 size disks, respectively. Then, the skeleton function is performed. It produces an image that contains some spurious branches which are redundant for our purposes and, consequently, we realized the following strategy to get rid of them. To solve this problem we used a path analyzer that checks for the presence of open paths. Indeed, a connected border is a closed path in which a pixel of that border is at the same time a starting and ending point. So, each pixel that does not belong to a closed path is removed. At this moment, every real edge belonging to the cells is available, but over-segmentation could occur so that we need to perform an arithmetical operation which fills all the WBCs edges and removes the others. This operation uses a mask obtained from the external force image. Finally, the application of an opening on the edge map with a 6 pixels radius disk structural element and its addition to WBCs

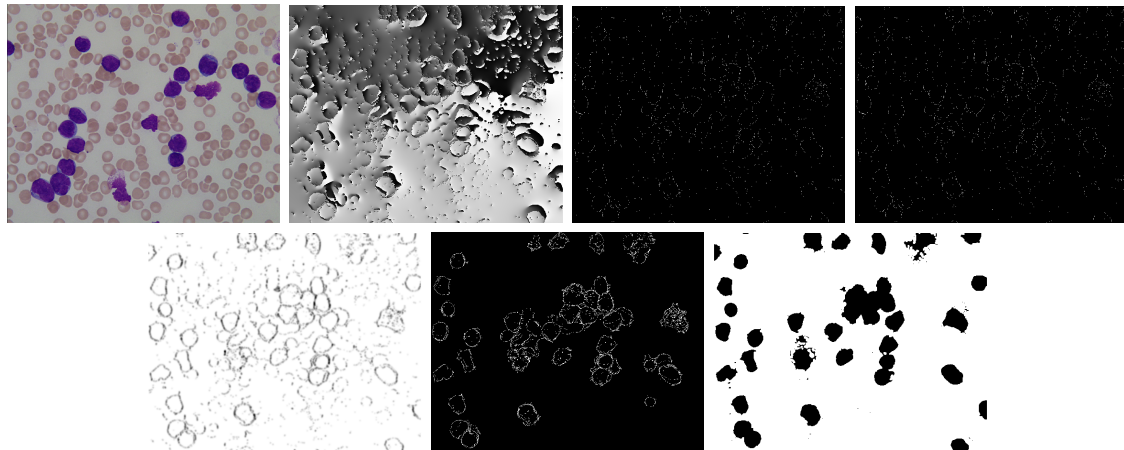


Figure 8.5: Example of VFC detection procedure. Top, from left to right: original image, VFC right component, VFC left component, distance transform image. Bottom, from left to right: external energy image, overlay image and opened image.

image in the foreground, all connected components, fitting into a specific area range, are successfully extracted, as shown in fig. 8.5.

Once the cleaned binary mask has been obtained, we should be able to perform the count of the cells inside the image. Unfortunately, as it can be observed in Figure 8.5, using the proposed method also some WBCs have been separated in two or more regions, so far hampering a correct cell counting.

Thus, it is necessary a further step that merges all the image regions belonging to the same cell. To understand which are the regions that should be part of a single cell, we analyzed the cell area. All the regions that have an area smaller than the half of the most significant region inside the image are considered part of a single

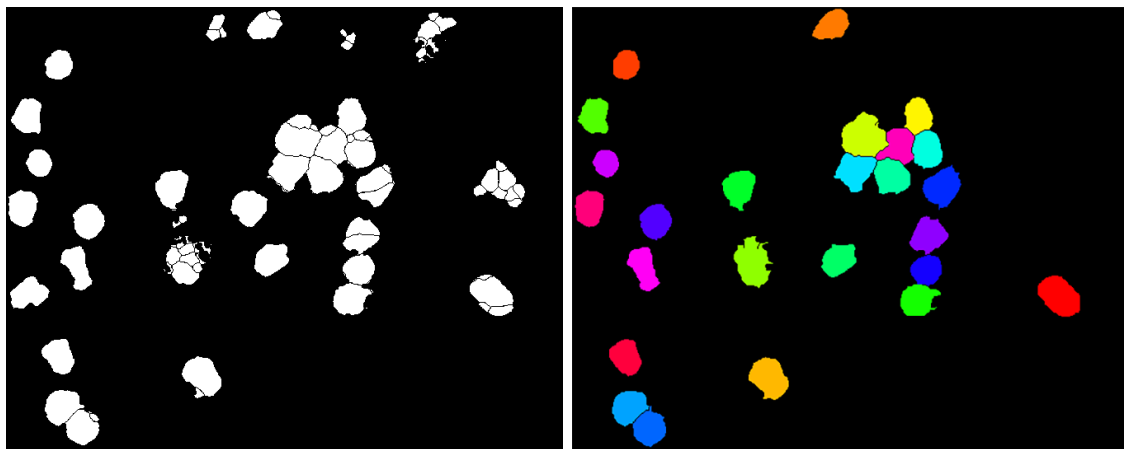


Figure 8.6: Application of complete VFC-based pipeline. Left: oversegmented image, right: final result, all WBCs are split.

cell, while the other regions are considered complete cells. Keeping in mind that smaller area regions belong to larger area regions, we need to identify which of the first ones belongs to the latter. The threshold area used to create these two different images is exactly half of the image's biggest region area. Labeling each area and computing all the centroids, we can know which areas need to be joined together, using the Euclidean distance formula. Finally, it is possible to isolate the two areas and merge them using a closing procedure with a 7 pixels radius disk element. The final result is given by an overlay of this step to the over-segmented image employing the union operator (figure 8.6).

8.4 Image Cleaning

Before being able to count the leukocytes a last step is necessary. Indeed not all the objects can be considered but only the object that are real leukocytes and only those leukocytes completely enclosed in the image. This is necessary in order to prevent errors in the later stages of the analysis process. Deleting the leukocytes that are not completely enclosed in the image is an easy task, since it can be completed by a search of the element touching the border of the image.

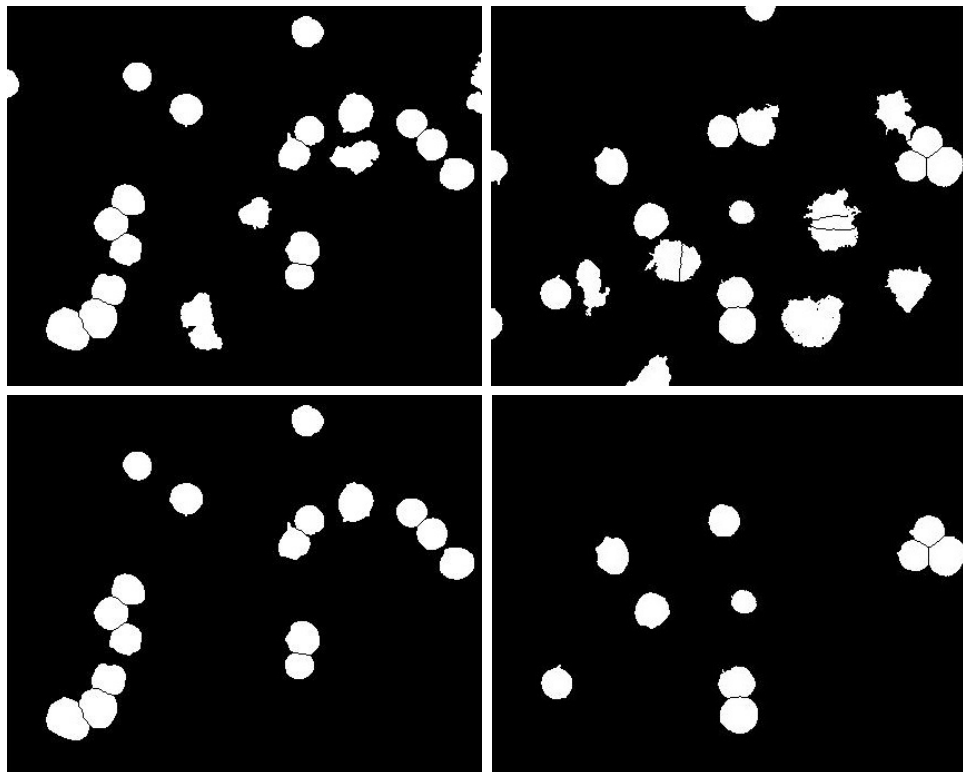


Figure 8.7: Final separation results and image cleaning results.

With this procedure, many WBCs are lost, but it ensures that only those cells

that can be analyzed accurately pass to the next step. The removal of abnormal components instead is a more complex task. Also, in this case, it is important to find a good method to identify the abnormal cells, and as mentioned earlier no assumption about the typical size or shape of the cells can be made based on previous knowledge. Since the size is discriminatory for WBCs, the area is computed for each object in the image, in order to have a reference value, that is the average area. The average area is useful to determine the presence of objects with irregular size. For example, a tiny area might indicate the presence of an artifact that was not removed. Alternatively, a huge area may indicate the presence of adjacent leukocytes that were not adequately separated. Thus a reference range value for the area has been established to remove all these anomalies, preserving only those objects for which $0.8 * \text{avg_area} \leq \text{area} \leq 1.2 * \text{avg_area}$. Unfortunately, abnormal objects could present a size close to the reference value and thus can bypass this check. Typically, this object is WBCs that have been altered by the staining process, so they don't present the typical morphology even a separated nucleus and cytoplasm. Area is used in combination with another shape descriptor that is the *solidity* (4.7). This descriptor measures the density of an object. A solidity value of 1 signifies a solid object while a value less than 1 signifies an object with an irregular boundary or containing holes. The reference value for solidity is again computed by averaging the solidity value of all the objects in the image, when present in a number greater than 5, otherwise a default value is used. During the experimentation, it has been observed that a solidity value lower than 0.90 can adequately discriminate abnormal components. Fig. 8.8 shows some results after border cleaning and the removal of abnormal components. To better highlight the performance of segmentation and separation of leukocyte agglomerates Fig. 8.9 also shows some results after these two main steps on different images belonging to ALL-IDB1, superimposing the segmented leukocyte borders on the original images. As it can be seen, although the images are different between them, both concerning resolution and colors, the results are exact.

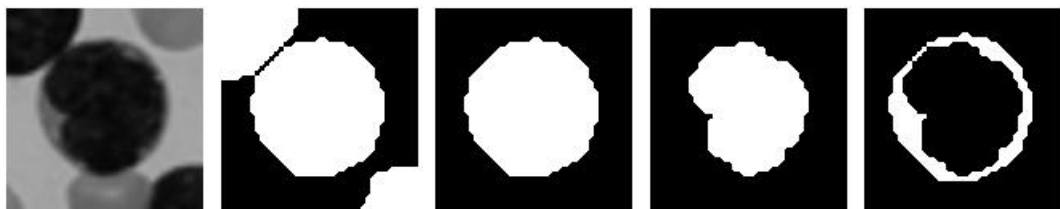


Figure 8.8: Left to right: grey level sub-image, binary sub-image, whole leukocyte sub-image, nucleus sub-image and cytoplasm sub-image.

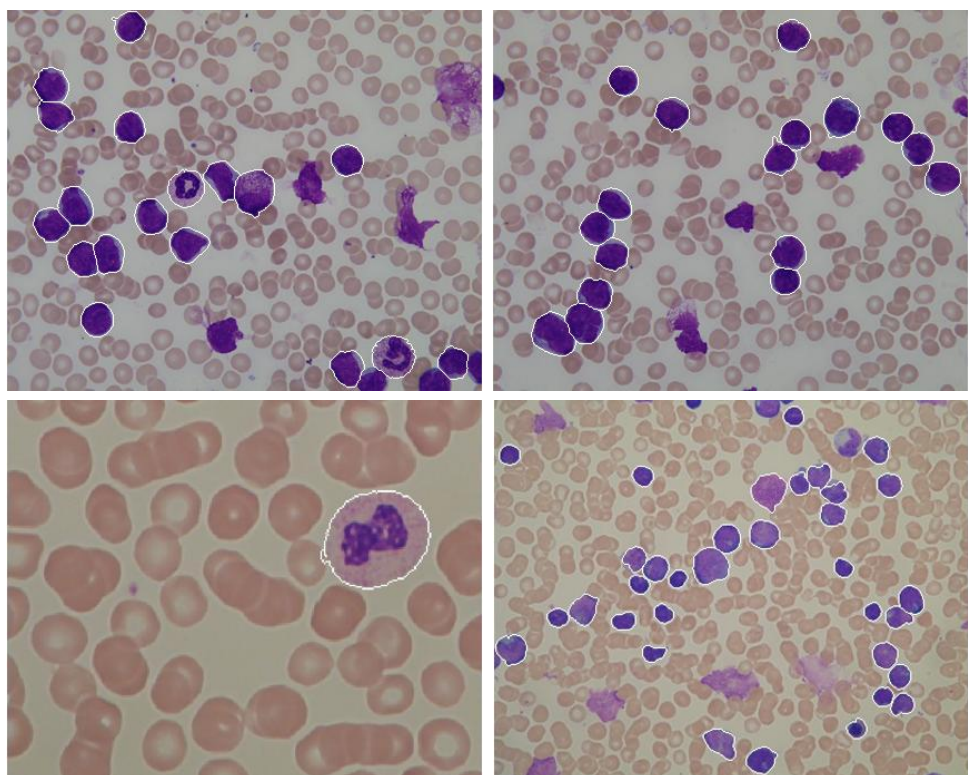


Figure 8.9: Original images superimposed with the contours of the leukocytes identified.

8.5 WBC Count

To evaluate the performances in counting, we have used some public datasets. The ground truth for all the images has been determined by an expert and used to validate the proposed method. As literature proposed we evaluated the counting performances using *precision*, *recall*, *F-measure* and then we added a fourth metric that is the False Negative Rate *FNR*, to highlight when the algorithm is not able to detect a cell present in the image. The whole results for WBCs counting are reported in Table 8.6, more precisely the method based on CHT takes the name of "Det1", while the one based on VFC is "Det2", where they have been directly compared with the results obtained by other authors that used at least one of the three image datasets. As it can be seen, the first approach correctly identified 99.2% of the whole leukocytes of ALL-IDB1 dataset, while using the IUMS-IDB and the SMC-IDB it correctly identified 100% of the whole leukocytes. The performance of the second approach for WBC counting are also reported in detail in Table 8.6 where it is shown that it correctly identified 100% of the whole leukocytes of all datasets. These results have been obtained because ALL-IDB1 presents many complex images, with many leukocytes and different agglomerates, while IUMS-IDB and SMC-IDB present more straightforward images with few leukocytes per image and only a few pure agglomerates. Through a numerical comparison, it is possible to observe that our approaches outperform the detection methods existing in the literature. In particular, they both outperform other methods [MLMR13, ASAFAO14], both because in our implementations we analyzed the grey level image and because with the proposed segmentation we can exclude all the other image regions before the detection phase, and thus considering only portions of the image containing leukocytes. Indeed, the proposed approach does not produce any false positive, being able to exclude all the other image regions before the detection phase, and thus considering only portions of the image containing leukocytes. We have also achieved better performances than another analyzed method [PCR14] that used the watershed algorithm applied on the distance transform. It is mainly due to the fact that watershed transform can obtain good results only in the presence of small agglomerates of cells. Moreover, it requires a perfect segmentation since it works directly on the binary images, therefore the presence of holes or other artifacts could affect the separation among cells and the number of cells detected. Finally, it is important to note that no one author used more than one dataset for the experiments, because all the methods present in the literature are based on a segmentation step that is dataset-dependent and that very realistically fails with different ones.

8.6 Discussion

In this chapter, the identification, separation, and counting of white blood cells have been illustrated. They can be applied to support some existing medical methods, like

	[MLMR13]	[AK13]	[PCR14]	[ASAZAO14]	Det 1			Det 2		
	ALL	ALL	ALL	ALL	ALL	IUMS	SMC	ALL	IUMS	SMC
FNR	-	-	-	1.5%	0.7%	0%	0%	0%	0%	0%
Precision	-	-	-	90%	100%	100%	100%	100%	100%	100%
Recall	81%	88%	92%	98%	99.2%	100%	100%	100%	100%	100%

Table 8.1: Detection performances of proposed WBC count methods compared with the state-of-the-art. Please note that "Det 1" stands for the method based on CHT and "Det 2" for the one based on VFC. ALL, IUMS and SMC are contraction of ALL-IDB, IUMS-IDB and SMC-IDB, respectively.

the White Blood Cells Counting (WBCC). After the segmentation phase, described in detail in chapter 7, the image requires an analysis in order to detect agglomerates, that present an abnormal shape and size. The agglomerates are then analyzed in two different ways, according to the specific needs. If the segmentation has been realized with a pixel classification techniques, single cells inside clumps are counted employing a detection based on CHT. In the other case, they are divided by means of VFC and mathematical morphology operations. The accuracy obtained in counting is outstanding in both cases, as discussed in this section. Three different public datasets have been considered to experiment, test and evaluate the two different proposed workflows. By using them, it becomes clear that ALL-IDB has given accurate samples to train the model, which can generalize enough to obtain good results in the described procedures, as shown in the following results. The first method, called **Det 1** from now on, achieves an average accuracy of 97.61% that in many cases reaches the 99%, outperforming the state-of-the-art methods, such as the method proposed in [MLMR13] that uses the circular Hough transform without any restriction on the area of interest, obtained an average accuracy of 81%, with an high number of false positives, or the method proposed in [AK13], based on a rectangular detection using Gray Level Co-occurrence Matrix, that achieved a 88% of accuracy with a high number of false positives. It is important to note that this method does not produce any false positive, being able to exclude all the other image regions since it is based on a previous phase of segmentation. We reported the ROC curves to show the SVM performances of the new method (see Fig. 8.11). The AUC value is almost always well above the 90%, except in one case. This value is observed only in IUMS-IDB dataset, because it contains images with significant visual defects that weaken the SVM prediction capabilities and, as a consequence, they affect the overall segmentation quality.

The evaluation of the second method, called "Det 2" from now on, is reported in fig. 8.10. Quantitative experimentation has been conducted by considering every single image for a WBCs analysis and relative count. Three metrics have been adopted to evaluate our study: False Negative Rate (FNR), Precision and Recall. The obtained results are reported in table 8.6, column "Det 2". It is evident that this approach correctly identifies 100% of the leukocytes inside ALL-IDB, IUMS-

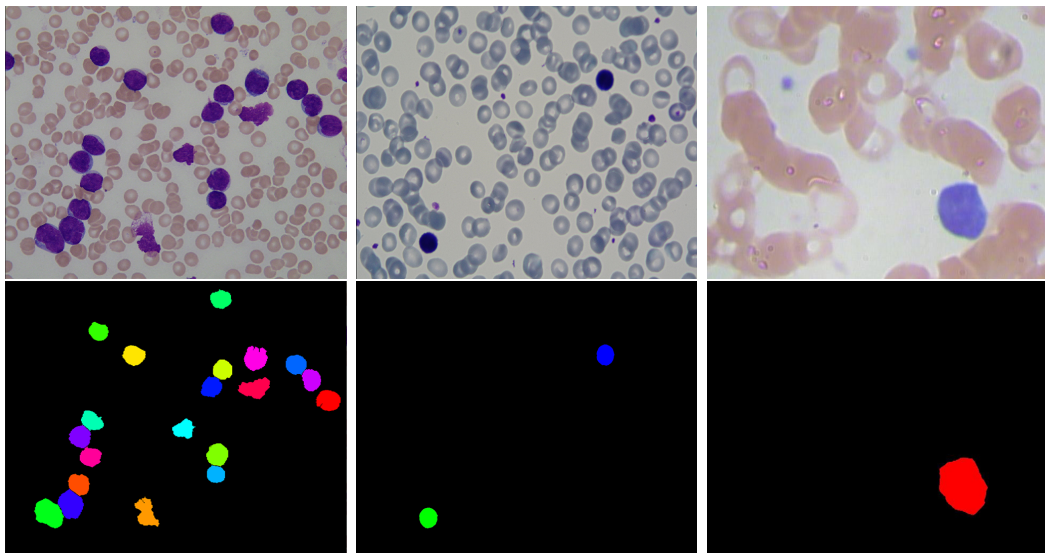


Figure 8.10: Top: from left to right, images extracted from ALL-IDB, IUSMS-IDB and SMC-IDDB, respectively. Bottom: from left to right, the final segmentation results for each image on top.

IDB and SMC-IDB datasets. The majority of clumped cells has been found in ALL-IDB, which presents a lot of complex images, with lots of leukocytes per image and different agglomerates, while IUMS-IDB and SMC-IDB contain simpler images composed of fewer leukocytes and only a few, simpler, agglomerates. They also have poorer quality than the ALL-IDB images. The proposed approach produces no false positives, being able to exclude all other image regions before the detection phase, and thus considering only the portions of the image containing leukocytes.

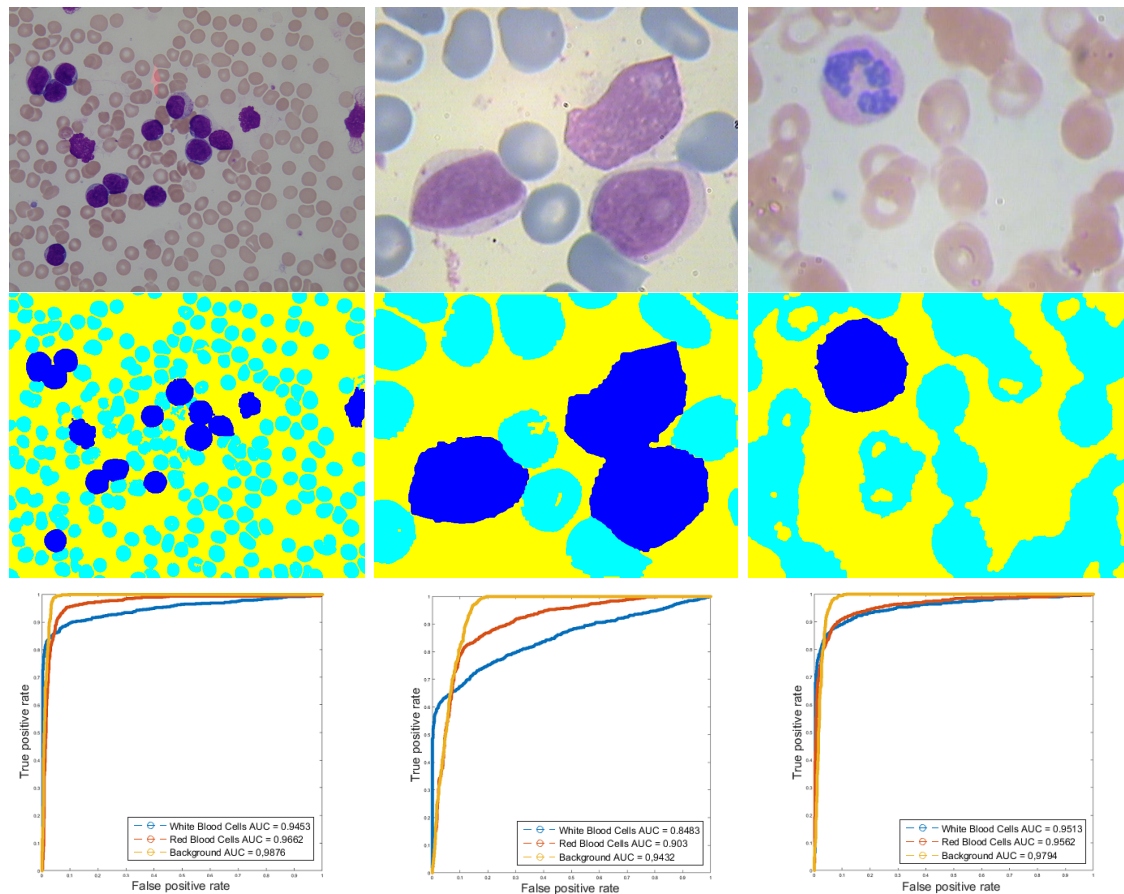


Figure 8.11: Original and segmented images from ALL-IDB1, IUMS-IDB, SMC-IDB and related SVM performances.

Chapter 9

RBC analysis

RBCs or erythrocytes are uniform in size, $7\text{-}8 \mu\text{m}$ in diameter. They are round and flattened like a donut, due to the presence of hemoglobin that is located peripherally, leaving an area of central pallor equal to $1\text{-}3 \mu\text{m}$, approximately 30-45% of the diameter of the cells. While not every RBC is perfect, any significant number of cells that are different in shape or size may indicate the presence of disease [EA13]. Identifying normal and abnormal erythrocytes is important since automated cell counters have not yet replaced the well-trained eye with respect to the subtleties of red blood cell morphology. Erythrocyte color is representative of hemoglobin concentration in the cell, while an abnormal shape may indicate a possible presence of a specific disease or disorder. Some examples of shape and color abnormalities are shown in Fig. 9.1. The cytoplasm of all normal RBCs is free of debris, granules, or other structures. Inclusions are the result of unique conditions, and their identification can be clinically helpful. Some examples of inclusion bodies are shown in Fig. 9.1.

9.1 RBC segmentation

An extension of the work presented in 7.1 is now presented. It refers the work [DRLP16]. This segmentation system is based on a machine learning approach. As for all the approaches involving machine learning techniques, training samples are needed in order to create a model or to make a comparison with the unknown samples. The WBCs, RBCs, and plasma regions are selected from some sample images by performing a manual crop over them to obtain the respective Region Of Interest (ROIs) as shown in Fig. 7.4. The pixels values from R, G and B channels are extracted from the three different ROIs. The obtained pixels are examined with the purpose of avoiding sampling errors and reduced in cardinality by using a Nearest Neighbour Search (NNS) with Euclidean distance. The NNS is applied on pixels belonging to the same region to remove duplicates or close values, therefore pixels with distance $\cong 0$, and outliers or noisy pixels, thus pixels with distance

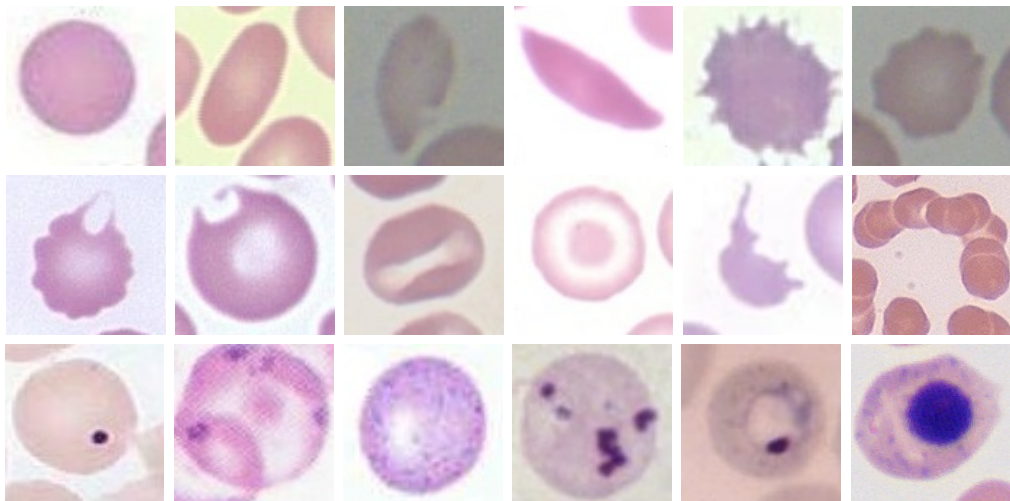


Figure 9.1: From top left to bottom right: shape and colour abnormalities: spherocyte, elliptocyte, tear, sickle, acanthocyte, echinocyte, keratocyte, bite, stomatocytosis, target, schistocyte and rouleaux formation. (Bottom) Inclusions: howell-jolly bodies, siderotic granules, basophilic stippling, Heinz bodies, malaria and nucleated RBC.

$\gg \mu$. Then the NNS is performed over the pixels belonging to different classes so that the intersection among the three classes is empty. Thus the NNS is used to create a smaller but more representative training set. This training set is used to create a multi-class model able to segment the blood components of new images correctly. The model has been obtained by training a Support Vector Machine using a one-vs-rest approach. The kernel used to train the model is the Radial Basis Function, also known as RBF. It uses two parameters: the value of the box constraint c and the value of gamma γ that defines the width of the bell-shaped curve. After a cross-validation procedure we identified the best parameter values that are equal to $1e3$ and $1e1$ for c and γ , respectively. A kernel approach has been preferred over a linear separation among the classes because it can take into account the brightness reductions and the uncertainty present in the images. The results of this approach applied to a new image is a labeled image with different labels for WBCs, RBCs, and plasma, as shown in Fig. 7.4. The just obtained labeled image can be used as a mask over the original image in order to separately analyze each image component. Many cells can be extracted directly from the binary mask but, as previously said, there are many agglomerates of cells that cannot be ignored. During the analysis, all the cells with a size comparable to the ones present in the training set, are recognized as single cells and directly counted. The remaining components, recognized as agglomerates of cells, are submitted to a further step based on circular Hough transform. This step takes advantages of the previous segmentation phase. Indeed, the detection step is performed on the original grey level images as follows. Firstly, the original image is masked with the segmented one, and then every cells

agglomerate is separately analyzed. Using the knowledge acquired from the training set, we can set the correct parameters for the circular Hough transform, that in this way searches only for the circular objects with the appropriate grey level values. Finally, the cells count can be quickly completed by adding the number of circles detected in this step to the single cells count value previously computed. More details about the proposed method for segmentation and cells count can be found in [DRLP16].

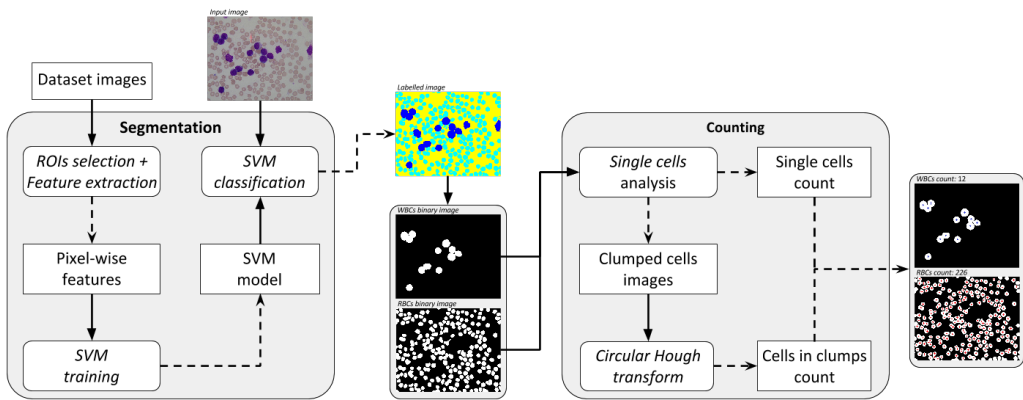


Figure 9.2: Pipeline of this approach.

To train our segmentation approach based on machine learning we have used the images belonging to the ALL-IDB2 version, while to test the whole algorithm we have used the first 33 images of ALL-IDB1 version that have been acquired with the same devices and with the same magnification. The ground truth for all the images has been determined by an expert and used to validate the proposed method. As proposed in literature we evaluated the counting performances using *precision*, *recall*, *F-measure* and then we added a fourth metric, that is the False Negative Rate *FNR*, in order to highlight when the algorithm is not able to detect a cell present in the image. The whole results for WBCs and RBCs counting are reported in Table 9.1, where they have been directly compared with the results obtained by other authors that used the same image dataset. During the experimentations the proposed approach correctly identified 99.2% of the whole leukocytes and the 98% of erythrocytes, also showing a little *FNR* value, being able to neglect just a few cells present in the images. It is also important to note that the proposed approach produces a low number of RBCs false positives and even less WBCs false positives (0%), being able to exclude all the other image regions before the detection phase by considering only portions of the image containing the currently analyzed cells. Through a numerical comparison, it is possible to observe that our method outperforms the detection methods existing in the literature. In particular, the method proposed in [AK13], based on a rectangular detection for WBCs only, using Gray Level Co-occurrence Matrix, achieved an 88% of accuracy with a significant amount of false positives. The method proposed in [MLMR13] uses the circular

Hough transform, like ours does, but it has been applied to different color spaces without any restriction on the area of interest. This method indeed produced an overall accuracy of 81% for WBCs and 64% for RBCs. Also in [ASAZA014], the circular Hough transform has been used, but in that case, the number of candidate circles has been reduced by selecting the one with the higher probability. This operation reduced the number of false positives but also increased the number of true positives, reaching an overall accuracy of 98.4%. It was also, at the best of our knowledge, the method that obtained the best performances applied to the ALL-IDB dataset. It is worth remembering that this system offers the possibility to perform a binary or a multiple segmentation, as shown in Fig. 9.3.

	[ASAZA014] Proposed method			
	WBCs	RBCs	WBCs	RBCs
FNR	1,5%	2,5%	0,7%	2%
Precision	90%	95%	100%	89%
Recall	98%	98%	99,2%	98%
F-measure	94%	96%	99,6%	93%

Table 9.1: Detection and counting of both WBC and RBC performances compared with the state-of-the-art.

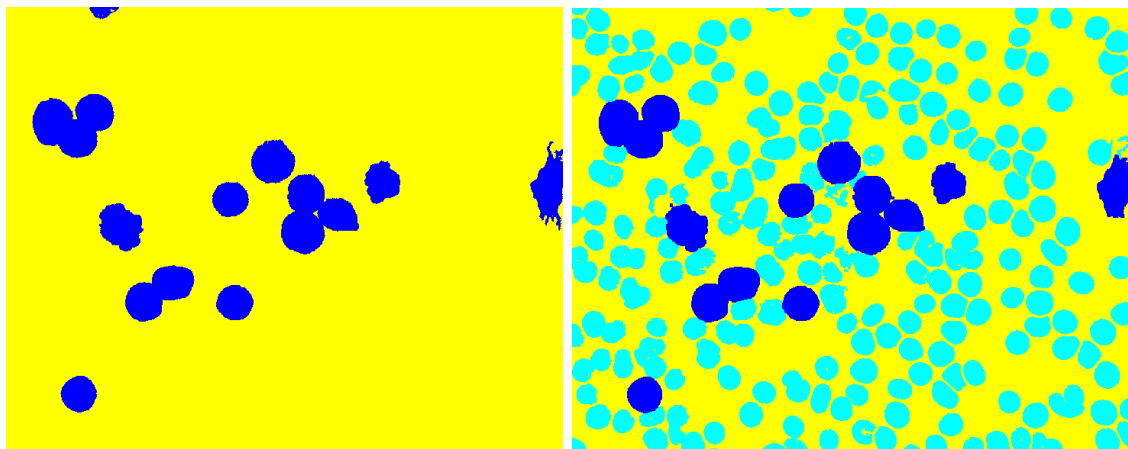


Figure 9.3: Segmentation results after ROI selection for two and three classes. Blue represents WBCs, while light blue represents RBCs.

As it can be seen also in this case the segmentation is really accurate, being able to properly segment WBCs and also RBCs. Using the manually segmented images we have computed the segmentation accuracy of this version that again reaches the 99%.

9.2 MP-IDB: Malaria Parasite Dataset

Malaria is an epidemic health disease. Rapid, and accurate diagnosis is necessary for proper intervention. Generally, pathologists visually examine blood stained slides for malaria diagnosis. Nevertheless, this kind of visual inspection is subjective, error-prone and time-consuming. Numerous methods of automatic malaria diagnosis have been proposed so far, to overcome the issues. In particular, many researchers have used mathematical morphology as a powerful tool for computer-aided malaria detection and classification. Microscopic image analysis and particularly malaria detection and classification can significantly benefit from the use of computer-aided algorithms. For these reasons, a new public dataset has been realized by acquiring images of malaria-affected blood smears. Dataset images have been acquired with a Leica DM2000 optical laboratory microscope at Centre Hospitalier Universitaire Vaudois (CHUV) coupled with a built-in camera and software. The entire procedure has been realized under the supervision of expert radiologists, headed by Dr. Guy Prod'Hom. Every image is stored in PNG format with a 2592×1944 resolution and 24-bit color depth. The images are taken with the same magnification of the microscope: $100\times$. This dataset is composed of 229 images, representing four different kinds of malaria parasite. *Plasmodium Falciparum* is present in 122 images, *Malariae* in 37, *Ovale* in 29 and *Vivax* in 46. Each image contains, at least, one parasite. Our dataset can be used either for testing segmentation capability of algorithms or classification system methods. It contains about 48000 blood cells, in which expert radiologists have labeled malaria parasites. The number of candidate parasites present in the MP-IDB is equal to 840. Specific counting, per parasite type and stage of life, is shown in table 9.2. The annotation of the dataset images is described as follows. The image filenames are named with the following notation: "ImXXXPR.png", in which "XXX" identifies a 3-digit integer counter, P represents one of the four parasite species ('F' for *P.Falciparum*, 'M' for *P.Malariae*, 'O' for *P.Ovale*, 'V' for *P.Vivax*), while the final R stands for the life stage ('R' for ring, 'S' for schizont, 'T' for trophozoite and 'G' for gametocyte stage). Every single image file has a reference text file with the filename notation set to "ImXXXC.xyc", which reports the coordinates of the parasites centroids. In particular, they have manually been estimated by a skilled radiologist at CHUV. These dataset images have been acquired with the same microscope. Unfortunately, lots of them suffer from different issues, like typical non-uniform background illuminations and overexposed borders, due to the illumination of the microscope lamp (visible in fig. 9.4). It also causes that the regions of interest can have different coloration, also due to the age of the analyzed smears. It justifies a strong pre-processing step to make the image conditions the most similar possible, to realize an automated procedure. Even though the images remain intelligible, classic segmentation methods, e.g., based on thresholding, can suffer from these issues. The main targets related to the creation of this dataset are to show how malaria parasite analysis is currently performed and which are the principal issues to deal with. Moreover, we have proposed a

public dataset of blood samples, specifically designed to evaluate and compare the performances in segmentation or classification of malaria parasites by computer vision techniques. Our aim in realizing MP-IDB is to offer a robust image processing dataset, specifically designed to help in encourage new studies about malaria image analysis under a fair comparative approach based on a standard dataset, like what ALL-IDB [LPS11] has offered for leukemia detection and white blood cells analysis [DRLP16].

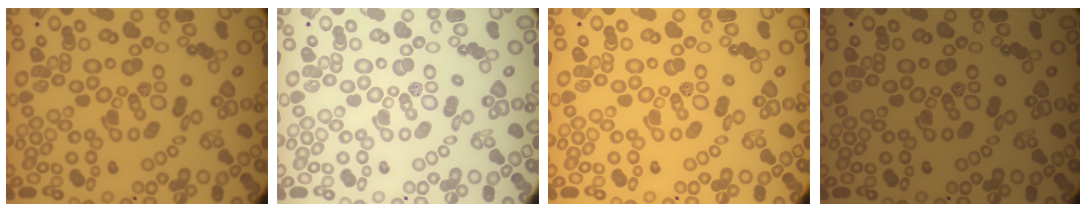


Figure 9.4: From left to right: same smear acquired with four microscope brightness levels. Different illumination conditions could generate unconventional colour schemes in images. Courtesy of CHUV, Lausanne.

Table 9.2: Composition of dataset's images

Dataset properties		
Parasite (images)	Stage of life	Quantity
P. Falciparum (122)	Ring	695
	Trophozoite	2
	Schizont	20
	Gametocyte	3
P. Vivax (41)	Ring	9
	Trophozoite	27
	Schizont	1
	Gametocyte	10
P. Ovale (29)	Ring	13
	Trophozoite	11
	Schizont	1
	Gametocyte	8
P. Malariae (37)	Ring	1
	Trophozoite	18
	Schizont	10
	Gametocyte	11

9.2.1 Homomorphic filtering for image enhancement

Normally, pre-processing methods are used to enhance images. In section 2, we listed a series of linear operators. The objective of this section, instead, is to show how the techniques of multiplicative homomorphic systems are used for enhancing the images in frequency domain, rather than in spacial domain. They are useful because images that make part of MP-IDB has an irregular background due to the illumination lamp, as shown in Fig. 9.5. The image can be characterized by two components, the amount of incident source illumination and amount of illumination reflected by the object. These are called the illumination and reflectance components of the image. The illumination-reflectance model can be used to develop a frequency domain procedure for improving the appearance of an image by simultaneous gray-level range compression and contrast enhancement. Here, the key to the approach is the separation of the illumination and the reflectance components. An image as a function can be expressed as the product of illumination and reflectance components as follows:

$$F(x, y) = I(x, y) * R(x, y) \quad (9.1)$$

Equation 9.1 cannot be used directly to operate separately on the frequency components of illumination and reflectance because the Fourier transform of the product of two functions is not separable. Instead the function can be represented as a logarithmic function wherein the product of the Fourier transform can be represented as the sum of the illumination and reflectance components as shown below:

$$\ln(x, y) = \ln(I(x, y)) + \ln(R(x, y)) \quad (9.2)$$

The Fourier transform of equation 9.2 is:

$$Z(u, v) = Fi(u, v) + Fr(u, v) \quad (9.3)$$

The Fourier transformed signal is processed by means of a filter function $H(u, v)$ and the resulting function is inverse Fourier transformed. Finally, inverse exponential operation yields an enhanced image. This enhancement approach is termed as homomorphic filtering. To get an estimate of $\log(I(x, y, c))$, the idea is to segment $f(x, y, c)$ into object and background. This can be done, for example, by thresholding the green plane or, better, the saturation plane, by using the Otsu threshold. The saturation plane indicates the degree of white in a given color and it is observed that the background has a very low saturation whereas the cells have a larger saturation. Because the saturations histogram exhibits a clear valley, the optimal two classes Otsu classifier can be used. The low frequency background is then estimated, channel by channel, by fitting a quadratic function to the spatial evolution of $f(x, y, c)$ at the background pixels.

$$f_{bg}(x, y, c) = \theta(1, c) + \theta(2, c)x + \theta(3, c)x^2 + \theta(4, c)xy + \theta(5, c)y + \theta(6, c)y^2 \quad (9.4)$$

The coefficients $\theta(1) \dots \theta(6)$ are obtained by a standard least square optimization. Note that for numerical reasons, the x, y coordinates are centered on the image center. When the background $I(x,y)$ has been estimated for each channel R, G and B, its maximum $\text{Max}(c)$, over the entire image is computed and the corrected channel is computed as such:

$$f_{corr}(x, y, c) = 10(flog(x, y, c) + \text{Max}(c)f_{bg}(x, y, c)) \quad (9.5)$$

After having computed 9.5, $c = r,g,b$, the final image is formed by concatenating the 3 planes. The results are shown in the following figures:

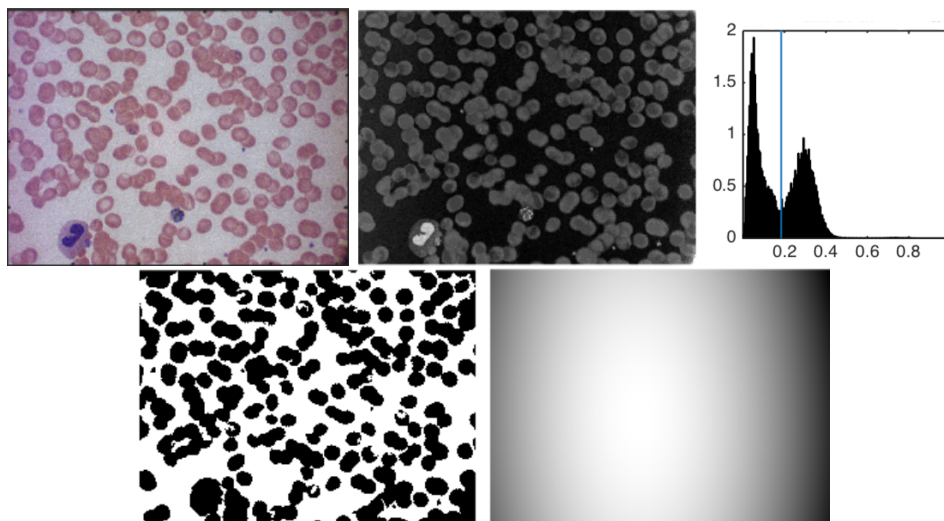


Figure 9.5: From left to right: original RGB image, Saturation channel of HSV space, Histogram of the saturation plane with a vertical line indicating the Otsu threshold. Underneath: segmentation, polynomial estimation of the background evolution. Courtesy of CHUV, Lausanne.

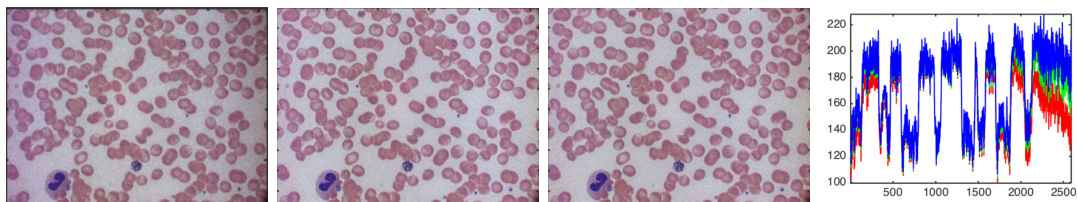


Figure 9.6: From left to right: original RGB image, corrected image by the described method with S channel, corrected image by the described method with G channel, horizontal profiles at the center of the image. In red, the original image, in blue, the proposed with S channel, and in green the proposed method with G channel. Courtesy of CHUV, Lausanne.

The two proposed methods are very similar, the difference between them lies in the segmentation of the background, the proposed method is based on the saturation plane whereas the other method is based on the green plane. The profile shows, in this case, that the saturation plane performs better than the green plane by enlightening more the image on its right side.

Part III

Conclusions

Conclusions and future works

This thesis addressed the automatized visual analysis of peripheral blood cells images, with particular efforts on WBC analysis firstly and RBC, secondly. It has been focused on cells analysis and counting for diagnosing diseases using a microscope, a crucial step to confirm if and which illness is present. The main purpose has been the analysis of the outstanding issues in a CAD from digital microscopy images, particularly Acute Lymphoblastic Leukemia for WBCs and malaria for RBCs. It shows the studies addressed to some possible solutions for cells analysis and counting. Special efforts have been focused on strategies to represent with meaningful information the visual content of digital images. Indeed this issue is critical in artificial vision and becomes further challenging in medical imaging, considering that there is not a color standardization for the staining and acquisition of digital slides. There are several color differences or intensity variations between different slides, due to the quality of the biological sample and the sample preparation, such as the quantity of dye used during the staining procedure, or due to different acquisition systems and the image capturing parameters, such as the environment illumination. Furthermore, mainly in peripheral blood images, such variability may be present in the same slide, due to the presence of uneven lighting caused by the microscope light. Thus, by computing descriptors that ignore this variability, it is possible to extract from the images more general information that may be used by conventional learning models for distinguishing different biological concepts, avoiding any dependency on a specific dataset.

Peripheral blood image analysis has been faced with special efforts towards the segmentation and the counting of both types of cells, either leukocytes and erythrocytes, proposing different segmentation algorithms able to isolate the cell of interest from images acquired in different illumination conditions and with different staining strategies. The experimental results demonstrated that the final approach is very accurate and robust in relation to some traditional methods. It has been able to obtain an average accuracy of 100% in WBC detection and 98 % in RBC detection. The 2% difference is due to the fact that a lot of RBC tend to overlap other RBCs, so that it becomes quite tricky, even for human eye, discover their exact number. The results in this phase have also permitted to identify and count the WBCs correctly, that can be directly used to support some existing medical methods, like the WBCC. The identification of single WBCs is also essential for the diagnosis of

leukemia, for which the cell components must be analyzed in detail, in order to find the morphological changes that can be observed in the cells affected by that disease. Consequently, a further extension could be devoted to the realization of a complete cells classification system, able to distinguish among the several types of WBCs.

Moreover, the identification of RBCs has also been made in standard cell conditions, which is represented by the dataset in WBC analysis. For this reason, this work also contains a new public dataset specifically built and designed for malaria analysis purposes.

It is important to note that many of the proposed approaches could also be used in different medical imaging system and also for artificial vision system far from the medical field. It could be possible thanks to the generality of the proposed approaches, that is designed to overcome many different issues, such as the color differences, that make them independent from dataset and in some cases also from the problem itself.

Despite the good results obtained with both case studies, further improvements can be realized for peripheral blood image analysis. Many other phases can be integrated. In particular, a first improvement could arise from a detailed analysis of the WBCs in order to detect the type of disease that can affect a cell. Moreover, the realized system could also be extended to malaria parasite analysis by using the proposed dataset. Once single cells of each type have been detected and segmented, they can be analyzed in detail, to detect the presence of the parasite, like malaria parasite or to diagnose disease that can affect that particular cell type. It can even be extended to provide new measures, like the parasitemia percentage of an image. These measures can be diagnostic by themselves, since that an overproduction or an underproduction is always a symptom of problems related to the health of the bone marrow. Adapting the system to bone marrow smear images analysis could be another exciting and useful task. Cells in bone marrow differ from peripheral blood cell images because there are only immature cells, so that shape and colors are not the same of peripheral blood cells either due to the absence of standard acquisition techniques or their characteristics. An example is shown underneath.

Finally, we should consider another important aspect which is arising a lot of importance in the community. Deep learning is increasingly used in computer vision and medical image analysis field. However, it is clear that applying deep learning algorithms to medical image analysis presents several unique challenges. The lack of large training data sets is often mentioned as an obstacle, especially in the case of microscopic image analysis. Although medical procedures nowadays tend to release a lot of images from medical procedures, one of the main challenge is also the acquisition of relevant annotations/labeling for these images. Even when data is annotated by domain expert, label noise can be a significant limiting factor in developing algorithms, whereas in computer vision the noise in the labeling of images is typically relatively low. Training a deep learning system on such data requires careful consideration of how to deal with noise and uncertainty in the reference standard. One partial solution could be incorporating labeling uncertainty directly

in the loss function, but this is still an open challenge. In medical imaging often classification or segmentation is presented as a binary task: normal versus abnormal, object versus background. However, this is often a gross simplification as both classes can be highly heterogeneous. For example, in our case, the normal category consists of completely normal blood cells but also several categories of leukemia or parasites exist for the abnormal category. This often leads to systems that are extremely good at excluding the most common normal subclasses, but fail miserably on several rare ones. A straightforward solution would be to turn the deep learning system in a multi-class system by providing it with detailed annotations of all possible subclasses. From a certain point of view, this thesis also faced this issue at a first approximation. More efforts can be made in order to improve the solution.

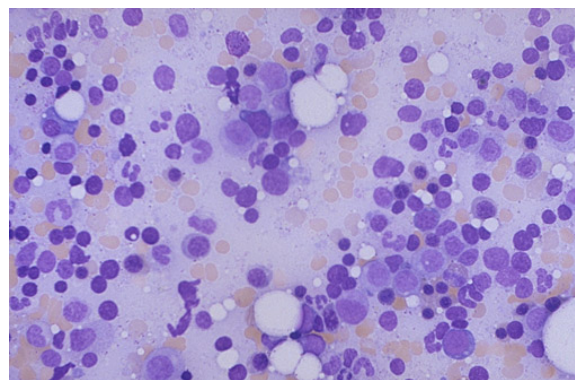


Figure 9.7: Bone marrow smear image. Erythroid and granulocytic precursors are present. Courtesy of [Uta18]

Bibliography

- [AGR⁺14] J.E. Arco, J.M. Gorriz, J. Ramirez, I. Alvarez, and C.G. Puntonet. Digital image analysis for automatic enumeration of malaria parasites using morphological operations. *Expert Systems with Applications*, 42(6):3041 – 3047, 2014.
- [AK13] M. Alilou and V. Kovalev. Automatic object detection and segmentation of the histocytology images using reshapable agents. *Image Analysis and Stereology*, 32(2):89–99, 2013.
- [ANP⁺11] D. Anggraini, A.S. Nugroho, C. Pratama, I.E. Rozi, A.A. Iskandar, and R.N. Hartono. Automated status identification of microscopic images obtained from malaria thin blood smears. In *In Proceedings of the 2011 International Conference on Electrical Engineering and Informatics*, pages 1–6, July 2011.
- [APA12] N. Ahirwar, S. Pattnaik, and B. Acharya. Advanced image analysis based system for automatic detection and classification of malarial parasite in blood images. *International Journal of Information Technology and Knowledge Management*, 5(1):59–64, 2012.
- [AS02] J. Angulo and J. Serra. Morphological color size distributions for image classification and retrieval. In *International Conference on Advanced Concepts for Intelligent Vision Systems*, pages 46–53, 2002.
- [ASAZAO14] Yazan M Alomari, Siti Norul Huda Sheikh Abdullah, Raja Zaharatul Azma, and Khairuddin Omar. Automatic detection and quantification of wbcs and rbcs using iterative structured circle detection algorithm. *Computational and mathematical methods in medicine*, 2014, 2014.
- [ASEH] Ahmed M. Abdeldaim, Ahmed T. Sahlol, Mohamed Elhoseny, and Aboul Ella Hassanien. *Computer-Aided Acute Lymphoblastic Leukemia Diagnosis System Based on Image Analysis*, pages 131–147. Springer International Publishing, Cham.

- [BCMT⁺76] J. M. Bennett, D. Catovsky, D. Marie-Therese, G. Flandrin, D. A. G. Galton, H. R. Gralnick, and C. Sultan. Proposals for the classification of the acute leukaemias french-american-british (FAB) co-operative group. *British Journal of Haematology*, 33(4):451–458, 1976.
- [BCPP00] A. Biondi, G. Cimino, R. Pieters, and C.-H. Pui. Biological and therapeutic aspects of infant leukemia. *Blood*, 96(1):24–33, 2000.
- [BDVD12] X. Benavent, E. Dura, F. Vegara, and J. Domingo. Mathematical morphology for color images: An image-dependent approach. *Mathematical Problems in Engineering*, 2012(678326):1 – 19, 2012.
- [BH07] M. Benčo and R. Hudec. Novel method for color textures features extraction based on glcm. *Radioengineering*, 4(16):64–67, 2007.
- [Bri] Britannica. Blood analysis. <https://www.britannica.com/topic/blood-analysis>.
- [BS07] L. Bing and T. Scott. Active contour external force using vector field convolution for image segmentation. *Acton, vol. 16, pp. 2096 - 2106*, 2007.
- [BSa08] S. Buavirat and C. Srisa-an. Classification for acute lymphocytic leukemia using feature extraction and neural networks in white blood cell stained images. 2008.
- [BTG06] H. Bay, T.uytelaars, and L. Van Gool. Surf: Speeded up robust features. In *ECCV European Conference on Computer Vision*, volume 3951 of *Lecture Notes in Computer Science*, pages 404–417. Springer Berlin Heidelberg, 2006.
- [BTKD11] H. Berge, D. Taylor, S. Krishnan, and T. S. Douglas. Improved red blood cell counting in thin blood smears. In *IEEE International Symposium on Biomedical Imaging: From Nano to Macro*, pages 204–207, March 2011.
- [BVMP04] L. Busin, N. Vandenbroucke, L. Macaire, and J. G. Postaire. Color space selection for unsupervised color image segmentation by histogram multithresholding. In *International Conference on Image Processing*, volume 4, pages 203–206, October 2004.
- [Caf98] R. E. Caflisch. Monte carlo and quasi-monte carlo methods. *Acta numerica*, 7:1–49, 1998.

- [Can86] J. Canny. A computational approach to edge detection. *IEEE Transactions on Pattern Analysis and Machine Intelligence*, PAMI-8(6):679–698, Nov 1986.
- [CDC18] Med CDC. Malaria parasite descriptions. <http://www.microbiologybook.org/parasitology/blood-malaria.htm>, 2018. [Online; accessed 05-Oct-2018].
- [CH67] T. M. Cover and P. E. Hart. Nearest neighbor pattern classification. *IEEE Transactions on Information Theory*, 13(1):21–27, 1967.
- [CH80] R. W. Connors and C. A. Harlow. A theoretical comparison of texture algorithms. *IEEE Transactions on Pattern Analysis and Machine Intelligence*, PAMI-2(3):204–222, May 1980.
- [Cie11] B. Ciesla. *Hematology in practice*. FA Davis, 2011.
- [Cla02] D. A. Clausi. An analysis of co-occurrence texture statistics as a function of grey level quantization. *Canadian Journal of Remote Sensing*, 28(1):45–62, 2002.
- [CMT⁺16] Claire Lifan Chen, Ata Mahjoubfar, Li-Chia Tai, Ian K Blaby, Allen Huang, Kayvan Reza Niazi, and Bahram Jalali. Deep learning in label-free cell classification. *Scientific reports*, 6:21471, 2016.
- [Cou56] W. H. Coulter. High speed automatic blood cell counter and cell size analyzer. In *National Conference on Electronics*, pages 1034–1040, October 1956.
- [CR03] T. Chaira and A. K. Ray. Segmentation using fuzzy divergence. *Pattern Recognition Letters*, 24(12):1837–1844, Aug 2003.
- [Cse92] I. Cseke. A fast segmentation scheme for white blood cell images. In *IAPR International Conference on Pattern Recognition. Vol. III: Image, Speech and Signal Analysis*, pages 530–533, 1992.
- [CWCT09] S. Chen, C. Wu, D. Chen, and W. Tan. Scene classification based on gray level-gradient co-occurrence matrix in the neighborhood of interest points. In *IEEE International Conference ICIS on Intelligent Computing and Intelligent Systems*, volume 4, pages 482–485, Nov 2009.
- [DGC⁺11] D.K. Das, M. Ghosh, C. Chakraborty, A.K. Maiti, and M. Pal. Probabilistic prediction of malaria using morphological and textural information. In *In Proceedings of the 2011 International*

- Conference on Image Information Processing (ICIIP)*, pages 1–6. IEEE, 2011.
- [DGP⁺13] D.K. Das, M. Ghosh, M. Pal, A.K. Maiti, and C. Chakraborty. Machine learning approach for automated screening of malaria parasite using light microscopic images. *Micron*, 45:97 – 106, 2013.
- [DGR09] G. Diaz, F.A. Gonzalez, and E. Romero. A semi-automatic method for quantification and classification of erythrocytes infected with malaria parasites in microscopic images. *Journal of Biomedical Informatics*, 42:296–307, 2009.
- [DH73] R. O. Duda and P. E. Hart. *Pattern classification and scene analysis*, volume 3. Wiley New York, 1973.
- [DMC14] D.K. Das, A.K. Maiti, and C. Chakraborty. *Textural pattern classification of microscopic images for malaria screening*, chapter 19, pages 419–446. CRC Press, 2014.
- [DMC15] D.K. Das, R. Mukherjee, and C. Chakraborty. Computational microscopic imaging for malaria parasite detection: a systematic review. *Journal of microscopy*, 260(1):1–19, 2015.
- [DRB⁺15] R. Dey, K. Roy, D. Bhattacharjee, M. Nasipuri, and P. Ghosh. An automated system for segmenting platelets from microscopic images of blood cells. In *In Proceedings of the 2015 International Symposium on Advanced Computing and Communication (ISACC)*, pages 230–237, 2015.
- [DRDKJ02] C. Di Ruberto, A. Dempster, S. Khan, and B. Jarra. Analysis of infected blood cell images using morphological operators. *Image and Vision Computing*, 20(2):133 – 146, 2002.
- [DRLP16] C. Di Ruberto, A. Loddo, and L. Putzu. A leucocytes count system from blood smear images: Segmentation and counting of white blood cells based on learning by sampling. *Machine Vision and Applications*, 27(8):1151–1160, 2016.
- [DSSL17] S.S. Devi, J. Singha, M. Sharma, and R.H. Laskar. Erythrocyte segmentation for quantification in microscopic images of thin blood smears. *Journal of Intelligent and Fuzzy Systems*, 32:2847–2856, 2017.
- [DT05] N. Dalal and B. Triggs. Histograms of oriented gradients for human detection. In *IEEE Computer Society Conference CVPR on Computer Vision and Pattern Recognition*, volume 1, pages 886–893 vol. 1, June 2005.

- [DU17] I.R. Dave and K.P. Upla. Computer aided diagnosis of malaria disease for thin and thick blood smear microscopic images. In *In Proceedings of the 2017 4th International Conference on Signal Processing and Integrated Networks (SPIN)*, pages 561–561, 2017.
- [EA13] O. Erhabor and T. C. Adias. *Hematology made easy*. Author-House, 2013.
- [EHZ11] M. Elter, E. Haßlmeyer, and T. Zerfaß. Detection of malaria parasites in thick blood films. In *In Proceedings of the 2011 Annual International Conference of the IEEE Engineering in Medicine and Biology Society*, pages 5140–5144, 2011.
- [FCMG00] D. J. Foran, D. Comaniciu, P. Meer, and L. Goodell. Computer-assisted discrimination among malignant lymphomas and leukemia using immunophenotyping, intelligent image repositories, and telemicroscopy. *IEEE Transactions on Information Technology in Biomedicine*, 4(4):265–273, 2000.
- [FH75] K. Fukunaga and L. Hostetler. The estimation of the gradient of a density function, with applications in pattern recognition. *IEEE Transactions on Information Theory*, 21(1):32–40, Jan 1975.
- [GBea16] A. Gonzalez-Betancourt and P. Rodriguez-Ribalta et alt. Automated marker identification using the radon transform for watershed segmentation. *IET Image Processing*, 11(3):183–189, 2016.
- [GD88] C.R. Giardina and E.R. Dougherty. *Morphological Methods in Image and Signal Processing*. Prentice-Hall, Inc., Upper Saddle River, NJ, USA, 1988.
- [GVB07] A. Gelzinis, A. Verikas, and M. Bacauskiene. Increasing the discrimination power of the co-occurrence matrix-based features. *Pattern Recognition*, 40(9):2367–2372, 2007.
- [GW07] R. C. Gonzalez and R. E. Woods. *Digital image processing*. Pearson Prentice Hall Pearson Education, 3rd edition, 2007.
- [GW12] R. Gong and H. Wang. Steganalysis for GIF images based on colors-gradient co-occurrence matrix. *Optics Communications*, 285:4961–4965, November 2012.
- [GWE04] R. C. Gonzalez, R. E. Woods, and S. L. Eddins. *Digital Image Processing Using MATLAB*. Pearson Prentice Hall Pearson Education, New Jersey, USA, 1st edition, 2004.

- [HCx09] Y. Hu and Z. Chun-xia. Unsupervised texture classification by combining multi-scale features and k-means classifier. In *CCPR Chinese Conference on Pattern Recognition*, pages 1–5, Nov 2009.
- [HMH11] N. H. A. Halim, M. Y. Mashor, and R. Hassan. Automatic blasts counting for acute leukemia based on blood samples. *International Journal of Research and Reviews in Computer Science*, 2(4), 2011.
- [HSD73] R. M. Haralick, K. Shanmugam, and I. H. Dinstein. Textural features for image classification. *IEEE Transactions on Systems, Man and Cybernetics*, SMC-3(6):610–621, 1973.
- [HSP02] H. Hengen, S. L. Spoor, and M. C. Pandit. Analysis of blood and bone marrow smears using digital image processing techniques. In *Medical Imaging*, volume 4684, pages 624–635, 2002.
- [IGM13] H. Inaba, M. Greaves, and C. G. Mullighan. Acute lymphoblastic leukaemia. *The Lancet*, 381(9881):1943–1955, 2013.
- [JF90] A. K. Jain and F. Farrokhnia. Unsupervised texture segmentation using gabor filters. In *IEEE International Conference on Systems, Man and Cybernetics*, pages 14–19, Nov 1990.
- [Jia09] X. Jiang. Feature extraction for image recognition and computer vision. In *In Proceedings of the 2009 2nd IEEE International Conference on Computer Science and Information Technology (ICCSIT)*, pages 1–15, 2009.
- [JRQ03] C. R. Maurer Jr and V. Raghavan R. Qi. A linear time algorithm for computing exact euclidean distance transforms of binary images in arbitrary dimensions. *IEEE Transactions on Pattern Analysis and Machine Intelligence*, 25(2):265–270, 2003.
- [KAG13] H. B. Kekre, B. Archana, and H. R. Galiyal. Segmentation of blast using vector quantization. *International Journal of Computer Applications*, 72(15), June 2013.
- [KASS11] M.I. Khan, B. Acharya, B.K. Singh, and J. Soni. Content based image retrieval approaches for detection of malarial parasite in blood images. *International Journal of Biometrics and Bioinformatics (IJBB)*, 5(2):97–110, 2011.
- [KGHS96] V. A. Kovalev, A. Y. Grigoriev, and A. Hyo-Sok. Robust recognition of white blood cell images. In *International Conference on Pattern Recognition*, volume 4, pages 371–375, Aug 1996.

- [Kit78] J. Kittler. Feature set search algorithms. In *Pattern Recognition and Signal Processing*, pages 41–60. Sijthoff and Noordhoff, Alphen aan den Rijn, 1978.
- [KKM12] S. Kareem, I. Kale, and R.C.S. Morling. Automated malaria parasite detection in thin blood films:- a hybrid illumination and color constancy insensitive, morphological approach. In *In Proceedings of the 2012 IEEE Asia Pacific Conference on Circuits and Systems (APCCAS)*, pages 240–243, 2012.
- [KMK11] S. Kareem, R.C.S. Morling, and I. Kale. A novel method to count the red blood cells in thin blood films. In *In Proceedings of the 2011 IEEE International Symposium on Circuits and Systems (ISCAS)*, pages 1021–1024, 2011.
- [KP17] T Karthikeyan and N Poornima. Microscopic image segmentation using fuzzy c means for leukemia diagnosis. *Leukemia*, 4(1), 2017.
- [KSH12] Alex Krizhevsky, Ilya Sutskever, and Geoffrey E. Hinton. Imagenet classification with deep convolutional neural networks. In *Proceedings of the 25th International Conference on Neural Information Processing Systems - Volume 1*, NIPS’12, pages 1097–1105, USA, 2012. Curran Associates Inc.
- [KSW85] J. N. Kapur, P. K. Sahoo, and A. K. C. Wong. A new method for gray-level picture thresholding using the entropy of the histogram. *Computer Vision, Graphics, and Image Processing*, 29(3):273–285, 1985.
- [KWT88] M. Kass, A. Witkin, and D. Terzopoulos. Snakes: Active contour models. *International Journal of Computer Vision*, 1(4):321–331, 1988.
- [LBBH98] Y. Lecun, L. Bottou, Y. Bengio, and P. Haffner. Gradient-based learning applied to document recognition. *Proceedings of the IEEE*, 86(11):2278–2324, Nov 1998.
- [LC02] O. Lezoray and H. Cardot. Cooperation of color pixel classification schemes and color watershed: a study for microscopic images. *IEEE Transactions on Image Processing*, 11(7):783–789, Jul 2002.
- [LDRK18] Andrea Loddo, Cecilia Di Ruberto, and Michel Kocher. Recent advances of malaria parasites detection systems based on mathematical morphology. *Sensors*, 18(2), 2018.

- [LEC⁺98] O. Lezoray, A. Elmoataz, H. Cardot, G. Gougeon, M. Lecluse, H. Elie, and M. Revenu. Segmentation of cytological image using color and mathematical morphology. In *European conference on Stereology*, 1998.
- [Lin02] J. Lindblad. Development of algorithms for digital image cytometry. *Comprehensive Summaries of Uppsala Dissertations from the Faculty of Science and Technology*, 2002.
- [LIT92] P. Langley, W. Iba, and K. Thompson. An analysis of bayesian classifiers. In *National Conference on Artificial Intelligence*, volume 90, pages 223–228. AAAI Press, July 1992.
- [Low04] D. G. Lowe. Distinctive image features from scale-invariant keypoints. *International Journal of Computer Vision*, 60(2):91–110, 2004.
- [LPDRF16] Andrea Loddo, Lorenzo Putzu, Cecilia Di Ruberto, and Gianni Fenu. A computer-aided system for differential count from peripheral blood cell images. In *In Proceedings of the 2016 12th International Conference on Signal-Image Technology Internet-Based Systems (SITIS)*, pages 112–118, 2016.
- [LPS11] R. Donida Labati, V. Piuri, and F. Scotti. All-idb: The acute lymphoblastic leukemia image database for image processing. In *IEEE ICIP International Conference on Image Processing*, pages 2045–2048, Sept 2011.
- [MAAB13] L. Malihi, K. Ansari-Asl, and A. Behbahani. Malaria parasite detection in giemsa-stained blood cell images. In *In Proceedings of the 2013 8th Iranian Conference on Machine Vision and Image Processing (MVIP)*, pages 360–365, 2013.
- [MDD13] M.C. Mushabe, R. Dendere, and T.S. Douglas. Automated detection of malaria in giemsa-stained thin blood smears. In *In Proceedings of the 2013 35th Annual International Conference of the IEEE Engineering in Medicine and Biology Society (EMBC)*, pages 3698–3701, 2013.
- [MdSV⁺97] N. Malpica, C. Ortiz de Solorzano, J. J. Vaquero, A. Santos, I. Vallcorba, J. M. Garcia-Sagredo, and F. del Pozo. Applying watershed algorithms to the segmentation of clustered nuclei. *Cytometry*, 28(4):289–297, Sep 1997.
- [Mey94] F. Meyer. Topographic distance and watershed lines. *Signal processing*, 38(1):113–125, 1994.

- [MFG12] M. Mohamed, B. Far, and A. Guaily. An efficient technique for white blood cells nuclei automatic segmentation. In *IEEE International Conference on Systems, Man, and Cybernetics (SMC)*, pages 220–225, Oct 2012.
- [MH80] D. Marr and E. Hildreth. Theory of edge detection. *Proceedings of the Royal Society of London B: Biological Sciences*, 207(1167):187–217, 1980.
- [Mis] [Mis]
- [MKA⁺10] H. T. Madhloom, S. A. Kareem, H. Ariffin, A. A. Zaidan, H. O. Alanazi, and B. B. Zaidan. An automated white blood cell nucleus localization and segmentation using image arithmetic and automatic threshold. *Journal of Applied Sciences*, 10(11):959–966, 2010.
- [MLMR13] N. H. Mahmood, P. C. Lim, S. M. Mazalan, and M. A. A. Razak. Blood cells extraction using color based segmentation technique. *International Journal of Life Sciences Biotechnology and Pharma Research*, 2(2), 2013.
- [MMN⁺12] D. Mitrea, P. Mitrea, S. Nedevschi, R. Badea, M. Lupșor, M. Socaciu, A. Golea, C. Hagiu, and L. Ciobanu. Abdominal tumor characterization and recognition using superior-order cooccurrence matrices, based on ultrasound images. *Computational and mathematical methods in medicine*, 2012, 2012.
- [MP10a] S. Mohapatra and D. Patra. Automated cell nucleus segmentation and acute leukemia detection in blood microscopic images. In *ICSMB International Conference on Systems in Medicine and Biology*, pages 49–54, Dec 2010.
- [MP10b] S. Mohapatra and D. Patra. Automated leukemia detection using hausdorff dimension in blood microscopic images. In *INTERACT International Conference on Emerging Trends in Robotics and Communication Technologies*, pages 64–68, Dec 2010.
- [MPCB⁺13] P. Melo-Pinto, P. Couto, H. Bustince, E. Barrenechea, M. Pagola, and J. Fernandez. Image segmentation using atanassovs intuitionistic fuzzy sets. *Expert Systems with Applications*, 40(1):15–26, 2013.
- [MPS10] S. Mohapatra, D. Patra, and S. Satpathy. Image analysis of blood microscopic images for acute leukemia detection. In *International Conference IECR on Industrial Electronics, Control Robotics*, pages 215–219, Dec 2010.

- [MPS14] S. Mohapatra, D. Patra, and S. Satpathy. An ensemble classifier system for early diagnosis of acute lymphoblastic leukemia in blood microscopic images. *Neural Computing and Applications*, 24(7-8):1887–1904, 2014.
- [NK00] M. Nachtegael and E.E. Kerre. *Classical and Fuzzy Approaches towards Mathematical Morphology*, volume 52 of *Studies in Fuzziness and Soft Computing*, chapter 1, pages 3–57. Physica, Heidelberg, 2000.
- [OPEea17] A.D. Oliveira, C. Prats, M. Espasa, and et al. The malaria system microapp: A new, mobile device-based tool for malaria diagnosis. *JMIR Research Protocols*, 6(4):1–11, 2017.
- [OPH96] T. Ojala, M. Pietikinen, and D. Harwood. A comparative study of texture measures with classification based on featured distributions. *Pattern Recognition*, 29(1):51–59, 1996.
- [Ots75] N. Otsu. A threshold selection method from gray-level histograms. *Automatica*, 11(285-296):23–27, 1975.
- [PCR14] L. Putzu, G. Caocci, and C. Di Ruberto. Leucocyte classification for leukaemia detection using image processing techniques. *Artificial Intelligence in Medicine*, 62(3):179–191, 2014.
- [PLC09] C. Pan, H. Lu, and F. Cao. Segmentation of blood and bone marrow cell images via learning by sampling. In *Emerging Intelligent Computing Technology and Applications*, volume 5754 of *Lecture Notes in Computer Science*, pages 336–345. Springer Berlin Heidelberg, 2009.
- [PLPD18] Simone Porcu, Andrea Loddo, Lorenzo Putzu, and Cecilia Di Ruberto. White blood cells counting via vector field convolution nuclei segmentation. In *Proceedings of the 13th International Joint Conference on Computer Vision, Imaging and Computer Graphics Theory and Applications - Volume 4: VISAPP*, pages 227–234. INSTICC, SciTePress, 2018.
- [PR88] S. K. Pal and A. Rosenfeld. Image enhancement and thresholding by optimization of fuzzy compactness. *Pattern Recognition Letters*, 7(2):77–86, 1988.
- [PR13] L. Putzu and C. Di Ruberto. Investigation of different classification models to determine the presence of leukemia in peripheral

- blood image. In *ICIAP International Conference on Image Analysis and Processing*, volume 8156 of *Lecture Notes in Computer Science*, pages 612–621. Springer Berlin Heidelberg, 2013.
- [PS04] V. Piuri and F. Scotti. Morphological classification of blood leucocytes by microscope images. In *IEEE International Conference CIMA on Computational Intelligence for Measurement Systems and Applications*, pages 103–108, July 2004.
- [Qui86] J. R. Quinlan. Induction of decision trees. *Machine Learning*, 1(1):81–106, 1986.
- [RAS⁺00] K. Ramar, S. Arumugam, S.N. Sivanandam, L. Ganesan, and D. Manimegalai. Quantitative fuzzy measures for threshold selection. *Pattern Recognition Letters*, 21(1):1–7, 2000.
- [RdCEC17] Luis Rosado, Jose M. Correia da Costa, Dirk Elias, and Jaime S. Cardoso. Mobile-based analysis of malaria-infected thin blood smears: Automated species and life cycle stage determination. *Sensors*, 17(2167):1–22, 2017.
- [RDKJ00] C. Di Ruberto, A. Dempster, S. Khan, and B. Jarra. Automatic thresholding of infected blood images using granulometry and regional extrema. In *International Conference on Pattern Recognition*, volume 3, pages 441–444 vol.3, 2000.
- [RKM15] S. K. Reni, I. Kale, and R. Morling. Analysis of thin blood images for automated malaria diagnosis. In *In Proceedings of the 2015 E-Health and Bioengineering Conference (EHB)*, pages 1–4, 2015.
- [RLP15a] C. Di Ruberto, A. Loddo, and L. Putzu. Learning by sampling for white blood cells segmentation. In *ICIAP International Conference on Image Analysis and Processing*, volume 9279 of *Lecture Notes in Computer Science*, pages 557–567. Springer International Publishing, 2015.
- [RLP15b] C. Di Ruberto, A. Loddo, and L. Putzu. A multiple classifier learning by sampling system for white blood cells segmentation. In *International Conference CAIP on Computer Analysis of Images and Patterns*, volume 9257 of *Lecture Notes in Computer Science*, pages 415–425. Springer International Publishing, 2015.
- [PRPD06] N.E. Ross, C.J. Pritchard, D.M. Rubin, and A.G. Dusé. Automated image processing method for the diagnosis and classification of malaria on thin blood smears. *Medical and Biological Engineering and Computing*, 44(5):427–436, 2006.

- [RRSRBRMC16] M.F. Romero-Rondon, L.M. Sanabria-Rosas, L.X. Bautista-Rozo, and A. Mendoza-Castellanos. Algorithm for detection of overlapped red blood cells in microscopic images of blood smears. *DYNA*, 83(198):187–194, 2016.
- [RSBK14] J. Rawat, A. Singh, H. S. Bhaduria, and I. Kumar. Comparative analysis of segmentation algorithms for leukocyte extraction in the acute lymphoblastic leukemia images. In *International Conference on Parallel, Distributed and Grid Computing*, pages 245–250, December 2014.
- [Sco05] F. Scotti. Automatic morphological analysis for acute leukemia identification in peripheral blood microscope images. In *IEEE International Conference CIMSA on Computational Intelligence for Measurement Systems and Applications*, pages 96–101, July 2005.
- [Sco06] F. Scotti. Robust segmentation and measurements techniques of white cells in blood microscope images. In *IEEE IMTC Instrumentation and Measurement Technology Conference*, pages 43–48, April 2006.
- [SDH⁺91] S. Serbouti, A. Duhamel, H. Harms, U. Gunzer, H. M. Aus, J.-Y. Mary, and R. Beuscart. Image segmentation and classification methods to detect leukemias. In *IEEE International Conference on Engineering in Medicine and Biology Society*, volume 13, pages 260–261, Oct 1991.
- [Ser83a] J. Serra. *Image analysis and mathematical morphology*, volume I. Academic Press, Inc., 1983.
- [Ser83b] J. Serra. *Image analysis and mathematical morphology, Theoretical Advances*, volume II. Academic Press, Inc., 1983.
- [Ser84] J. Serra. *Image Analysis and Mathematical Morphology*. Academic Press, 1984.
- [SF68] Irwin Sobel and Gary Feldman. A 3x3 isotropic gradient operator for image processing. *a talk at the Stanford Artificial Project in*, pages 271–272, 1968.
- [SMK11] J. Soni, N. Mishra, and C. Kamargaonkar. Automatic difference between rbc and malaria parasites based on morphology with first order features using image processing. *International Journal of Advances in Engineering and Technology*, 1:290–297, 2011.

- [SN11a] S.S. Savkare and S.P. Narote. Automatic classification of normal and infected blood cells for parasitemia detection. *International Journal of Computer Science and Network Security (IJCSS)*, 11(2):94–97, 2011.
- [SN11b] S.S. Savkare and S.P. Narote. Automatic detection of malaria parasites for estimating parasitemia. *International Journal of Computer Science and Security (IJCSS)*, 5(3):310–315, 2011.
- [SN15] S.S. Savkare and S.P. Narote. Blood cell segmentation from microscopic blood images. In *In Proceedings of the 2015 International Conference on Information Processing (ICIP)*, pages 502–505, 2015.
- [Soi04] P. Soille. *Morphological Image Analysis: Principles and Applications*. Springer, 2004.
- [Som11] J. Somasekar. Computer vision for malaria parasite classification in erythrocytes. *International Journal on Computer Science and Engineering*, 3(6):2251–2256, 2011.
- [Špr09] V. Špringl. Automatic malaria diagnosis through microscopy imaging. Master’s thesis, Czech Technical University in Prague, Faculty of Electrical Engineering, Czech Republic, 2009.
- [SR03] N. Sinha and A. G. Ramakrishnan. Automation of differential blood count. In *TENCON Conference on Convergent Technologies for the Asia-Pacific Region*, volume 2, pages 547–551, Oct 2003.
- [SR15] J. Somasekar and B.E. Reddy. Segmentation of erythrocytes infected with malaria parasites for the diagnosis using microscopy imaging. *Computers and Electrical Engineering*, 45:336–351, 2015.
- [SR17] J. Somasekar and B.E. Reddy. A novel two-stage thresholding method for segmentation of malaria parasites in microscopic blood images. *Journal of Biomedical Engineering and Medical Imaging*, 4(2):31–42, 2017.
- [SRPP15] D.H. Sulistyawati, F.Z. Rahmanti, I.K.E. Purnama, and M.H. Purnomo. Automatic segmentation of malaria parasites on thick blood film using blob analysis. In *In Proceedings of the 2015 International Seminar on Intelligent Technology and Its Applications*, pages 137–142, 2015.
- [SRTB14] O. Sarrafzadeh, H. Rabbani, A. Talebi, and H. U. Banaem. Selection of the best features for leukocytes classification in blood smear microscopic images, 2014.

- [SRZT13] M. Sheikhhosseini, H. Rabbani, M. Zekri, and A. Talebi. Automatic diagnosis of malaria based on complete circle ellipse fitting search algorithm. *Journal of Microscopy*, 252(3):189–203, 2013.
- [ST99] L.-K. Soh and C. Tsatsoulis. Texture analysis of sar sea ice imagery using gray level co-occurrence matrices. *IEEE Transactions on Geoscience and Remote Sensing*, 37(2):780–795, Mar 1999.
- [SZ14] Karen Simonyan and Andrew Zisserman. Very deep convolutional networks for large-scale image recognition. *CoRR*, abs/1409.1556, 2014.
- [Tan98] X. Tang. Texture information in run-length matrices. *IEEE Transactions on Image Processing*, 7(11):1602–1609, Nov 1998.
- [TDK06] F.B. Tek, A.G. Dempster, and I. Kale. Malaria parasite detection in peripheral blood images. In *In Proceedings of the 2006 British Machine Vision Conference (BMVC)*, pages 347–356, 2006.
- [TDK10] F.B. Tek, A.G. Dempster, and I. Kale. Parasite detection and identification for automated thin blood film malaria diagnosis. *Computer Vision and Image Understanding*, 114(1):21 – 32, 2010.
- [Uta18] Med Utah. Bone marrow smear. <https://library.med.utah.edu/WebPath/HEMEHTML/HEME151.html>, 2018. [Online; accessed 05-Oct-2018].
- [VLMea16] Gulshan V, Peng L, Coram M, and et al. Development and validation of a deep learning algorithm for detection of diabetic retinopathy in retinal fundus photographs. *JAMA*, 316(22):2402–2410, 2016.
- [VMP03] N. Vandenbroucke, L. Macaire, and J.-G. Postaire. Color image segmentation by pixel classification in an adapted hybrid color space. application to soccer image analysis. *Computer Vision and Image Understanding*, 90(2):190–216, 2003.
- [WEG87] S. Wold, K. Esbensen, and P. Geladi. Proceedings of the multivariate statistical workshop for geologists and geochemists principal component analysis. *Chemometrics and Intelligent Laboratory Systems*, 2(1):37–52, 1987.
- [WHO16] WHO. Malaria fact sheet december 2016. <http://www.who.int/mediacentre/factsheets/fs094/en/>, 2016. [Online; accessed 06-March-2017].

- [WJL03] R. F. Walker, P. T. Jackway, and D. Longstaff. Genetic algorithm optimization of adaptive multi-scale glcm features. *International Journal of Pattern Recognition and Artificial Intelligence*, 17(01):17–39, 2003.
- [WZZO06] J. Wu, P. Zeng, Y. Zhou, and C. Olivier. A novel color image segmentation method and its application to white blood cell image analysis. In *International Conference on Signal Processing*, volume 2, 2006.
- [XP98] C. Xu and J. L. Prince. Generalized gradient vector flow external forces for active contours. *Signal Process.*, vol. 71, pp. 131 - 139, 1998.
- [YAM12] L. Yunda, A. Alarcón, and J. Millán. Automated image analysis method for p-vivax malaria parasite detection in thick film blood images. *Sistemas & Telemática*, 10(20):9–25, 2012.
- [YL04] L. Yu and H. Liu. Efficient feature selection via analysis of relevance and redundancy. *Journal of Machine Learning Research*, 5:1205–1224, December 2004.
- [ZRL77] G. W. Zack, W. E. Rogers, and S. A. Latt. Automatic measurement of sister chromatid exchange frequency. *Journal of Histochemistry & Cytochemistry*, 25(7):741–753, 1977.

Appendix A

Hematopoiesis

The production of all types of blood cells including the formation, development, maturation, and differentiation of blood cells is called hematopoiesis. Its purpose is to ensure the constant daily production of mature cells of the peripheral blood both in healthy condition and in response to particular situations of increased demand, such as in the presence of infection or blood loss. The hematopoiesis is supported by a small number of primitive cells called *Haematopoietic Stem Cells* (HSCs) or *haemocytoblasts*, characterized by the ability of self-renewing, namely the ability to generate cells identical to themselves. At the same time, the HSCs are pluripotent, having the potential to develop into all types of blood cells. Hematopoiesis occurs in bone marrow, where the HSCs are present in the ratio of one stem cell for every 1.000 nonstem cell elements. It is why the cause and effect of haematologic disease are usually rooted in the bone marrow. Usually, only healthy, mature or nearly mature cells are released into the bloodstream, but certain circumstances can induce the bone marrow to release immature and abnormal cells into the circulation. The predominance of immature cells noted in a complete blood count is indicative of infections, inflammations, and other severe illnesses. It is also the reason why it is essential to analyze the whole hematopoietic process, being able to recognize inside the blood smears any cell type at any stage of maturation. The HSCs give rise to mature cells, that enter in the peripheral circulation via the bone marrow sinuses, by firstly differentiating into myeloid (non-lymphoid) and lymphoid precursor committed cells. Myeloid precursor cells develop into monocytes, macrophages, neutrophils, basophils, eosinophils, erythrocytes, megakaryocytes, platelets, and dendritic cells, while the lymphoid precursors develop into lymphocyte T-cells, B-cells, NK-cells. Hematopoiesis can also be subdivided according to the type of cell being formed: granulopoiesis (neutrophils, eosinophils, basophils), monopoiesis (monocytes), lymphopoiesis (lymphocytes), erythropoiesis (erythrocytes) and megakaryocytopoiesis (platelets). Fig. A.1 shows a schema of the hematopoietic process.

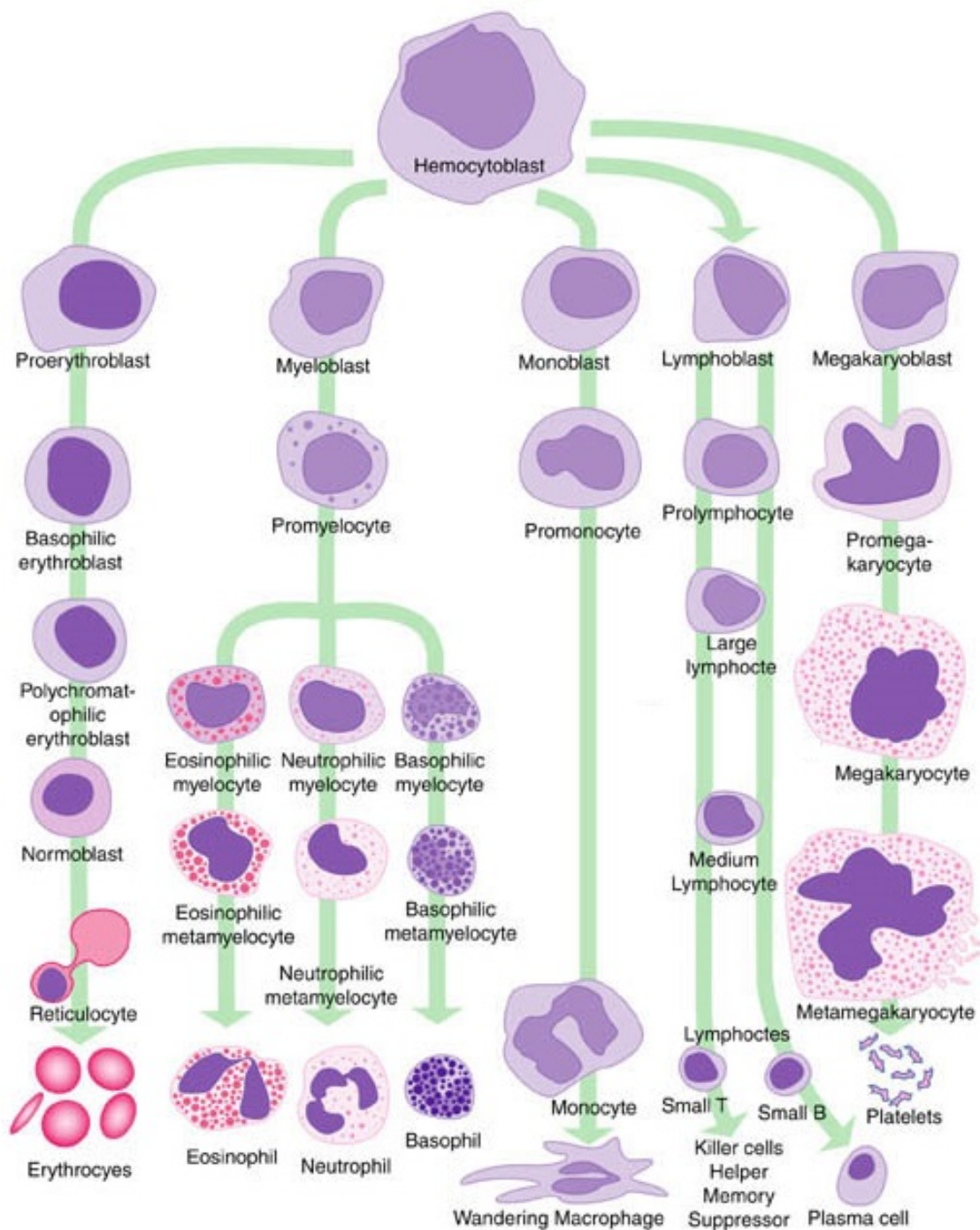


Figure A.1: Hematopoietic process.

A.1 Granulopoiesis

Granulocytes are also called *polymorphonuclear leukocytes* because of their characteristically shaped nuclei and cytoplasmic granules. Granulocytes include neutrophils, eosinophils, and basophils. A granulocyte differentiates into a distinct cell type by a process called granulopoiesis. The stages of maturation for the neutrophilic, eosinophilic and basophilic series is very similar. They start to differentiate at the third stage, so the first two stages are in common. The first five stages of granulopoiesis are illustrated in Fig. A.2.

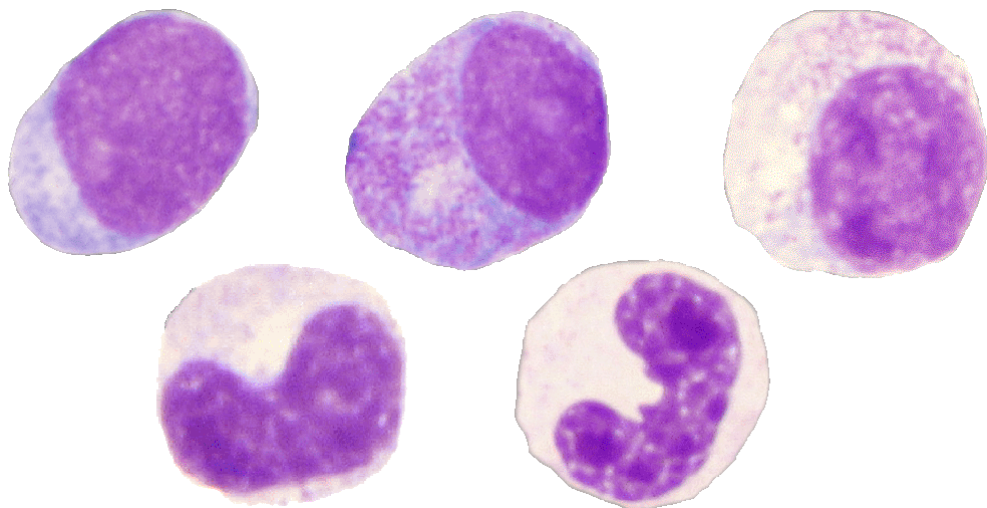


Figure A.2: Granulopoiesis.

At the first stage of maturation the myeloid progenitor, called *myeloblast*, has a size that ranges from 10 to 20 micron. The nucleus is large and centrally round, that could have a round or oval shape, and it has an open, unclumped nuclear chromatin that is of a light red-purple color. The nucleus contains several nucleoli, from two to five, which appear as lightened, refractile round structures, while the cytoplasm is weak and has a moderate blue color and usually without granules. At the second stage the myeloblast transforms in a *promyelocyte* or *progranulocyte*, that has a similar size that ranges from 10 to 22 micron. The nucleus is oval, round, or eccentric and the nuclear chromatin is more condensed of a light red-purple color. The nucleus contains less prominent nucleoli while the cytoplasm presents azurophilic granules. At this stage, the three series starts to differentiate, even if they preserve a similar appearance. Thus the promyelocyte gives rise to a unique myelocyte that can either be eosinophilic, basophilic, or neutrophilic. The myelocyte then differentiates further into a metamyelocyte and then into a band cell before becoming a mature neutrophil, eosinophil, or basophil. The *myelocytes* are slightly smaller than promyelocytes with a diameter of 10-18 micron. They present an eccentric, round-oval nucleus with a coarse and condensed chromatin and small, non-visible nucle-

oli. Some azurophilic granules persist in the cytoplasm, but secondary or specific granules begin to predominate, in particular, the neutrophilic granules are dusty, subtle, and red-blue, while eosinophilic granules are large red-orange and singular, instead basophil granules are large deep blue-purple. The *metamyelocytes* are slightly smaller than myelocytes with a diameter of 10-15 micron. They have characteristic kidney-shaped nuclei and relatively densely clumped nuclear chromatin with no nucleoli. The cytoplasm range from pale blue to pinkish and becomes filled with predominantly secondary granules, although primary granules persist, and tertiary granules begin to appear. The *band forms* have a size of 9 to 15 micron, with a curved or band-shaped nucleus but non-lobular or unsegmented. The cytoplasm is brown-pink, with many fine specific or secondary granules, that start to predominate. The *segmented forms* have a size similar to the band forms, but they present a segmented nucleus, with two to five nuclear lobes connected by thin threadlike filaments. The cytoplasm is pale lilac with blue shading and many fine secondary dust-like granules. In detail, *neutrophils* or polymorphonuclear neutrophils have a diameter of 12-15 micron filled with pink or purple granules and 2-5 nuclear lobes. The chromatin of the segmented neutrophil is coarsely clumped. The cytoplasm is faint pink, and it is filled with fine pink secondary granules. They are involved in the defense against infections. Neutrophils are the most abundant white blood cells in humans and account for approximately 70% of all white blood cells. The presence of abnormally low number of neutrophils is described as neutropenia. Also, the number of lobes and the extent of granulation are diagnostic. Neutrophils with more than 5 lobes are called hypersegmented neutrophils. Neutrophils with more intensely stained (large dark blue) and more granules are described as toxic granulated neutrophils. Vacuoles appear as holes in the cytoplasm and are frequently found in association with toxic granulation. *Eosinophils* instead have a diameter of 10-15 micron and they are easily recognized in stained smears because of their cytoplasm is filled with large, red-orange granules and a bi-lobed nucleus. They are generally low in number (1-3%). The presence of abnormally high number of eosinophils is described as eosinophilia. Also *basophils* have a diameter of 10-15 micron and a coarse, clumped bi-lobed nucleus and the presence of many large, specific secondary purple-black granules in the cytoplasm. Basophils are the least often seen type of WBC (1%). Increased basophils number is called basophilia.

Because white blood cells have such a short time span in the peripheral circulation, alterations either in quantity or in the quality of a particular white blood cell can be quite dramatic. As white blood cells increase, the peripheral smear usually shows an increased number of segmented neutrophils or the presence of younger cells. In either of these cases, toxic changes, such as toxic granulation, toxic vacuolization, the presence of Dohle bodies or Auer Bodies, Pelger-Huet and Hypersegmentation may be observed. These toxic changes are illustrated in Fig. A.3.

Toxic granulation is excessive in amount and intensity, with more prominent granules in segmented neutrophils and bands. Normal granulation in the segmented neutrophils has a dust-like appearance, with the red and blue granules being chal-

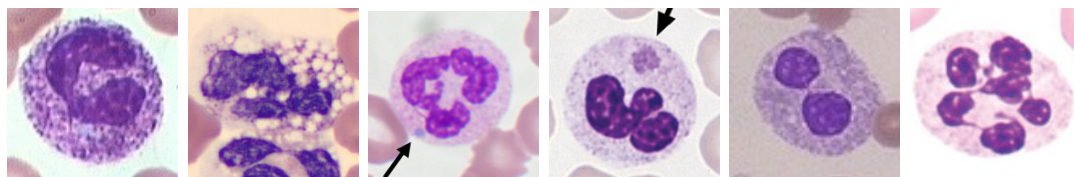


Figure A.3: Granulocyte toxic changes.

lenging to observe, while, with toxic granulation, these granules are more frequent and have much more vivid blue-black coloration. Clusters of toxic granules usually appear in neutrophils. Sometimes the granulation is so dense as to resemble basophilic granules. Toxic granulation can be observed during acute bacterial infections. *Toxic vacuolization* occurs in the segmented neutrophil with the appearance of small or large vacuoles in the cytoplasm. *Dohle bodies* are light blue cytoplasmic inclusions that range from 1 to 5 micron in size, are located in the peripheral cytoplasm of neutrophils and appear as a rod-shaped, pale bluish grey structure. They are nuclear remnants that are often seen in association with toxic granules and vacuoles. Dohle bodies may be present in sepsis or severe inflammatory responses. *Auer Bodies* are clumps of azurophilic granular material that form elongated needles seen in the cytoplasm of leukemic blasts. They are unique, pink or red rod-shaped inclusions that are seen in very immature granulocytes in patients with acute non-lymphocytic leukemia. *Pelger-Huet* is an anomaly characterized by impaired nuclear segmentation of mature granulocytes. The nucleus is often in the shape of a peanut or dumbbell or may consist of two lobes connected with a filament. *Hypersegmentation* is defined as a segmented neutrophilic nucleus having more than five lobes, since normal segmented neutrophils have between three and five lobes in the nucleus.

A.2 Monopoiesis

The cell precursors called monoblasts produce monocytes. Monocytes differentiate and mature from monoblasts into promonocytes and then to matured monocytes. The stages of monopoiesis are illustrated in Fig. A.4.

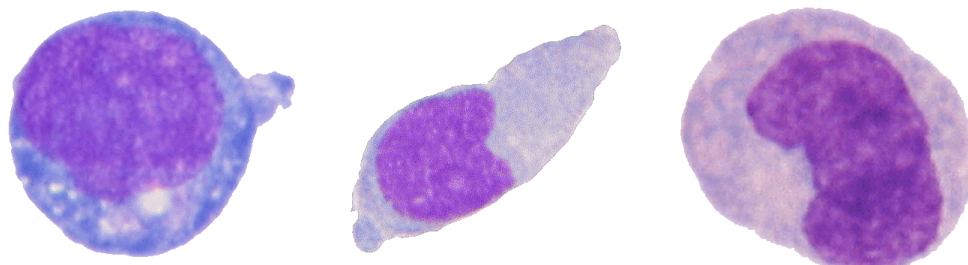


Figure A.4: Monopoiesis.

Monoblast is very similar to myeloblast, with a size of about 12-20 micron. The cytoplasm is agranular and the nucleus is large, round to oval and has fine nuclear chromatin. The main difference with myeloblast is that nucleoli (one or two) are more prominent in monoblasts. *Promonocyte* has an average diameter of 14-18 micron. It has a large, convoluted nucleus, a coarse chromatin structure and one or two nucleoli. The cytoplasm is grey-blue and may contain a few fine azurophilic granules. *Monocytes* are the largest of the white blood cells with a size of 12-20 micron. The cytoplasm is grey-blue, it may have numerous vacuoles and fine azurophilic granules. Monocytes have abundant cytoplasm and a large, distinctive, kidney-shaped nucleus. They circulate in the bloodstream for about one to three days, where they move into tissues throughout the body. They constitute between 3-8% of all leukocytes in the blood. In the tissues, monocytes mature into different types of macrophages and help protect tissues from foreign substances. A decreased percentage of monocyte levels is called monocytosis.

A.3 Lymphopoiesis

Outlining the lymphocyte cell population is a complex task and beyond the scope of this thesis. Furthermore, some populations of lymphocytes appear morphologically similar to peripheral smear. For this reason, only a modified subset of sub-population is included. Lymphocytes are produced by the cell precursors called lymphoblast, that gives rise to prolymphocyte that differentiate into large lymphocyte and small lymphocyte. Fig. A.5 shows the lymphocyte precursors.

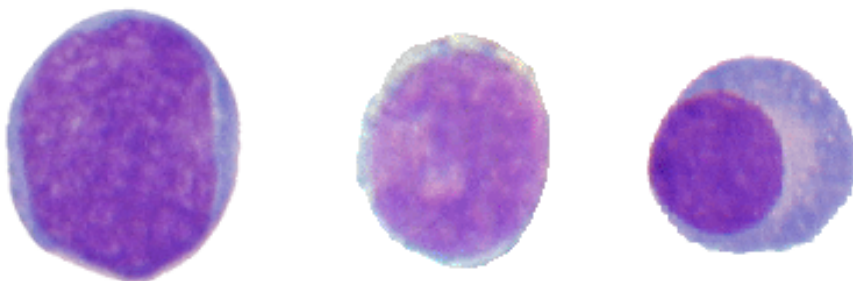


Figure A.5: Lymphopoiesis.

Lymphoblasts have a size of 10-20 micron with a little cytoplasm deep blue staining at the edge. They present one or two nucleoli. *Prolymphocytes* have a size of 9-18 with a grey-blue cytoplasm that is mostly blue at edges. The nucleus is almost round with coarse chromatin and some nucleoli may be present. *Large lymphocytes* have a size of 15 to 18 micron, chromatin more transparent and they present a more significant amount of cytoplasm, lighter in color. *Small lymphocytes* have a size of 7-12 micron. They present an oval eccentric nucleus with coarse, lumpy chromatin

with specific areas of clumping. The cytoplasm is usually just a thin border, with few azurophilic granules. Small lymphocytes consist of T cells and B cells, but it is not possible to distinguish between them in a peripheral blood smear as they appear morphologically similar. Their derivation and function, however, are entirely different. B lymphocytes comprise 10% to 20% of the total lymphocyte population, whereas T lymphocytes comprise 60% to 80%. A third minor population, NK lymphocytes, constitutes less than 10% of the total lymphocyte population. Lymphocytes can also differentiate into dendritic cells, that unlike T-cells, B-cells and NK cells, arise from lymphoid or myeloid lineages. Lymphocytes frequently represent 20 to 40% of circulating white blood cells, and they are the cornerstones of the adaptive immune system. T lymphocytes and B lymphocytes play a role in the maintenance of cell-mediated and antibody-mediated immunity. The increase in the number or proportion of lymphocytes in the blood is termed lymphocytosis, while a decreased number of lymphocytes is termed lymphocytopenia, or lymphopenia.

A.4 Erythropoiesis

Erythropoiesis is the process by which red blood cells (RBCs) or erythrocytes are produced. This process starts with the proliferation and differentiation of HSCs into the red cell precursors. This process is composed of six stages of maturation in the red blood cell series: pronormoblast, basophilic normoblast, polychromatophilic normoblast, orthochromatic normoblast, reticulocyte, and mature erythrocytes. In general, several morphological clues mark the RBC maturation series, the cell size decreases, nuclear chromatin becomes more condensed, the cytoplasm color is altered during hemoglobin production, but the most evident is the vanishing of the nucleus and the decrease in size, as it can be seen in Fig. A.6.

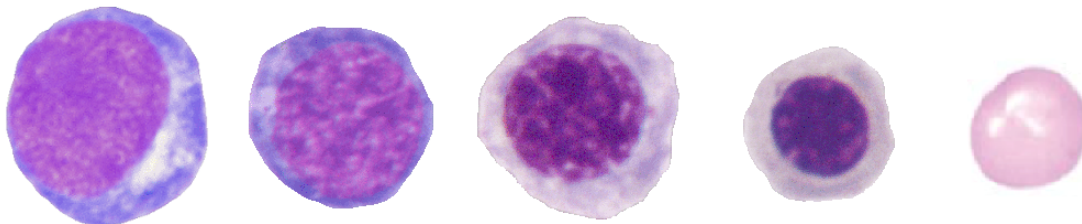


Figure A.6: Erythropoiesis.

The *proerythroblast* or *pronormoblast* is typically 14-20 micron in size. It presents a round centrally located nucleus with coarser chromatin, more reticular, and condensed with a fine texture with deep violet color, nucleoli may be present but are hard to visualize. The cytoplasm presents a dark marine blue color with definitive areas of clearing. The *basophilic normoblast* or *erythroblast* is slightly smaller in size than pronormoblast, typically 12-17 micron of diameter. The nucleus is round with

crystalline chromatin appearance, and it presents closed nucleoli. The cytoplasm becomes more basophilic, a cornflower blue color with indistinct areas of clearing and a grainy and reticular textured chromatin. The *polychromatic* or *intermediate normoblast* has a size of 12-15 micron. The nuclear chromatin is condensed and moderately compacted with no nucleoli. The nucleus becomes smaller with a size of 7-9 micron and the cytoplasm color shift from deep basophilic to grey. The *orthochromic* or *non-nucleated normoblast* has a size of 8-12 micron. The cytoplasm increases with orange-red color tinges with slight blue tone. The nuclear chromatin condenses further, and the nucleus shrinks and tends to become more peripheral and eventually extruded. An orthochromatic normoblast becomes a reticulocyte once the nucleus is extruded. *Reticulocytes* or *polychromatic erythrocyte* are larger about twice than normal mature red cells, with a size of 8 microns, but the most evident difference is the presence of a reticulum in the cytoplasm. The mature cell is released from the bone marrow into peripheral circulation at the reticulocyte stage. Under normal circumstances, reticulocytes constitute about 1% of circulating red blood cells. The reticulocyte count is the most effective measure of erythropoietic activity since it reflects bone marrow healthy or injured. Low reticulocyte counts indicate decreased erythropoietic activity or may occur in ineffective erythropoiesis, a condition in which red blood cell precursors are destroyed before they are delivered to the peripheral circulation, or if the bone marrow is infiltrated with a tumor or abnormal cells. Increased reticulocyte counts indicate increased erythropoietic activity, usually as the bone marrow compensates in response to anemia. The reticulocyte matures after one to two days in circulation into a mature and functional RBC. The mature *erythrocytes* present a significant reduction in the cell size that ranges from 6 to 8 micron and the cytoplasm changes characteristically from blue to salmon pink. Erythrocytes are disk-shaped cells, due to the presence of hemoglobin that is located peripherally, leaving an area of central pallor equal to 1-3 micron, approximately 30-45% of the diameter of the cells.

A.4.1 Erythrocyte Variations

Identifying normal and abnormal erythrocytes is important since automated cell counters have not yet replaced the well-trained eye with respect to the subtleties of red blood cell morphology. Erythrocytes of average size are termed *normocytes*, while erythrocytes larger than average, thus with a diameter greater than 9 microns, are called *macrocytes*, while smaller than average, thus with a diameter less than 6 microns, are called *microcytes*. Erythrocyte color, that in normal conditions is pinkish red with central pallor, is representative of hemoglobin concentration in the cell. Under normal conditions, when the color, central pallor, and hemoglobin are proportional, the erythrocyte is termed *normochromic*. *Hypochromic* cells exhibit an area of central pallor larger than average, thus greater than 50% of the diameter (3 microns), that means a decreased hemoglobin concentration. *Polychromatophilic* cells exhibit a blue-grey cytoplasm, and they are slightly larger than average. Poik-

ilocytosis is a general condition associated with the presence of one or more types of abnormally shaped mature erythrocytes, some of which may indicate the possible presence of a specific disease or disorder. Examples include; spherocytes, elliptocytes, sickle cells, teardrop cells, echinocytes, acanthocytes, keratocytes, bite cells, schistocytes, target cells, stomatocytes, and rouleaux formation. These shape abnormalities are illustrated in Fig. A.7.



Figure A.7: Poikilocytosis.

Spherocytes are compact, round, densely staining red cells that lack central pallor. They are easily recognized among the rest of the red blood cell because they are dense, dark and small. *Ovalocytes* or *elliptocytes* are the most common red cells. They appear rather than the typical biconcave disc-shaped. Erythrocytes with this defect range from slightly oval to elongated cigar-shaped forms and they may appear macrocytic, hypochromic, or normochromic. *Sickle cells* are elongated or shaped like crescents or sickles. The fragile, sickle-shaped cells deliver less oxygen to the body's tissues. They can also get stuck more easily as they try to go through small blood vessels, and break into pieces that interrupt healthy blood flow. Many sickle cells may revert to normal disk shape on oxygenation, but approximately 10% are unable to revert. *Teardrop* are characterized by a smaller size and above all from the appearance that resembles a tear. *Acanthocytes* are characterised by a smaller size and above all from the presence of thorny projections distributed irregularly around the red blood cell, which lacks central pallor. The number of thorn can range from three to nine and must be distinguished from the *echinocytes*, in which the projections are typically evenly spaced on the cell surface and they are more numerous, from 10 to 30. Another difference is that echinocytes have serrated edges over the entire surface and often the membrane is smaller and much more uniform in shape and distribution. *Schistocytes* are fragmented erythrocytes that are irregular in shape and size. They are usually half the size of the normal red blood cells and have a deeper red colour. They can appear as small triangular erythrocytes, helmet cells, and normal-size erythrocytes with 2 to 3 pointed surface projections (*keratocytes*). Round erythrocytes with a single, elliptical or round surface defect are termed *bite cells*. *Stomatocytes* are characterized by a mouth-shaped area of central pallor and

a decrease in the ratio of surface area-to-volume that can be induced either by a reduction in surface area or an increase in red cell volume. Several agents can induce this morphology and often they can also be found on the peripheral smear of healthy subjects, due to drying artifact. It can be distinguished since the percentage of stomatocytes in healthy subjects is usually below 3% of the total red cells. *Target cells* have a centrally located disk of haemoglobin surrounded by an area of pallor with an outer ring of haemoglobin adjacent to the cell membrane giving the cell the appearance of a target. They are seen in the peripheral blood due to the presence of artefacts, because of decreased volume or increased red blood cell surface membrane. *Rouleaux* formation is a phrase denoting an agglomerate of erythrocytes, that create a stack generally in a curving pattern. The flat surface of the RBCs give them a large surface area to make contact and stick to each other forming a rouleaux.

A.4.2 Erythrocyte Inclusions

The cytoplasm of all normal red blood cells is free of debris, granules, or other structures. Inclusions are the result of unique conditions, and their identification can be clinically helpful. Examples of inclusion bodies are howell-jolly bodies, siderotic granules, basophilic stippling, Heinz bodies, malaria, and nucleated red cells. This cell inclusion is illustrated in Fig. A.8.



Figure A.8: Erythrocyte Inclusions.

Howell-jolly bodies represent remnants of the nucleus as it is extruded from the cytoplasm, that appears in the red blood cell as round, deep purple structures of about 1 micron in size. They are eccentrically located in the cytoplasm and seen when erythropoiesis is rushed. *Siderotic granules* or *Pappenheimer bodies* appear as small, dark blue or purple dots, located along the periphery of the red blood cells. *Basophilic stippling* refers to numerous tiny coarse or fine blue granules in the periphery of the cytoplasm. They are difficult to visualize in the peripheral smear without fine focusing, but red blood cell containing basophilic stippling often is polychromatophilic. *Heinz bodies* are defined as large structures approximately 1 to 3 micron in diameter located toward the periphery of the red blood cell membrane. Although they cannot be visualized by standard stain, bite cells in the peripheral smear are evidence that a Heinz body has been formed. *Malaria* is a mosquito-borne infectious disease that results from the multiplication of a parasite within the cytoplasm of the red blood cells. Five species of this parasite can infect and be transmitted by humans, for this reason, the inclusion appearance can be very

different. *Nucleated red blood cells* (NRBCs), that are red cells with a retained nucleus can be observed inside the blood smears. The average size of the NRBC is 7-12 micron in diameter, the cytoplasm is pink, and the nucleus is a homogeneous blue-black mass with no structure. NRBCs detection and quantification is still based on the microscopic analysis of stained blood, since they are often counted as white cells by most hematology analyzers because of the presence of the retained nucleus, and this, in particular in patients with a high nucleated cell count, could lead to misleading results. Sometimes platelets overlying erythrocytes may be mistaken for erythrocyte inclusions.

A.5 Megakaryocytopoiesis

Megakaryocytopoiesis is the process by which platelets or thrombocytes are produced. Platelet development is originated in the bone marrow from the HSC that differentiate into the megakaryocytic precursor, that then develops into the megakaryoblast, that gives rise to the pro-megakaryocyte and then the megakaryocyte before developing into mature platelets. During this period the megakaryocyte nucleus undergoes extensive endomitosis, the cytoplasmic differentiation, the formation of platelet granules, and the fragmentation into mature platelets as it can be seen in Fig. A.9.

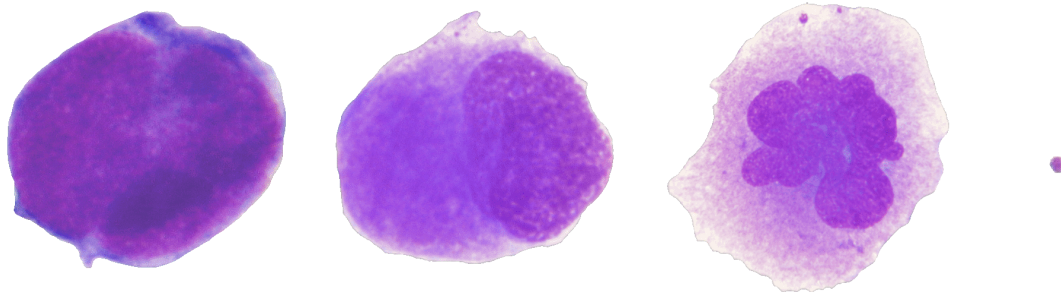


Figure A.9: Megakaryocytopoiesis.

The *megakaryoblast* has a size between 20 to 30 micron. Its nucleus is large, oval or kidney-shaped and contains several nucleoli. It has an insignificant non-granular and slightly basophilic cytoplasm. The *pro-megakaryocyte* is very similar to the megakaryoblast except for the presence of an intensely basophilic cytoplasm that contains fine azurophilic granules. The *megakaryocyte* instead is much bigger than its precursors, having a size around 50-100 micron. It presents a single, indented nucleus and a basophilic (light blue) cytoplasm that contains azurophilic granules. Each megakaryocyte fragments into thousands of platelets. *Platelets* are very small, about 3 microns, the cytoplasm is stained light blue, and it contains purple-reddish granules. Platelets play a crucial role in hemostasis, and they are involved in the formation of blood clot. A low number of platelets is called thrombocytopenia,

while a decrease in function of platelets is called thrombasthenia. In some people, too many platelets may be produced, which may result in interferences with the flow of blood. An increase in the number of platelets is called thrombocytosis. Sometimes this problem could cause bleeding, because many of the extra platelets may be dysfunctional even though they appear healthy. A platelet count is usually evaluated by preparing a blood smear to visualize any anomalies in shape or size directly. Blood smear could present platelets greater than 3 microns in diameter, that is called macrocytic platelets or megathrombocytes. The modern hematology analyzers disregard this kind of platelets since they count the platelets based on their sizing. Also, the count is falsely low when there are platelets clumps. In such instances, the instrument does not count these clumps of platelets and gives the platelet count as falsely low. Usually, in a healthy person, less than 5% of the platelets appear large. Platelet size is of diagnostic significance, particularly if considered in relation to the platelet count. Small or normal-sized platelets in association with thrombocytopenia are suggestive of a failure of bone marrow production, while thrombocytopenia with large platelets is more likely to be caused by peripheral destruction or consumption of platelets with the bone marrow responding by increasing platelet production. Platelet size is also useful in assessing the likely cause of thrombocytosis.

A.5.1 Malaria parasites

Human malaria infection is not strongly related to cell count, but it needs different tests to be identified. It can only be caused by parasitic protozoans belonging to the *Plasmodium* type. The parasites are spread to people through the bites of infected female Anopheles mosquitoes, called “malaria vectors”. There are five parasite species that cause malaria in humans and two of these species, *Plasmodium falciparum* and *Plasmodium vivax*, constitute the greatest threat. *Plasmodium ovale*, *Plasmodium malariae* and *Plasmodium knowlesi* are the three remaining species that are less dangerous in humans [WHO16], as shown in Figure A.10. All five species may appear in four different life-cycle stages during the infection phase in peripheral blood: ring, trophozoite, schizont, and gametocyte. Some examples are shown in Figure A.10. The life-cycle-stage of the parasite is defined by its morphology, size and the presence or absence of malarial pigment. The species differ in the changes of infected cell’s shape, the presence of some peculiar dots and the morphology of the parasite in some of the life-cycle-stages [Som11].

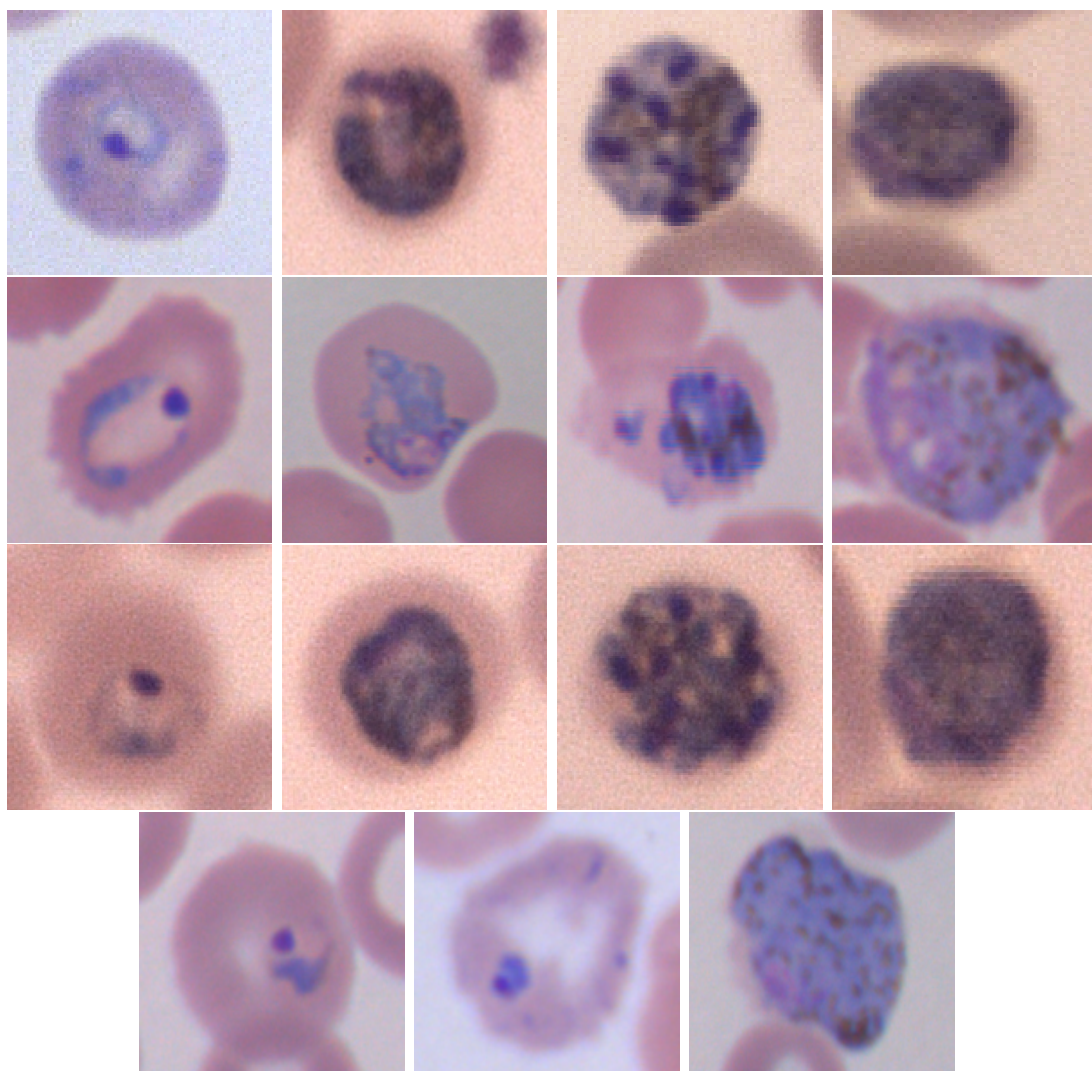


Figure A.10: Examples of malaria parasite stages. First row, from left to right: *P. falciparum* ring, trophozoite, schizont, gametocyte; second row, from left to right: *P. ovale* ring, trophozoite, schizont, gametocyte; third row, from left to right: *P. malariae* ring, trophozoite, schizont, gametocyte; last row, from left to right: *P. vivax* ring, developed trophozoite, gametocyte. Courtesy of CHUV, Lausanne.

Malarial parasite trophozoites are generally ring-shaped, 1-2 microns in size, although other forms (ameboid and band) may also exist. The sexual forms of the parasite (gametocytes) are much larger and 7-14 microns in size. *P. falciparum* is the largest and is banana shaped while others are smaller and round. *P. vivax* causes stippling of infected red cells.

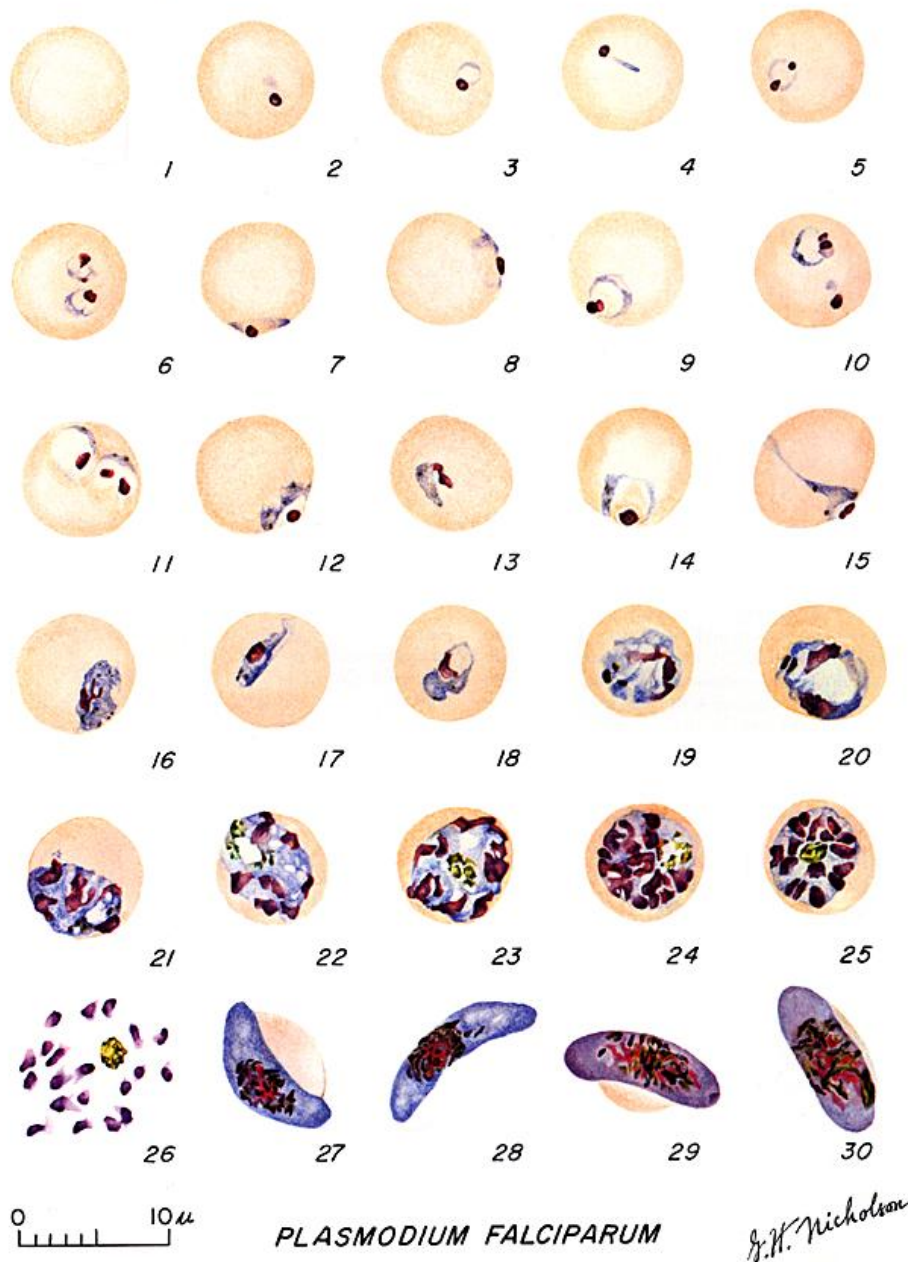


Figure A.11: *Plasmodium falciparum* schematic stages of life. Courtesy of [CDC18]. Fig. 1: Normal red cell; Figs. 2-18: Trophozoites (among these, Figs. 2-10 correspond to ring-stage trophozoites); Figs. 19-26: Schizonts (Fig. 26 is a ruptured schizont); Figs. 27, 28: Mature macrogametocytes (female); Figs. 29, 30: Mature microgametocytes (male).

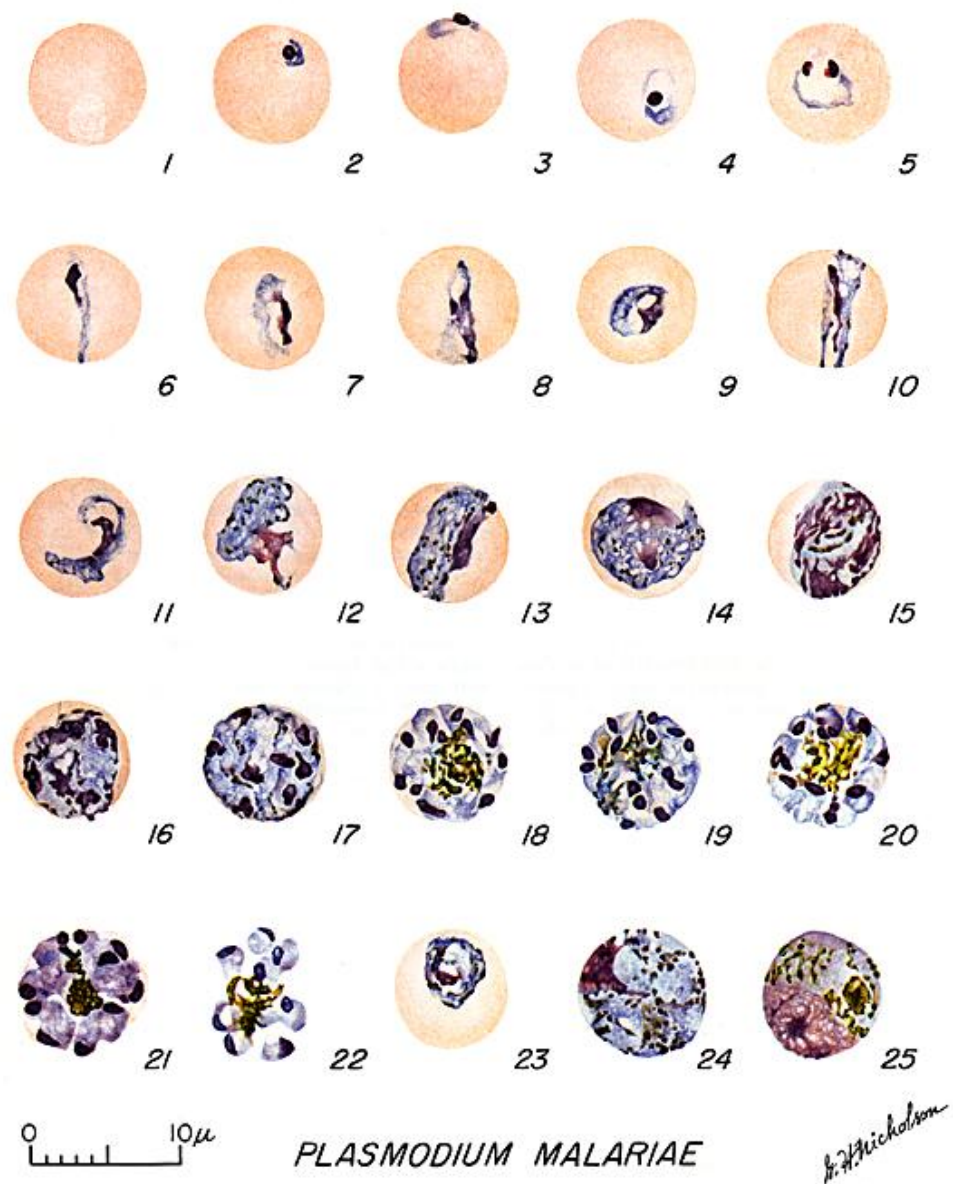


Figure A.12: *Plasmodium Malariae* schematic stages of life. Courtesy of [CDC18]. Fig. 1: Normal red cell; Figs. 2-5: Young trophozoites (rings); Figs. 6-13: Trophozoites; Figs. 14-22: Schizonts; Fig. 23: Developing gametocyte; Fig. 24: Macrogametocyte (female); Fig. 25: Microgametocyte (male).

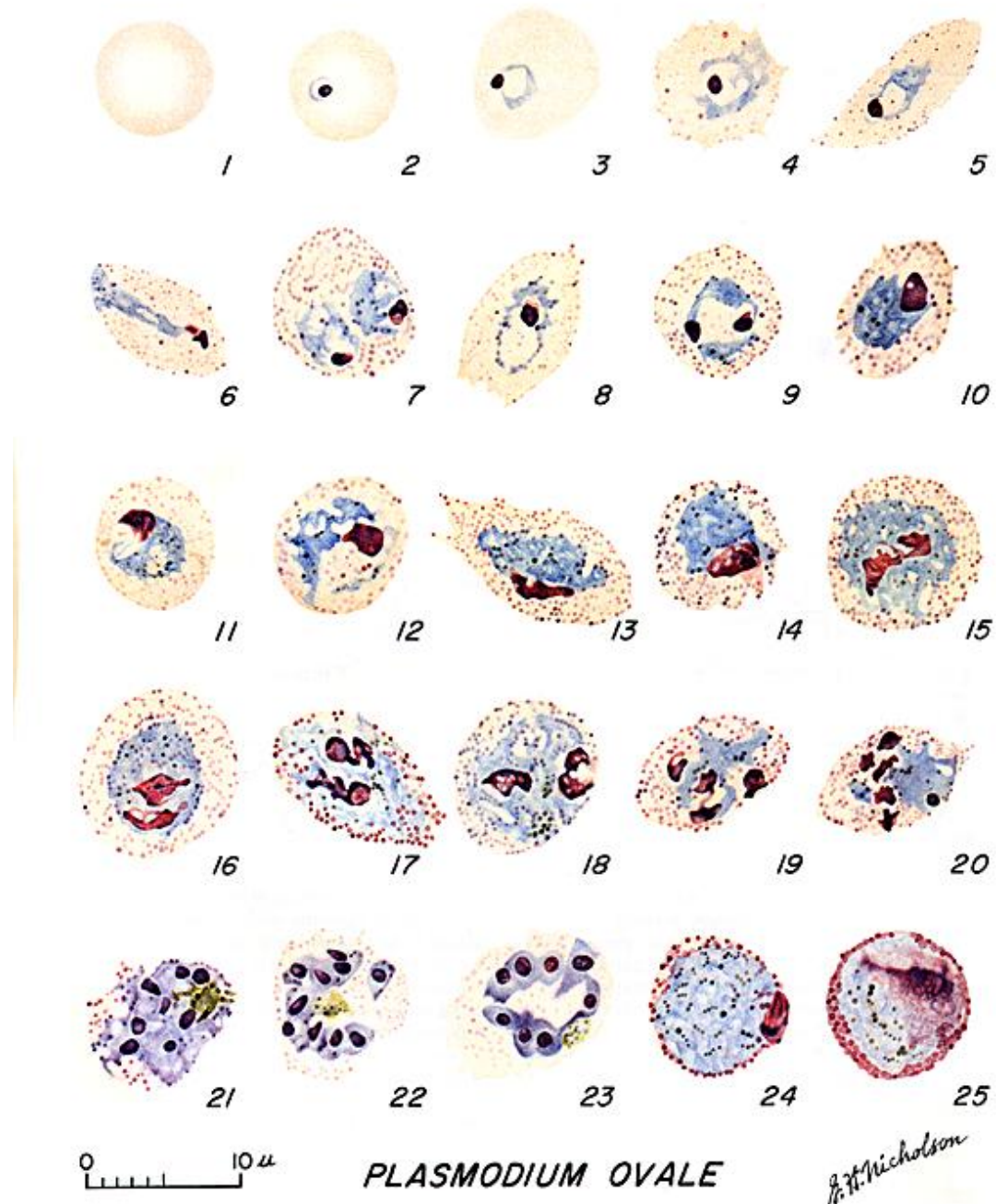


Figure A.13: Plasmodium Falciparum schematic stages of life. Courtesy of [CDC18]. Fig. 1: Normal red cell; Figs. 2-5: Young trophozoites (Rings); Figs. 6-15: Trophozoites; Figs. 16-23: Schizonts; Fig. 24: Macrogametocytes (female); Fig. 25: Microgametocyte (male).

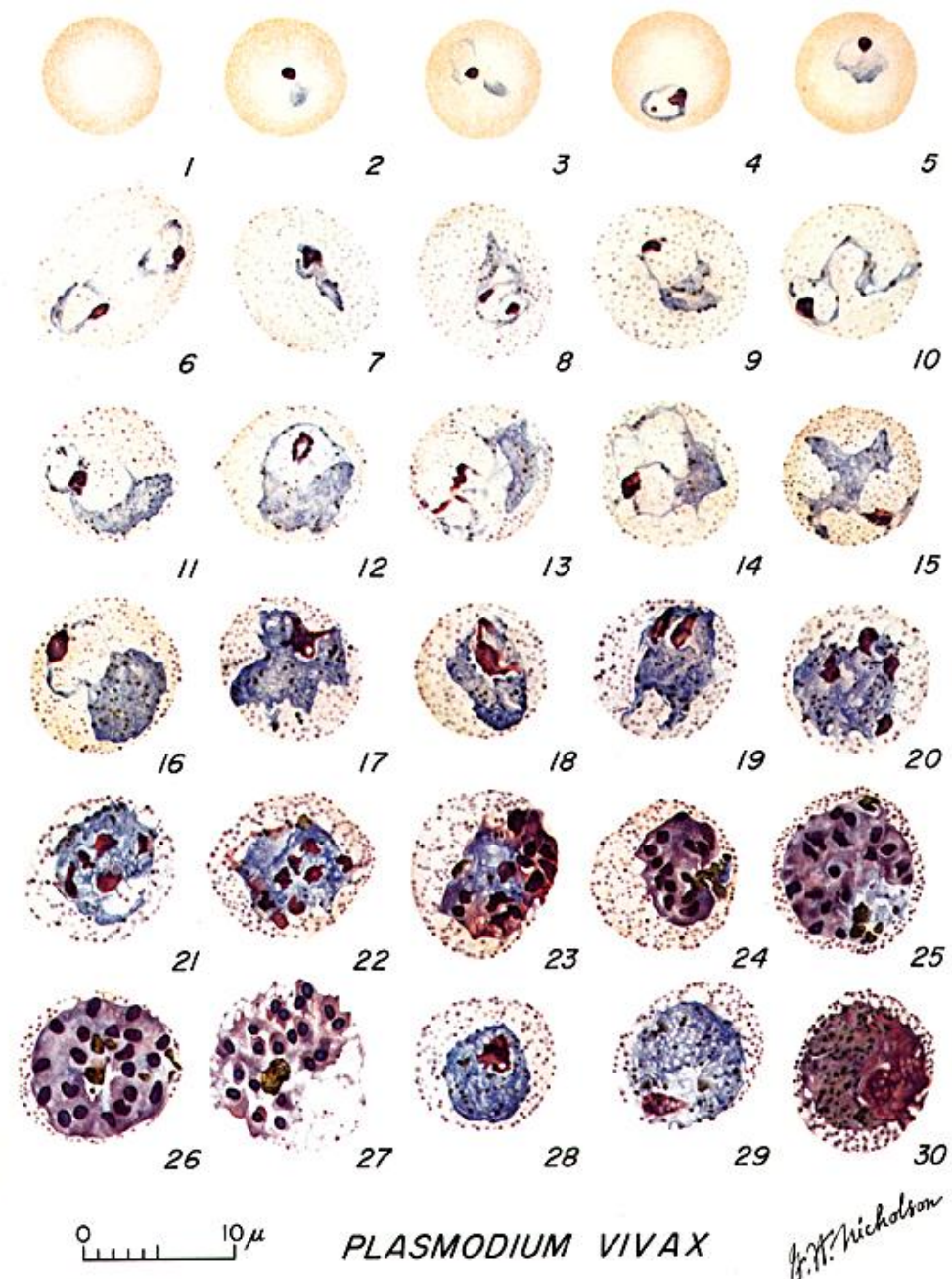


Figure A.14: *Plasmodium Vivax* schematic stages of life. Courtesy of [CDC18]. Fig. 1: Normal red cell; Figs. 2-6: Young trophozoites (ring stage parasites); Figs. 7-18: Trophozoites; Figs. 19-27: Schizonts; Figs. 28 and 29: Macrogametocytes (female); Fig. 30: Microgametocyte (male).